UNIVERSITY OF OKLAHOMA

GRADUATE COLLEGE

IN-SITU MEASUREMENTS AND REMOTELY SENSED ESTIMATIONS OF SURFACE FLUXES OVER THE SOUTHERN GREAT PLAINS OF THE UNITED STATES

A THESIS

SUBMITTED TO THE GRADUATE FACULTY

in partial fulfillment of the requirements for the

Degree of

MASTER OF SCIENCE IN METEOROLOGY

By

HAYDEN MAHAN
Norman, Oklahoma
2016

IN-SITU MEASUREMENTS AND REMOTELY SENSED ESTIMATIONS OF SURFACE FLUXES OVER THE SOUTHERN GREAT PLAINS OF THE UNITED STATES

A THESIS APPROVED FOR THE
SCHOOL OF METEOROLOGY

BY

_____
Dr. Jeffrey Basara, Chair

_____
Dr. Xiangming Xiao

_____
Dr. Petra Klein

© Copyright by HAYDEN MAHAN 2016
All Rights Reserved.

Acknowledgements

These past few years I have grown and excelled as a scientist and person thanks to the help of many advisors, colleagues, friends, and family members. This thesis was supported, in part, by the Agriculture and Food Research Initiative Competitive Grant (2012-02355) from the USDA National Institute of Food and Agriculture. First, I owe much gratitude to my advisor, Dr. Jeffrey Basara. He taught me most of what I know today about fieldwork, research ethic, and interacting with fellow scientists. Had it not been for him I would not have had the once-in-a-lifetime opportunity to conduct research at Seoul National University for a summer. I appreciated the time he spent mentoring me and overseeing my studies. This thesis was a success thanks to his recommendations and many hours of edits. I also would like to thank my advisors Dr. Xiangming Xiao and Dr. Petra Klein. I have worked closely with Dr. Xiao and his lab members. He bridges the gap between the colleagues that I have worked beside in the field and me. Dr. Klein has supported me since my undergraduate. There was one specific instance during my time in her class as an undergraduate that she expressed how impressed she was with my studies. That moment help embolden me to pursue this degree. I thank both Dr. Xiao and Dr. Klein for their edits, recommendations, and time that they have devoted to me during this process.

I could not have collected all of the data I did had it not been for my colleagues Yuting Zhou, Rajen Bajgain, and Pradeep Wagle. Their teamwork and assistance in the field, in data processing, and motivation helped solidify this work. There were many times I would not know how to tackle a problem, but the three of them were more than

willing to put aside their own work to help assist me in mine. Not only are they long lasting colleagues of mine now, but they are now some of my closest friends.

I am also grateful to have gotten the opportunity to conduct research at Seoul National University thanks the National Science Foundation East Asian Pacific Summer Institute. While there I had the privilege to work alongside Dr. Youngryel Ryu, Dr. Chongya Jiang, and the rest of his lab members. Had it not been for Dr. Ryu's willingness to mentor me for a summer my thesis would not carry as much weight as it does now. Dr. Jiang was a key component to the success of my modeling work as he was able to provide me with the resources I needed to complete my work. I look forward to continuing a lasting relationship with my Korean counterparts. Thank you, and as they say in Korean, gamsamnida.

Lastly, I would like to thank my friends and family. They were a nice escape from the academic world. To be able to hear their encouraging words and high praise for my accomplishments helped continue to push me when things seemed out of my control. My parents, John and Rhonda Coontz, have been my biggest supporters during this journey. If it were not for them I would never have been able to reach these goals. I appreciate all of the support, both financially and emotionally, that they have given me.

Table of Contents

List of Tables

List of Figures

Abstract

Evapotranspiration (ET) is an important variable in the hydrologic cycle. As such, improved understanding of the spatial and temporal variability of ET is critical to weather and climate analysis and prediction, water management resources, agriculture, land-use and land-change projects, and ecological research. Eddy covariance flux towers were deployed over grasslands and winter wheat at the United States Department of Agriculture site near El Reno, Oklahoma and at the Marena Oklahoma In-Situ Sensor Testbed (MOISST). Ten total years of surface energy, water, and carbon fluxes were paired with fifty total years of data from twelve additional flux towers across the Southern Great Plains (SGP) for a regional land-surface analysis using the Breathing Earth System Simulator (BESS). BESS is a land-surface model that couples land-atmosphere processes to estimate ET and gross primary production (GPP). The study results show that BESS and the observations yield good agreement with R^2 values of 0.74. Further, BESS outperformed other ET estimates including a two-source surface energy balance model (Gowda et al. 2013), an empirical model (Wagle et al. 2016), and the MODIS ET product. ET decreases from southeast to northwest across the SGP, ranging from 300-1000 mm/year. ET varies more in the southwest portion of the SGP (50-100 mm/year) and less in the northeast (10-40 mm/year). Using BESS to analyze long-term ET, it was determined that, on average, 74% of the precipitation received in the SGP is re-distributed by ET. However, the results also noted that BESS lacks the ability to accurately depict ET patterns during flash drought conditions, as seen during 2012, but can depict drought and pluvial conditions when soil moisture and near-surface atmospheric conditions are in equilibrium.

Chapter 1 : Introduction

1.1 Motivation

Ecosystems influence weather and climate processes on a wide range of temporal scales via fluxes of moisture, energy, and momentum between the land surface and the atmosphere (Pielke et al. 1998). Short-term interactions include the evolution of the atmospheric boundary layer (ABL) throughout the day (McPherson and Stensrud 2004) whereby the boundary layer will grow, in part, based on how available energy is partitioned. If more energy is realized as sensible heat flux then buoyancy creates turbulent entrainment in the ABL allowing for growth in height. Long-term interactions can create moisture feedback loops between the atmosphere and land surface that influence drought and pluvial conditions (Pielke et al. 1998; McPherson and Stensrud 2004).

Evapotranspiration (ET) is latent heat flux expressed in terms of mm/day rather than W/m^2. ET influences global climate change, water balance, carbon exchange, agriculture, drought, flooding, and surface-based weather processes (Fisher et al. 2008). Due to a lack of a long-term ET datasets it is unclear how ET will be impacted by a changing climate (Ryu et al. 2008). One of the most widely used methods of measuring ET is with eddy covariance flux towers that have a spatial scale of 100s of meters (Baldocchi 2013). These measurements at various sites are important because gaps remain in the understanding how ET across different ecosystems varies and how ET responds to climate variables at different timescales (Wagle et al. 2016).

Approximately 20% of the global land cover consists of grasslands (Ryu et al. 2008) and it is unknown how land-use and land-cover change will influence water yield

in these regions (Marc and Robinson, 2007). Water vapor and carbon exchange in grasslands are anticipated to be more sensitive to climate perturbations (Knapp et al. 2002). Thus, understanding how ET varies across grassland regions is important in determining how climate factors spanning different time and spatial scales will affect ecosystems in the current and future climate (Wagle et al. 2016).

Because observations of ET require expensive instrumentation and extensive maintenance it is not practical to deploy in-situ measurements at high density on large spatial scales. As such, remote sensing has been proposed as the most efficient tool to collect ET data across the globe (Gowda et al. 2008). These observations can be used to model ET processes through surface energy budget models as well as empirical/statistical models.

1.2 Study Period and Domain

The SGP is defined by Christian et al. (2015) as Kansas, Oklahoma, and climate divisions 1-4 that comprise Northern Texas (Fig. 1.1). This is a region that experiences dramatic interannual variability of precipitation that can lead to drought and flooding (Christian et al. 2015). Approximately 70% of land use in the SGP is designated for agricultural and livestock purposes and the vast majority of Kansas consists of agricultural vegetation and shrubland/grassland (Fig. 1.2). Western Oklahoma and the Texas Panhandle are similar to Kansas with agricultural vegetation and shrubland/grassland distributed throughout the region. The southeastern portions of Oklahoma and Texas are comprised of forests, crops/introduced vegetation, and wetlands. For this project, the study period for the in-situ based analysis spanned from 2012-2015 while the study period focused on remote sensing spanned from 2000-2015.

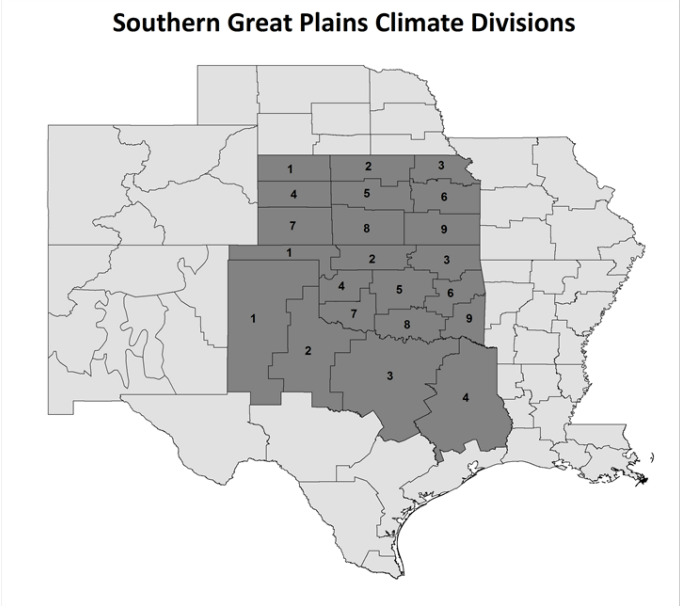

Figure 1.1.1: The Southern Great Plains of the United States region as defined by Christian et al. (2015).

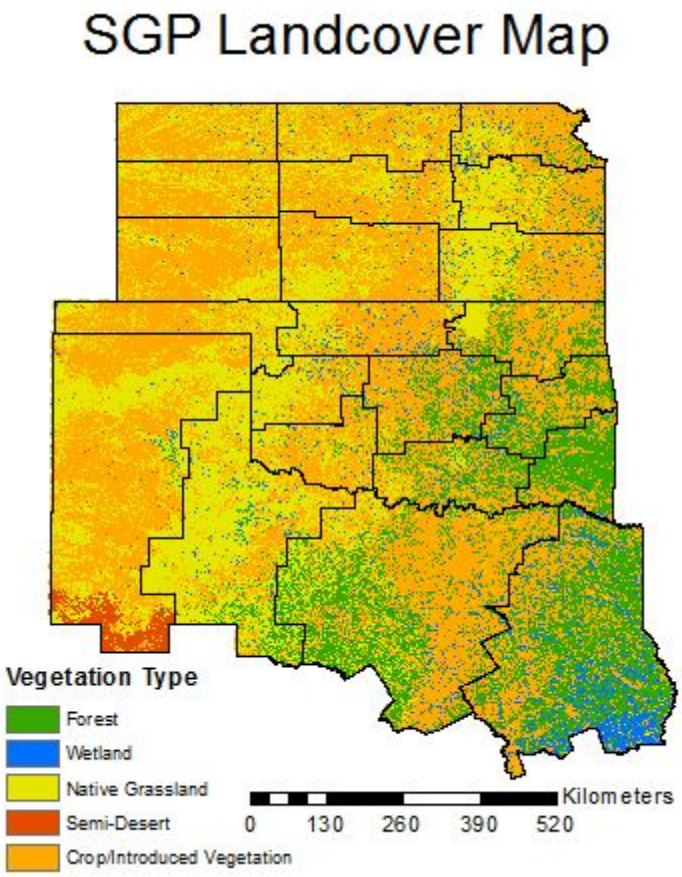

Figure 1.1.2: Landcover map of the SGP (USGS 2016)

1.3 Thesis Objectives

The overarching goal of this study was to investigate surface fluxes across the SGP. A quality-controlled dataset was created from four in-situ measurement sites across central Oklahoma from 2012-2015 augmented with data from an additional 12 flux towers across the SGP. The in-situ data collected across the SGP was compared with satellite-derived ET and a case study was conducted to determine the applicability of remotely sensed ET. Thus, the objectives include:

(1) developing a quality-controlled surface energy budget dataset from 16 flux towers across the SGP;

(2) compare these observations with ET estimations from several land-surface models that incorporate remotely sensed data; and

(3) apply the utility of the best model at local scales to determine how observations and estimations compare.

The format of this thesis begins with a literature review that gives background for what ET is, how it is measured, and how these measurements are acquired on a large spatial and temporal scale. Next, a data and methodology chapter explains how this data was collected across the domain and how that data was used to complete the objectives stated prior. Then, an analysis of the in-situ flux measurements collected in Oklahoma demonstrates how energy is distributed in these regions, confirms the quality of the data used, and quantifies the ET and carbon exchange at the sites. After, an evaluation of three methods to estimate ET using satellite data was explored with an assessment of the best model to follow. Finally, a site-specific case study was conducted to examine how well the Breathing Earth System Simulator (BESS) captures rapidly changing surface ET fluxes.

Chapter 2 : Literature Review

2.1 Evapotranspiration

ET is a two-component quantity (evaporation and transpiration) measured as a single variable. Evapotranspiration is defined as *"*the *combined processes through which water is transferred to the atmosphere from open water and ice surfaces, bare soil, and vegetation that make up the Earth's surface"* (American Meteorological Society 2012). An accurate representation of the total ET process is important for understanding hydrological, meteorological, ecological, and agronomical processes (Pielke et al. 1998).

The hydrological cycle defines how water in the Earth system is budgeted between evapotranspiration, precipitation, storage, and runoff:

$$\mathbf{P = ET + Q + \Delta S} \tag{2.1}$$

where ΔS is the change in water storage, P is the precipitation, ET is the evapotranspiration, and Q is the runoff of the water through the surface and tributaries. Of the three terms on the right-hand side of equation 2.1, ET has been found to contribute significantly to the partitioning of precipitation, and depending on the region and ecosystem, 50-90% of P is converted to ET (Ford et al. 2007).

The surface energy budget defines how incoming radiation is partitioned. At the surface, the net radiation is partitioned to heat fluxes via the energy budget:

$$\mathbf{R_n = LH + SH + G} \tag{2.2}$$

where R_n is the net radiation, LH is latent heat flux, SH is sensible heat flux, and G is ground heat flux. The partitioning of R_n into LH, SH, and G vary based on the time of year, time of day, ecosystem, temperature, wind speed, and water availability. Latent heat flux is ET expressed in terms of energy (Wm^{-2}) and as such, dividing LE by the latent heat of vaporization ($\lambda_v \sim 2.45$ MJ kg^{-1}) yields ET in mm/day (Gowda et al. 2013).

Studies have shown that land cover type is the largest contributing factor to surface flux variability (Fischer et al. 2007 and Sellers 1965). For example, the net radiation afforded to a dessert region is nearly completely partitioned to sensible heating (Fig. 1; Middle Left) while a wetland spends most of its net radiation to latent heating (Fig. 1; Top Left). For more temperate humid regions, 70-80% of net radiation is afforded to latent heating with sensible heating contributing to approximately 10-15% of the energy budget, and less than 5% going towards ground heating during the growing season (Fig. 1; Bottom Right).

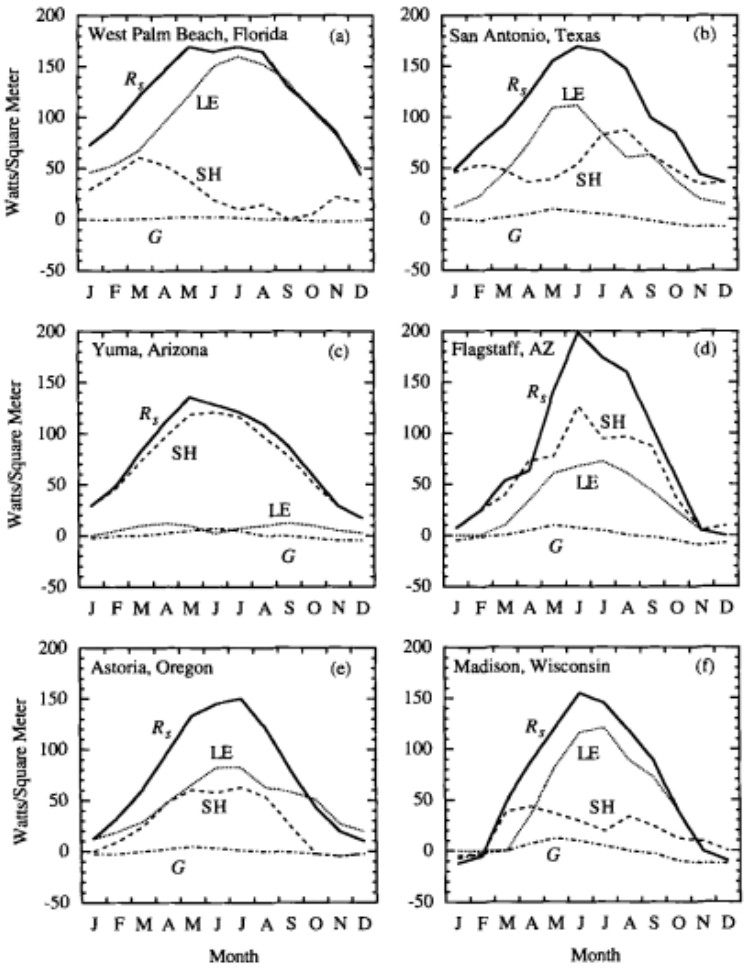

Figure 2.1: Annual cycle for surface energy budget for different ecosystems and latitudes (Sellers, 1965).

Approximately 80% of the Southern Great Plains of the United States (SGP) is grassland and cropland (Fischer et al. 2007). For grassland regions during the growing season 25-50% of energy was partitioned to LH (Wagle and Kakani, 2012).

Further, ET over the SGP has been found to be lowest in grasslands, approximately 15% higher in croplands, and around 30% higher in forested regions (Twine et al. 2004).

2.2 Eddy Covariance Theory

2.2.1 A Brief History of Eddy Covariance Theory

Eddy covariance theory can be dated back to Sir Osborne Reynolds in 1895 when he discovered Reynolds averaging that allowed fluxes to be computed (Reynolds, 1895). However, this theory was ahead of the technology that could measure such fluxes, and the application of the theory could not be immediately applied. Ludwig Prandtl, G.I. Taylor and Bowen (1920's) developed the flux-gradient approach in order to evaluate momentum, water, and heat fluxes (Baldocchi, 2013). One of the first known applications of this approach was completed by F.J. Scrase in 1926 using very primitive instrumentation on small time scales (Scrase, 1930).

It was not until the 1950's that advances in instrumentation paved the way for measurements multiple times per second with the use of hot-wire anemometers and thermometers (Swinbank, 1951). This method was still insufficient in recording large temporal datasets and was accompanied with much uncertainty in data reliability. For the next several decades research focused on designing instrumentation and methods to measure these variables accurately (Baldocchi, 2013). In addition, studies had to rely on ideal conditions to obtain the most reliable data. Several experiments that were conducted relied on flat terrain in sunny and neutral atmospheric conditions (Businger, 1971; Pruitt et al. 1973; Hess et al. 1981; Swinbank and Dyer, 1967; Zilitinkevich and Chalikov, 1968). Even so, these studies parameterized and modeled surface layer turbulence (Foken, 2006).

Modern micrometeorology research of eddy covariance measurements have only been made possible for the past few decades thanks to the development of open and

closed path gas analyzers (Baldocchi, 2013). The first studies using these instruments were on temporal scales of hours due to the need for constant calibration of the instruments and lack of computer data storage (Auble and Meyers, 1992; Hyson and Hicks, 1975; Ohtaki and Matsui, 1982). By the 1990's companies were producing commercial sensors accessible to research scientists. These new sensors, along with advancements in data storage, allowed for data collection to be conducted on scales of days and weeks without the worry of re-calibration (Gash et al. 1989; Sellers and Hall, 1992; Sellers et al. 1995; Sellers et al. 1997; Gash et al. 1997). Since the mid 1990's, a renaissance in eddy covariance measurements research has occurred and scientific publications have grown from less than 100 per year in the mid 90's to near 500 per year in recent years (Baldocchi, 2013). Therefore, this field of science is fairly young with little long-term datasets and many questions remaining unanswered.

2.2.2 Measuring Atmospheric Fluxes

The most commonly used and highly accurate way to measure ET is through in-situ eddy covariance (EC) towers that utilize a sonic anemometer with a water vapor gas analyzer to produce 30-minute flux averages from 10-hz data (Burba 2013; Baldocchi et al. 1998). 30-minute flux averages are calculated because this allows enough time to measure both positive and negative vertical wind components, therefore it can be assumed that the system is in a steady state if the mean vertical wind is zero. These fluxes are calculated by measuring the vertical transportation of a gas (e.g., water vapor) via eddies created by horizontal and vertical turbulence. The flux of any gas is represented as the product of the mixing ratio of the gas (s), air density (ρ), and vertical wind speed (w):

$$\mathbf{F} = \overline{\boldsymbol{\rho} * \boldsymbol{w} * \boldsymbol{s}}$$

(2.1)

where F is the vertical flux of the gas. Reynolds decomposition (Reynolds, 1895) is used to break the terms down into their means and deviations until the equation is simplified down to

$$\mathbf{F} = \overline{\boldsymbol{\rho}} * \overline{\boldsymbol{w}' * \boldsymbol{s}'}$$

(2.2)

that represents the product of the mean air density and covariance of the vertical velocity fluctuation and concentration fluctuation. For latent heat flux, equation 2.2 becomes

$$\mathbf{LE} = \boldsymbol{\lambda} \frac{{}^{\boldsymbol{M_w}}/_{\boldsymbol{M_a}}}{\bar{\boldsymbol{P}}} \overline{\boldsymbol{\rho}} \overline{\boldsymbol{w}' \boldsymbol{e}'}$$

(2.3)

where λ is latent heat of vaporization, M_w is the mass of water vapor, M_a is the mass of air, P is pressure, and e is the water vapor mixing ratio. LE can be converted to ET by dividing by the latent heat of vaporization (ET = LE/λ). These values can then be integrated over an entire day to obtain daily values of ET in mm hr^{-1} or mm day^{-1} (Rebmann et al. 1983). Interdisciplinary fields can benefit from a better measuring protocol for ET, including meteorology, agronomy, ecology, and hydrology (Wan et al. 2015).

2.3 Estimating Evapotranspiration

2.3.1 Remote Sensing Approaches

Remotely sensed ET provides estimates across the globe at various spatial and temporal resolutions. Because it is impossible to have in-situ measurements densely spread across large scales due to the high cost and need for maintenance, satellite measurements can help create estimates of ET across the globe. Several relationships incorporate satellite measurements to estimate ET: Penman-Monteith equation (Monteith, 1965), Priestley-Taylor method (Fisher et al. 2008), and vegetation index-ET empirical relationships (Tang et al. 2009). The return interval for the LandSat and Moderate Resolution Imaging Spectrometer (MODIS) satellites is 16 days and 8 days, respectively. These satellite measurements require clear-sky conditions to accurately measure surface features. As such, this poses a challenge for accurate temporal resolution of ET across the globe, especially in wet climates. The anticipated launch of the Hyperspectral Infrared Imager (HypsIRI) in 2021 with a return interval of 5 days will allow for increased return interval. However, for many scientific applications, this will still be too coarse. As such, methods have been developed to utilize temporal downscaling of satellite measurements to daily time scales to achieve higher temporal resolution. However, these downscaling techniques decrease the accuracy of the ET estimation (Ryu et al. 2012; Allen et al. 2015; Cammalleri et al. 2014).

2.3.2 Surface Energy Balance System

The Two Source Surface Energy Balance System (TSEBS) is a two-source model that calculates the canopy and surface latent heat fluxes. Specifically, surface energy balance models have shown an agreement between 85%-90% over corn and

soybean in Ames, Iowa (Su et al. 2005). Conversely, Timmerman et al. (2011) found that the estimates over tall vegetation were less accurate. Gowda et al. (2013) measured ET using four weighted lysimeters over four irrigated and dry fields of corn, sorghum, cotton, and sunflowers over 16 days from 2006-2009 in Amarillo, TX and found a strong correlation between estimated and observed ET (R^2 = .86). In El Reno, Oklahoma TSEBS forced with Landsat data resulted in R^2 = .79 over the controlled site and R^2 = .77 over the burned site (Fig. 2.2a and 2.2b).

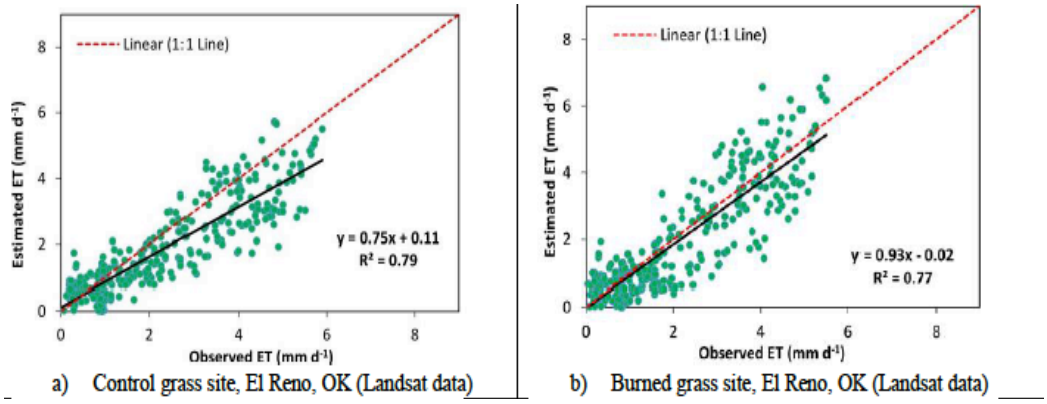

Figure 2.2: TSEBS vs. Observed ET over two grassland sites in El Reno, Oklahoma in 2005 using LANDSAT data. (a) Control grassland site, (b) burned grassland site (Gowda et al. 2016).

2.3.3 An Empirical Model from Wagle et al. 2016

A simple empirical model was developed by Wagle et al. (2016) to estimate ET over grassland regions of the United States Great Plains. The model only requires enhanced vegetation index (EVI) and photosynthetically active radiation (PAR) data as inputs. Recently, ET values were evaluated over three tallgrass prairie sites in the central United States (Wagle et al. 2016) with observed ET yielding R^2 values of 0.87-0.96 (Fig. 2.3). However, Wagle et al. (2016) was only evaluated using MODIS EVI and in-situ PAR. There is motivation to see how the results vary when using both MODIS EVI and MODIS PAR over a larger number of grassland sites.

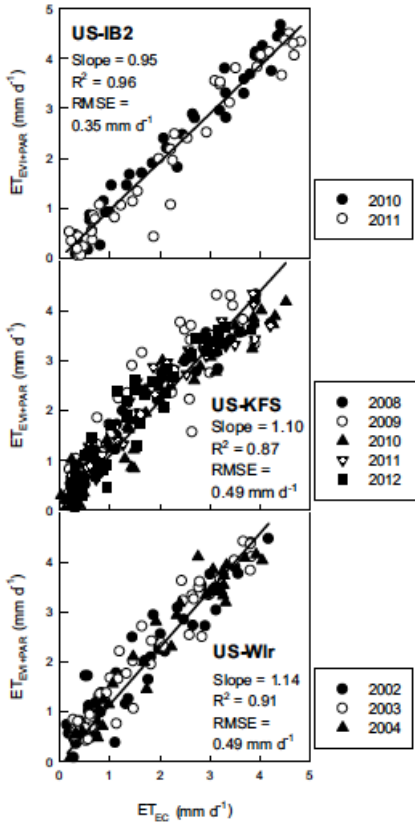

Figure 2.3: Comparison of estimated ET with observed ET from three eddy covariance towers (Wagle et al. 2016).

2.3.4 Breathing Earth System Simulator

BESS is a global model that estimates ET and gross primary production (GPP) on 1 km spatial scales and 8-day temporal scales that can be downscaled to 1-day or integrated to monthly and annual means (Fig. 2.4). BESS utilizes MODIS radiation data and meteorological reanalysis data to estimate ET and GPP. Unlike most land surface models, BESS does not utilize precipitation as a forcing term because global precipitation data can tend to be highly erroneous (Ryu et al. 2011). In a recent evaluation, BESS performed better than MODIS ET and GPP products over 33 eddy covariance towers across the globe (Ryu et al. 2011). For grasslands a correlation between 0.8-0.9 over three sites (Fig. 2.5) was observed for locations in Tibet, Canada,

and Denmark. Over croplands BESS yielded slightly lower correlations with values between 0.8-0.85 for three sites (Fig. 2.5) in Nebraska, Illinois, and Denmark, all of which are outside of the SGP.

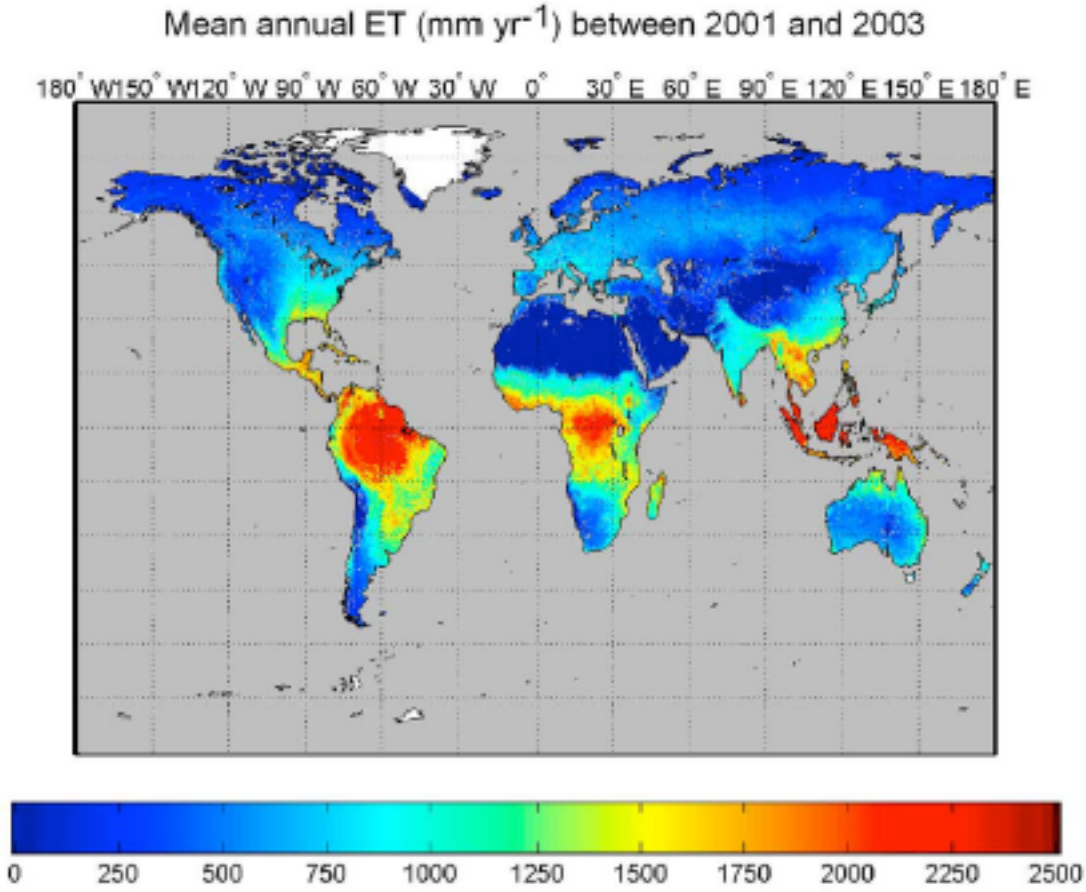

Figure 2.4: Global map of evapotranspiration (Ryu et al. 2011).

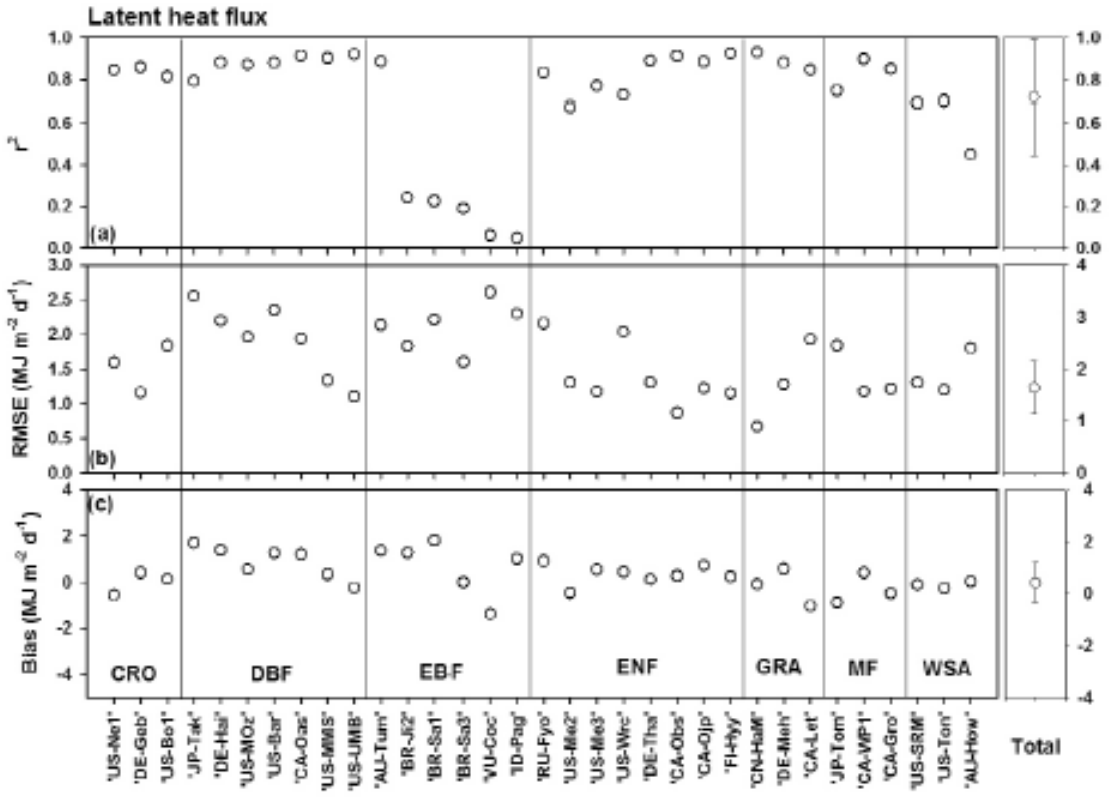

Figure 2.5: 8-day mean daily sum of latent heat flux between 33 eddy covariance flux towers and BESS. Where CRO is crop, DBF is deciduous broadleaf forest, EBF is evergreen broadleaf forest, ENF is evergreen needle forest, GRA is grassland, MF is mixed forest, and WSA is woody savanna (Ryu et al. 2011).

Chapter 3 : Data and Methodology

3.1 Installation of an Eddy Covariance Network

During the Spring of 2014, a network of eddy covariance towers were installed near El Reno, Oklahoma at the United States Department of Agriculture (USDA) Grazinglands Research Laboratory (GRL). Two towers were deployed over grassland surface conditions (Integrated Grassland Observing Systems; IGOS) and one tower was deployed within a winter wheat field (Integrated Cropland Observing Systems; ICOS). Grassland site 1 (IGOSE) was installed over native vegetation that was grazed by cattle while Grassland site 2 (IGOSW) was installed over improved vegetation that had been burned and fertilized. These towers were maintained and collected data during the growing seasons of 2014 and 2015. Another tower site (Marena) used in this research was co-located with the Marena In Situ Soil Moisture Testbed (MOISST; Cosh et al. 2016) near Marena, Oklahoma over native vegetation. This site was installed in November 2011 and has collected data throughout the study period.

3.1.1 Weather Conditions for El Reno, Oklahoma 2014-2015

During an abnormally dry winter in 2014 limited precipitation fell over El Reno, Oklahoma created very dry soil conditions that was not conducive for winter wheat growth (Fig. 3.1). As a result, the winter wheat crop was very poor and could not be harvested. This led to a data gap in ICOS for the 2014 growing season. Thus, there is only data for 2015 over ICOS. The entire 2014 growing season had below average precipitation. However, a wet June supported an active growing season. 2015 was one of the wettest years ever in Oklahoma. As such, this research is beneficial because it allows insight into how vegetation in Oklahoma responded to one of the wettest periods

in history.

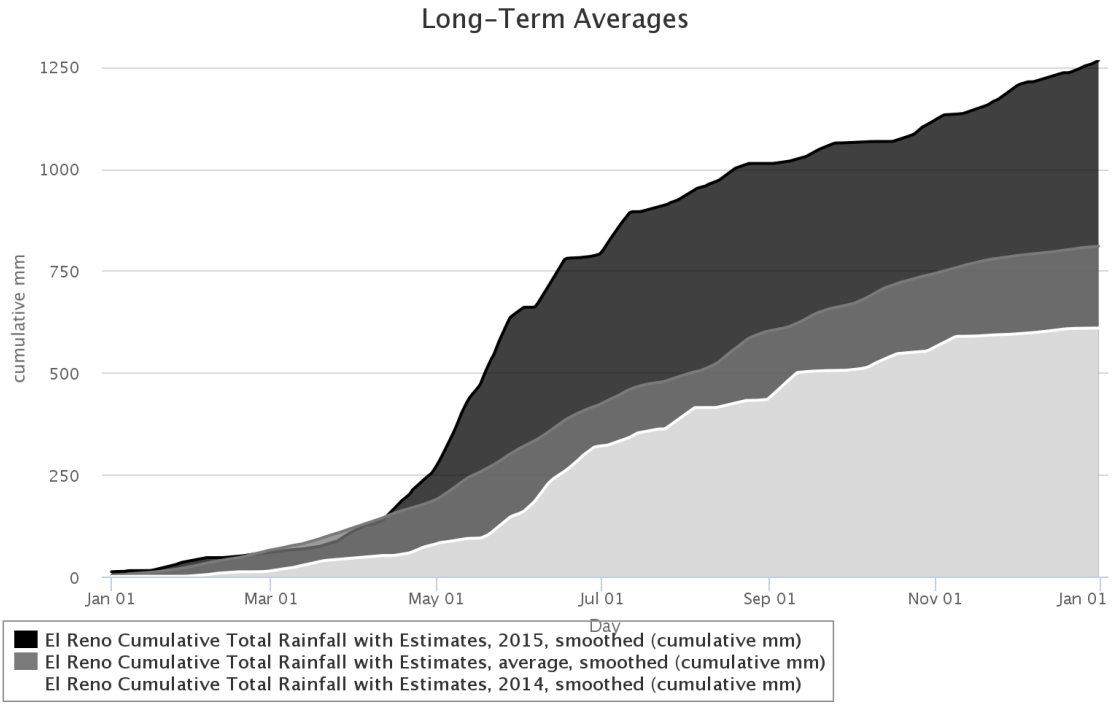

Figure 3.1: Cumulative rainfall distributions over El Reno, Oklahoma for 2014 and 2015 compared to the average 2001-2015 rainfall distribution (source: mesonet.org).

Drought conditions over El Reno increased during the wintertime. According to the United States Drought Monitor (Svoboda et al. 2002) there was no drought in the beginning of 2014, however drought developed quickly. On a scale of D0-D5, with D0 being abnormally dry and D5 being exceptional drought, drought escalated from D0 on January 14th, 2014 to a D3 (extreme drought) by May 6, 2014. By June rainy conditions alleviated the drought conditions, and by June 24th, 2014 the drought conditions reduced to D1 (moderate drought).

Temperatures over El Reno during 2014 and 2015 were near average for the most part (Fig. 3.2). Temperatures in January and February of 2015 were above average. This led to an early sprouting of winter wheat over ICOS. Temperatures during July and early August of 2014 were about 5 degrees below normal and then a few degrees above normal during late August and September. Temperatures during 2015 were 5-10 degrees cooler than average during late May due to an abnormally wet and cloudy period. The rest of the 2015 summer had normal temperatures except for abnormally warm temperatures during August.

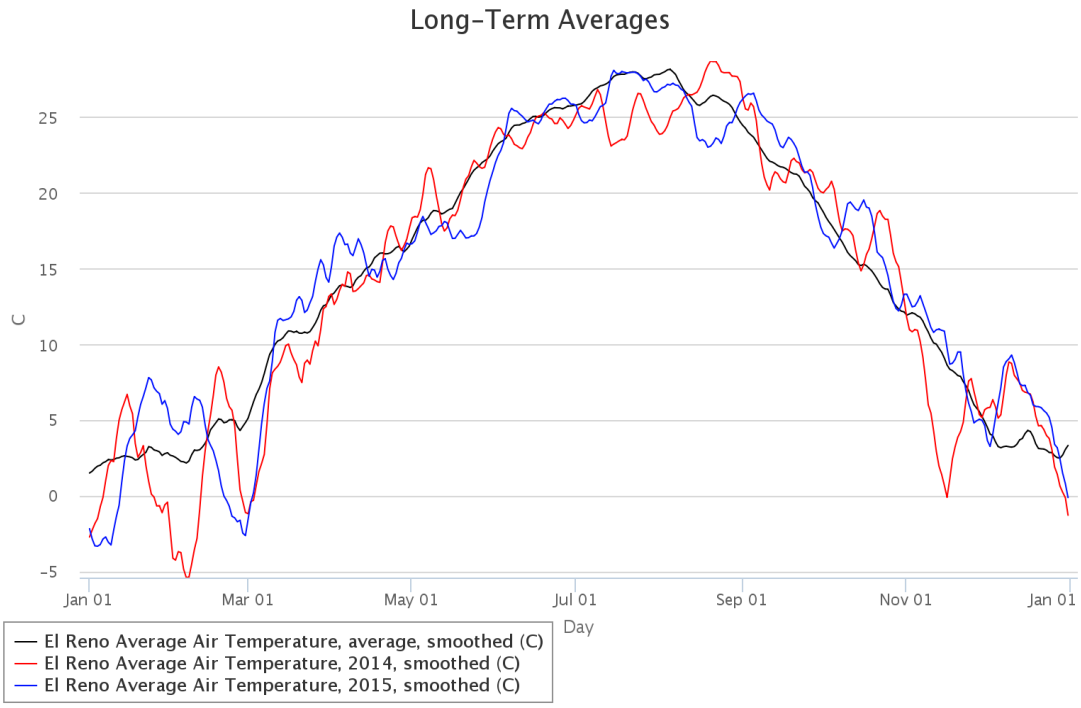

Figure 3.2: Average temperature over El Reno, Oklahoma for 2014 and 2015 compared to the average 2001-2015 rainfall distribution (source: mesonet.org)

3.1.2 Weather Conditions for Marena, Oklahoma 2012-2015

Weather conditions at Marena varied significantly between 2012 and 2015. 2012 began with above normal precipitation until June when drought developed across the SGP and persisted throughout the rest of the year (Fig. 3.3), and temperatures were above normal before and during the growing season (Fig. 3.4). 2013 had abnormally high precipitation throughout the entirety of the year, and temperatures were below average. 2014 was very dry to start the year with less than 100 mm of rain through the first five months, but the summer months were wet, and temperatures were near average. 2015 began with below average precipitation but was wetter than usual from May to September, and temperatures were near average for most of the year.

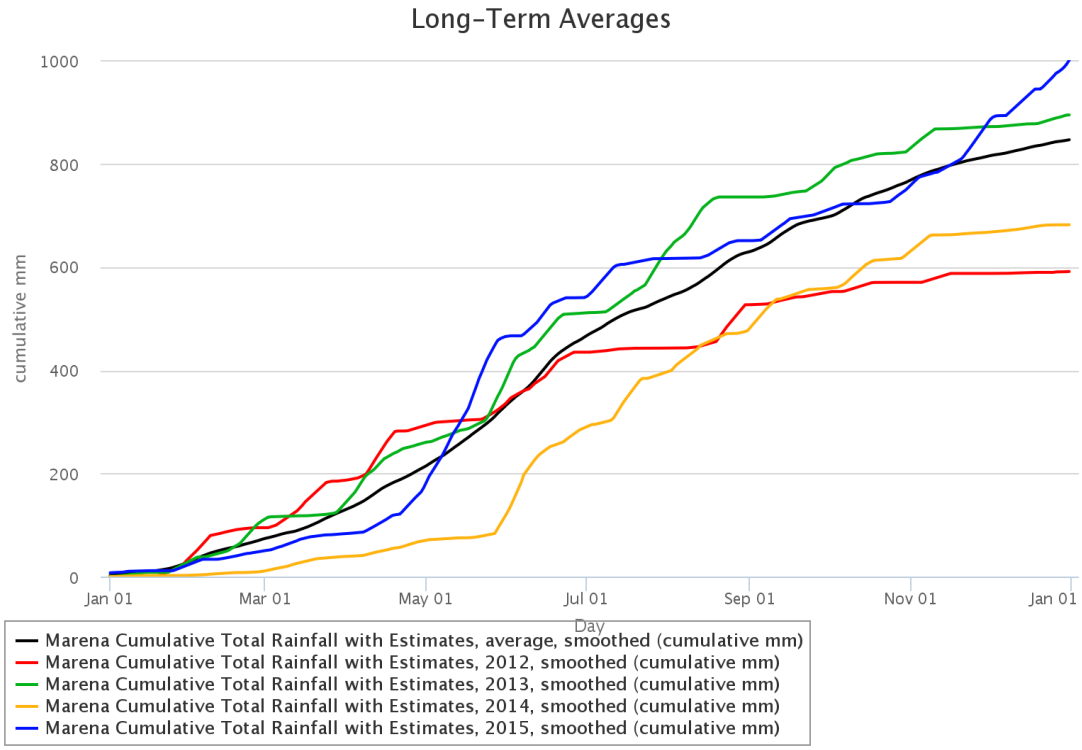

Figure 3.3: Cumulative rainfall distributions at Marena, Oklahoma for 2012-2015 compared to the average 2001-2015 rainfall distribution (source: mesonet.org).

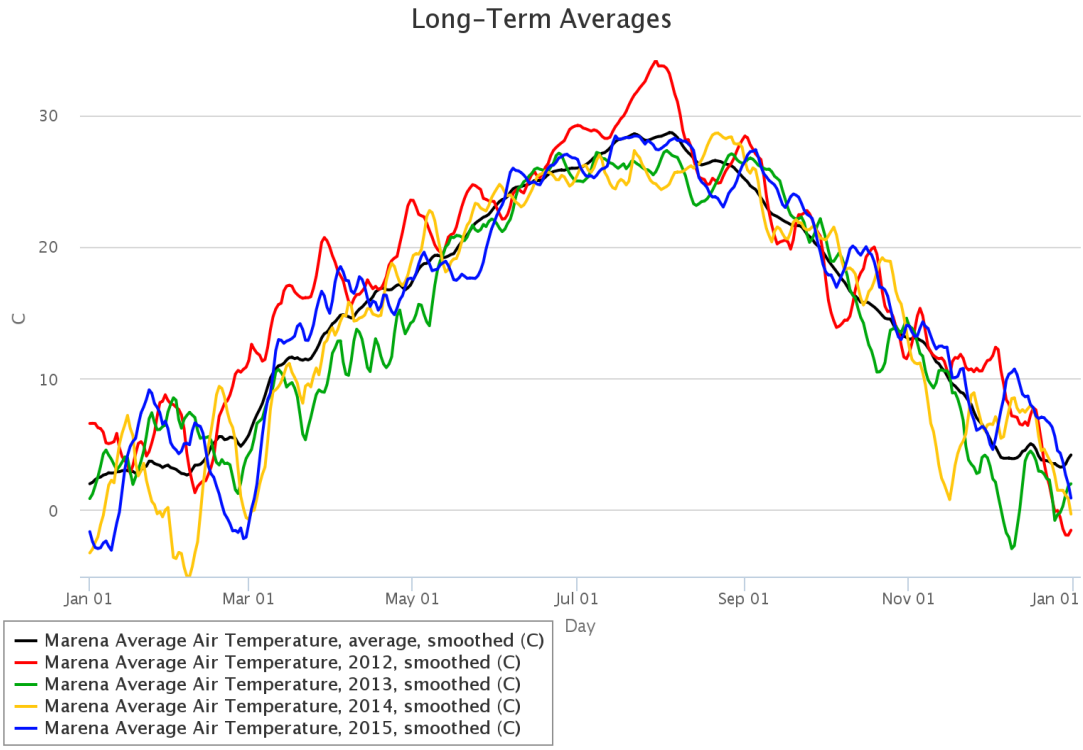

Figure 3.4: Average temperature at Marena, Oklahoma for 2012-2015 compared to the average 2001-2015 rainfall distribution (source: mesonet.org)

3.2 Collection and Data Processing Procedures

3.2.1 Data Collection

Three eddy correlation flux towers in El Reno, Oklahoma, one tower in Marena, Oklahoma and 12 additional towers from across the SGP were used in this study; the 12 additional flux towers are associated with the Ameriflux Network (Ameriflux Management Project 2016) (Table 3.1). The Ameriflux Network is a collaboration effort that incorporates flux towers from across the globe in order to help benefit the scientific community through the sharing of high quality eddy covariance data. Each

dataset acquired from the Ameriflux Network has been quality-controlled and gap-filled. The position of IGOSW, IGOSE, and ICOS are within a few kilometers of one another (Fig. 3.5). A total of 60 years of data were used in the analysis.

Table 3.1: Flux tower sites, locations, data period, and vegetation type.

Site	Location	Lat/Lon	Data Period	Vegetation
IGOS East	El Reno, OK	35.5487 -98.0376	2014-2015	Grassland
IGOS West	El Reno, OK	35.5468 -98.0453	2014-2015	Grassland
ICOS	El Reno, OK	35.5785 -98.0558	2015	Winter Wheat
Marena	Marena, OK	36.0635 -97.2170	2012-2015	Grassland
ARM SGP Main	Lamont, OK	36.6058 -97.4888	2003-2014	Winter Wheat
ARM SGP Burn	Lamont, OK	35.5497 -98.0402	2005-2006	Grassland
ARM SGP Control	Lamont, OK	35.5464 -98.0401	2005-2006	Grassland
Woodward 1	Woodward, OK	36.4267 -99.4200	2009-2012	Grassland
Woodward 2	Woodward, OK	36.6358 -99.5975	2009-2012	Grassland
Ponca Winter Wheat	Ponca City, OK	36.7667 -97.1333	2000	Winter Wheat
Kansas Field Station	Midland, KS	39.0561 -95.1907	2008-2013	Grassland
Kansas Land Institute	Salina, KS	38.7745 -97.5684	2012-2014	Grassland
Konza Prairie	Manhattan, KS	39.0824 -96.5603	2008-2014	Grassland
Konza LTER	Manhattan, KS	39.0745 -96.5951	2008-2013	Grassland
Walnut River	Smileyburg, KS	37.5208 -96.8550	2001-2004	Grassland

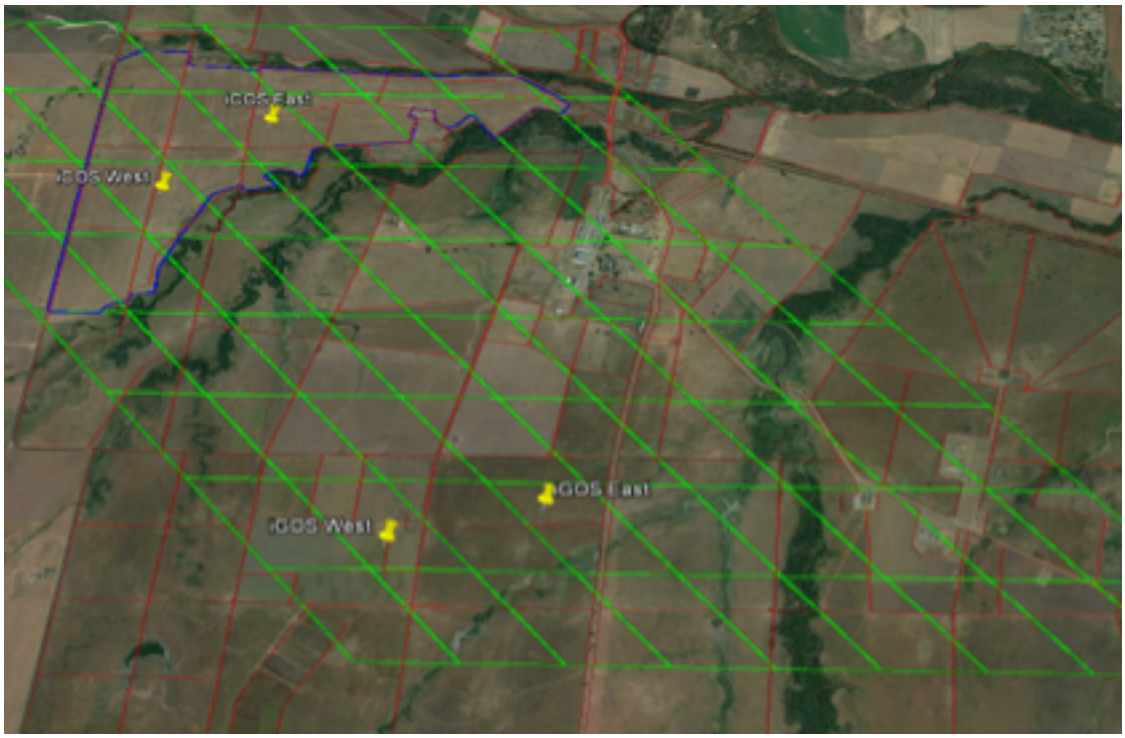

Figure 3.5: Location of the flux towers in El Reno, Oklahoma overlayed with MODIS pixels. Note: ICOS West denotes the position of ICOS and ICOS East was not installed during this study period.

Each site in El Reno and Marena, Oklahoma is equipped with a Licor LI-7500A open path CO_2 and H_20 gas analyzer, a Campbell CSAT3 sonic anemometer, soil moisture sensors, soil temperature sensors, phenological camera, and an assortment of other meteorological variable measuring instruments (Fig. 3.6). The surface conditions adjacent to each of the towers in El Reno, Oklahoma are homogenous with flat terrain (Fig. 3.6).

Figure 3.6: Eddy covariance flux tower setup (ICOS).

3.2.2 Data Footprint

The aerial extent around the flux tower that the instruments measure is called the 'flux footprint' (Burba 2013). It is important to quantify this footprint as this describes the source region of the variable measured (e.g., water vapor or carbon dioxide). In the case of eddy correlation measurements, it is difficult to determine the source region of the variables measured by the flux tower. For example, if many different vegetation types or ecosystems are within the same flux footprint then it is challenging to quantify how much each system contributed to the flux measurement. The flux footprint distance is a function of the surface roughness, atmospheric stability, and sensor measurement height. Thermal stability is an important indicator of the fetch. For very unstable conditions and an instrument at 1.5 meters above a 0.6 meter canopy, most of the footprint falls within a 50 meter radius of the tower. This can bias the data due to the

disturbed environment near the tower caused by maintenance and tower facilities. Very stable conditions will create a footprint of up to 500 meters and can entrain gases from different source regions that can bias the data if the focus area is smaller than the fetch. Neutral conditions will create a fetch radius of approximately 250 meters. A general 100 to 1 fetch-to-height ratio is applied to determine how high to place an instrument to sample a large majority of the flux footprint within neutral conditions (Leclerc and Thurtell, 1990). Equation 3.1 was used to compute the flux footprint under neutral conditions of the flux towers used in this study (Schuepp et al. 1990)

$$\boldsymbol{CNF(x_L) = -\int_0^{x_L} \frac{U(z-d)}{u_* k x^2} e^{\frac{-U(z-d)}{u_* k x}} dx = e^{\frac{-U(z-d)}{u_* k x_L}}} \quad \textbf{(3.1)}$$

where CNF is the cumulative normalized contribution to flux measurement (%), x_L is distance from the station (m), U is the mean integrated wind speed (m s^{-1}), z is measurement height (m), u_* is friction velocity (m s^{-1}), d is zero plain displacement (m), and k is the von Karman constant (0.4). For the towers at El Reno and Marena, Oklahoma the measurement height is 2.5 meters. At this height, approximately 80% of the fetch is within 200 meters upwind of the tower (Fig. 3.7).

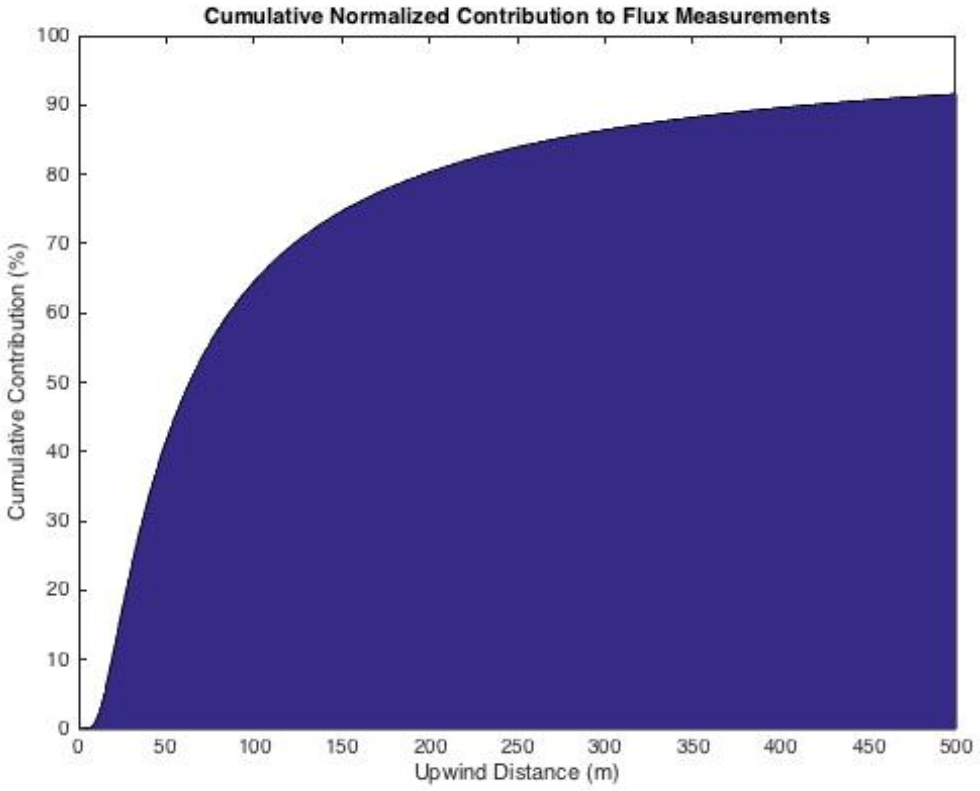

Figure 3.7: Cumulative Normalized Contribution of measurements within an upwind distance of the flux towers in El Reno and Marena, Oklahoma with a measurement height of 2.5 meters.

3.2.3. Quality Control and Gap-Filling

Eddy covariance instrumentation is sensitive and requires ideal atmospheric conditions to collect research quality data. While most conditions are acceptable for flux measurements, during periods of rain or very stable/unstable conditions, the quality of the data can be compromised. Additionally, non-meteorological factors can influence measurements, such as battery failure, sensor malfunction, or datalogger connectivity issues. It is important to account for these factors to adequately correct the data and assemble as complete of a dataset as possible. The data was processed using the Eddy

Pro software package that computes the fluxes and quality controls them by removing outliers, performing coordinate rotations, and assessing density irregularities.

A gap-filling scheme developed by the Max Planck Institute of Biogeochemistry based on the research of Falge et al. (2001) and Reichstein et al. (2005) was used to gap-fill missing data. The scheme uses a look-up table with a moving window to fill the gaps (Fig. 3.8). Three critical conditions are identified in a hierarchical order:

- Condition 1 states that if meteorological data is available (radiation, air temperature, and vapor pressure deficit) then the data of interest (i.e. LE or NEE) can be filled by using a look-up table (LUT) and a moving time window. If condition 1 does not exist then condition 2 will be executed.
- Condition 2 states that if only radiation is available then the same LUT method is applied. If condition 1 and 2 do not exist then condition 3 is executed.
- Condition 3 states that if radiation is also missing then the missing value is replaced by the average value at that time of day over the 7 days in the window. If there is still a missing value after these steps then each step will be repeated with a larger time window until the values are replaced.

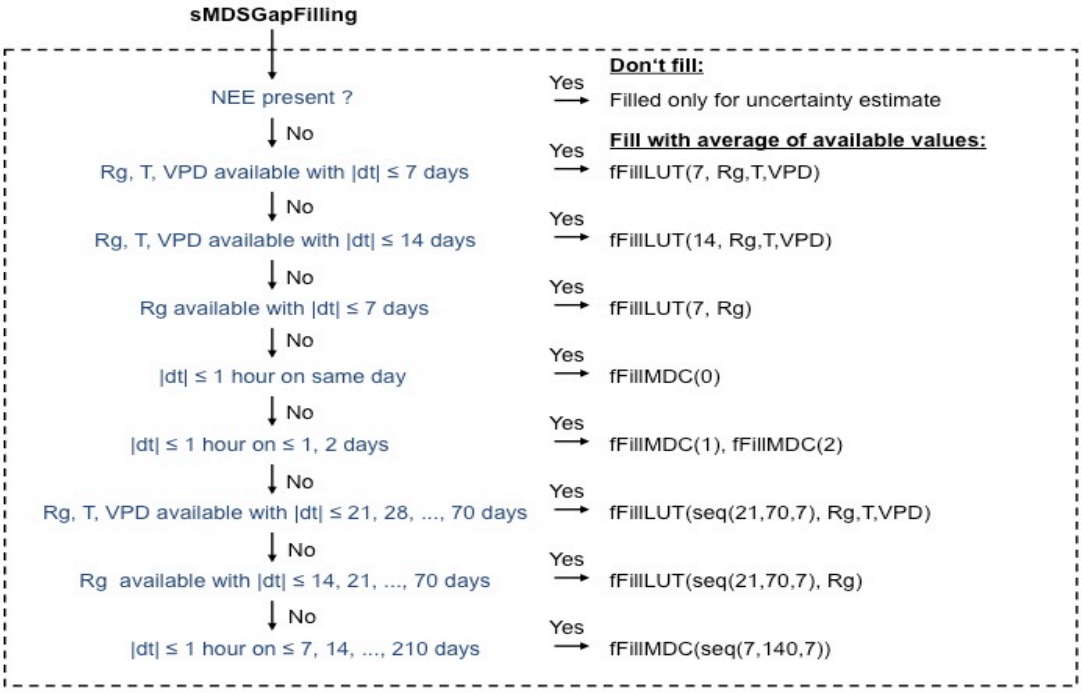

Figure 3.8: A flow diagram describing the conditions and scheme used by the gap-filling scheme. In this case, ET is gap-filled, not NEE (retrieved from https://www.bgc-jena.mpg.de/bgi/index.php/Services/REddyProcWebGapFilling).

3.3 TSEBS Model

TSEBS is a two-source land surface model

$$LE_C = R_{N,C} - H_C \quad (3.2)$$

$$LE_S = R_{N,S} - G - H_S \quad (3.3)$$

where LE_C and LE_S are latent heat fluxes for the canopy and surface, respectively; R_N is the net radiation for canopy and surface; G is ground heat flux; and H is the sensible heat for the canopy and surface (Norma et al. 1995; Colaizzi et al. 2012; Colaizzi et al. 2016). Landsat 5/8 thermal imagery is used as input data for TSEBS (Gowda et al. 2016). Instantaneous ET was interpolated to daily ET using an evaporative fraction with

a daily reference ET hybrid model (Allen et al. 2005). After investigating the model's pixels around each tower in 2014 it was determined that a 3x3 pixel yielded sufficient representation of the flux footprint, given that the pixels are over homogenous vegetation they are very similar to their neighboring pixels.

3.4 Wagle Model

The Wagle ET Model was constructed with a training dataset over grassland sites in the SGP. This model is a function of PAR and EVI where:

$$\mathbf{EVI} = \frac{\mathbf{2.5}*(\mathbf{NIR}-\mathbf{RED})}{\mathbf{NIR}+\mathbf{6}*\mathbf{RED}-\mathbf{7.5}*\mathbf{BLUE}+\mathbf{1}} \quad \textbf{(3.4)}$$

where NIR is the near-infrared spectral band, RED is the red spectral band, and BLUE is the blue spectral band. The Wagle ET model is defined as

$$\mathbf{ET = 0.11*PAR + 5.49*EVI - 1.43} \quad \textbf{(3.5)}$$

Both of PAR and EVI can be derived from MODIS observations allowing for large spatial scale evaluation of ET. Since this model was created using a training dataset of grassland flux data it is only applicable for grassland regions. Only the grassland sites from El Reno, Marena, and the Ameriflux sites were compared to this model. MODIS EVI was used as the EVI input into the model. PAR was derived from MODIS using the Forest Light Environmental Simulator (FLiES) (Kobayashi and Iwabuchi, 2008). Subsequently, ET values every 8 days were computed using the model.

3.5 BESS

BESS is a process-based model that couples atmosphere and canopy radiative transfer, photosynthesis and evapotranspiration, and uses MODIS atmosphere and land

data paired with meteorological reanalysis data as inputs (Fig. 3.9). BESS provides estimates of GPP, the amount of carbon absorbed by the ecosystem, and ET on a 1km spatial scale and an 8-day temporal scale that can be further scaled to daily, weekly, monthly, annual, or decadal scales. BESS essentially has three layers: above canopy layer, canopy layer, and below canopy layer.

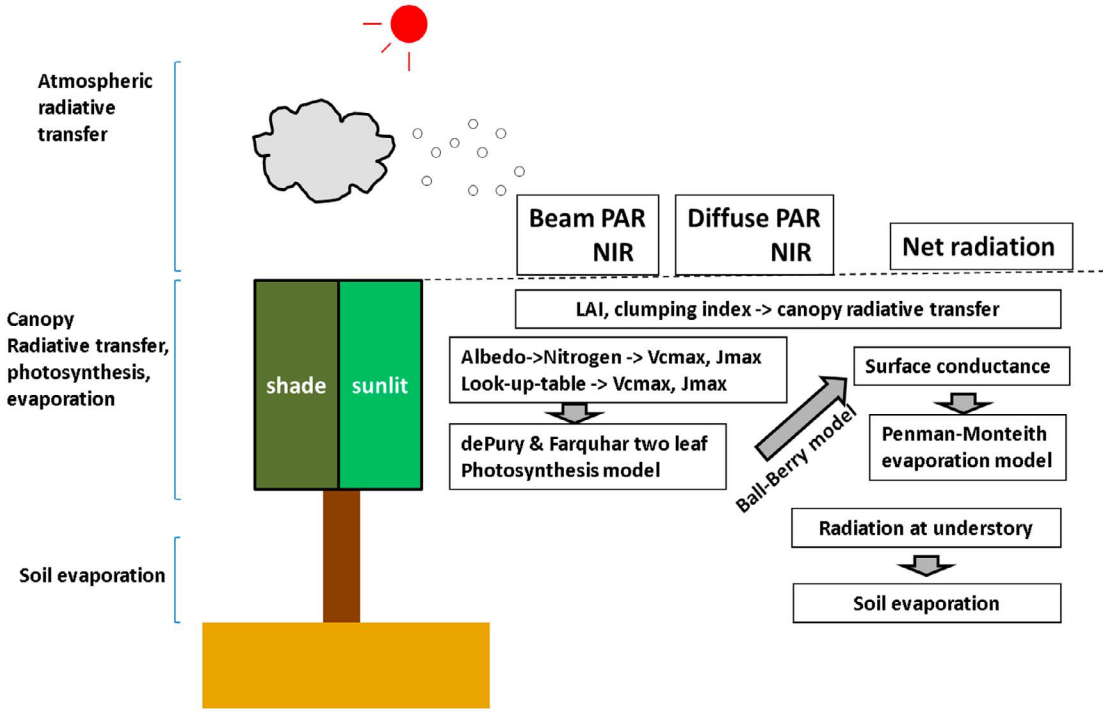

Figure 3.9: Model layers of BESS (Ryu et al. 2011).

The above canopy layer consists of an atmospheric radiative transfer model called the Forest Light Environmental Simulator (FLiES) developed by Kobayashi and Iwabuchi (2008). This model calculates the incoming shortwave radiation, photosynthetic active radiation (PAR), and near-infrared radiation (NIR) at the top of the canopy. The input variables for this model are derived from MODIS data streams:

MOD04 (aerosol optical thickness), MOD06 (solar zenith angle, cloud optical thickness, cloud top height), and MCD43 (albedo).

The canopy layer is comprised of several models. A two-leaf canopy radiative transfer model that calculates PAR, NIR, and longwave radiation for sunlit and shaded leaves. A photosynthesis model computes the photosynthesis of C3 and C4 plants (Collatz et al. 1991; Farquhar et al. 1980; Collatz et al. 1992) based off of the proportion of C3 and C4 plants per pixel. Two-leaf canopy latent heat flux is computed using a quadratic form of the Penman-Monteith equation (Monteith, 1965; Paw U and Gao, 1988)

$$\boldsymbol{a\lambda E_j^2 + b\lambda E_j + c = 0}$$

(3.6a)

where

$$\boldsymbol{a = \frac{r_a^2}{2[\rho_a C_p \gamma (r_a + r_{c,j})]} \frac{d^2 e_s(T_a)}{dT_a^2}}$$

(3.6b)

$$\boldsymbol{b = -1 - r_a \frac{de_s(T_a)}{dT_a} \frac{1}{\gamma (r_a + r_{c,j})} - \frac{R_{n,j} r_a^2}{\rho_a C_p \gamma (r_a + r_{c,j})} \frac{d^2 e_s(T_a)}{dT_a^2}}$$

(3.6c)

$$\boldsymbol{c = \frac{\rho_a C_p D}{\gamma (r_a + r_{c,j})} + \frac{r_a R_{n,j}}{\gamma (r_a + r_{c,j})} \frac{de_s(T_a)}{dT_a} + \frac{1}{2} \frac{(r_a \times R_{n,j})^2}{\rho_a C_p \gamma (r_a + r_{c,j})} \frac{d^2 e_s(T_a)}{dT_a^2}}$$

(3.6d)

where r_a and $r_{c,j}$ are aerodynamic and canopy resistance (j stands for the sunlit and shaded leaf), respectively; ρ_a is the density of air; γ is the psychrometric constant; $e_s(T)$ is saturated vapor pressure at a given temperature, T; R_n is the net radiation (Henderson-Sellers, 1984; Ryu et al. 2012). The below canopy layer is comprised of a soil

evaporation model that is forced by the amount of soil water that is a function of the soil litter layer (Ryu et al. 2011). Soil evaporation was computed with a soil water stress function $RH^{D/1000}$ from Fisher et al. (2008)

$$\boldsymbol{\lambda E_{soil} = \frac{s}{s+\gamma}(R_{n,soil} - G_{soil}) \times RH^{D/1000}}$$

(3.7a)

where

$$\boldsymbol{R_{n,soil} = R_n - (R_{n,sun} + R_{n,shade})}$$

(3.7b)

$$\boldsymbol{G_{soil} = 0.35 \times R_{n,soil}}$$

(3.7c)

and where $R_{n,soil}$ is the net radiation at the soil surface, and G_{soil} is the soil heat flux.

Chapter 4 : In-Situ Flux Measurements

4.1 Flux Tower Measurements

Three towers at the USDA site in El Reno, Oklahoma were deployed over native grassland, improved grassland, and winter wheat, and one tower near Marena, Oklahoma was deployed over native grassland. The two grassland sites at El Reno collected data during the growing season from 2014-2015 while data was only collected during the growing season of 2015 at the winter wheat site because there was no collection of data until after senescence and harvest in 2014. The Marena site collected data from 2012-2015.

4.1.1 Energy Balance Closure

Energy balance closure was used to verify the data quality at each site location. Monthly and annual cycles of the surface energy budget were compared for each year at each site. Diurnal and seasonal variations of water and carbon fluxes were analyzed and compared over all of the sites and years. From equation 2.2, net radiation is partitioned into latent heat flux, sensible heat flux, and ground heat flux. By measuring net radiation, latent heat flux, sensible heat flux, and ground heat flux it is easy to determine what percentage of the total net radiation is measured by the instruments; this is known as energy balance closure (EBC) (Burba, 2013). The EBC is quantified by comparing the difference between available energy ($R_n - G$), to the sum of latent and sensible heat flux (Fig. 4.1). Ideally, available energy should be equal to the sum of latent heat flux and sensible heat flux, and when plotted versus one another should exhibit a slope of 1 and an intercept of 0 (Wilson et al. 2001). However, this is typically not the case when it comes to eddy covariance measurements. The eddy covariance tower usually does not

measure all of the latent and sensible heat fluxes due to instrument error, uneven terrain, and canopy energy storage (Burba, 2013). EBC can range between 55%-99% (Wilson et al. 2002) and typically over grasslands, the EBC averages between 70-80% (Twine et al. 2000). Similar research done over central Oklahoma found EBC of 77% over a switchgrass field (Wagle et al. 2012).

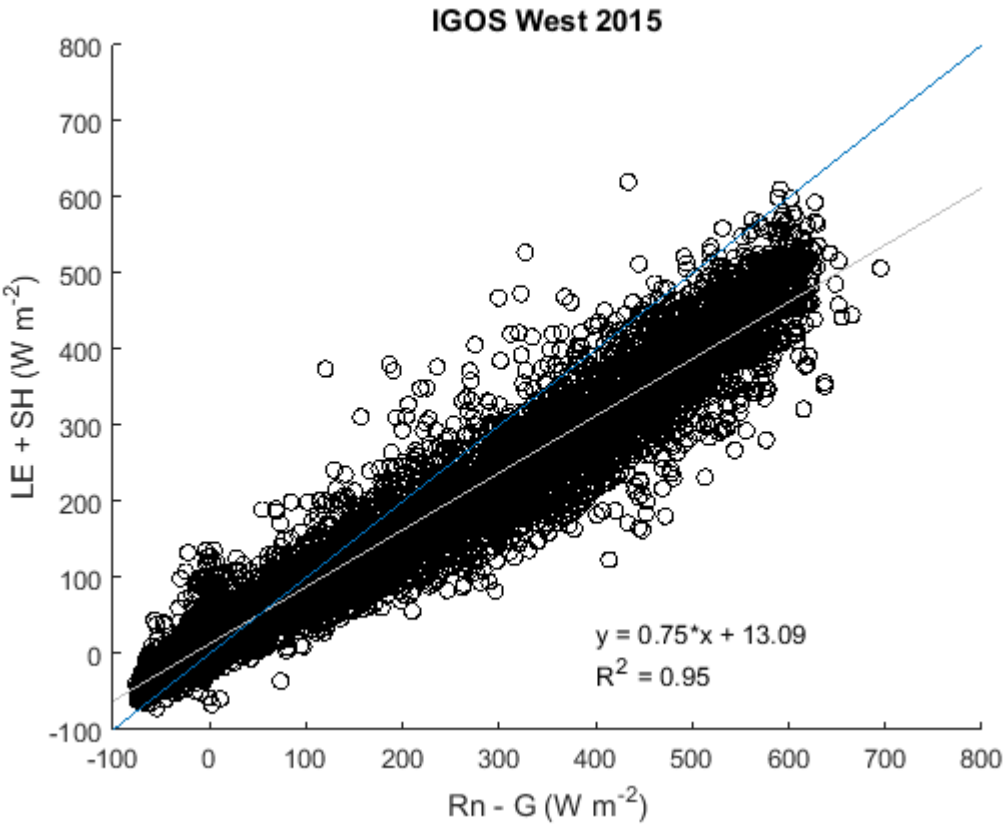

Figure 4.1: Energy Balance Closure over IGOS West in El Reno, Oklahoma during 2015. There is 75% closure over IGOS West during 2015.

For the IGOS, ICOS, and Marena sites the EBC ranged from 59% closure to 91% closure (Table 4.1). Figure 4.1 shows that there was 75% closure at IGOS West in 2015. This shows that the eddy covariance tower is unable to explain where 25% of the available energy was partitioned (latent heat flux or sensible heat flux). IGOS East for

2014 and 2015 has closure values of 91% and 83%, respectively. Because both sites have near homogeneous vegetation, the most likely reason for the observed differences is due to the terrain of IGOS West compared to IGOS East. IGOS East is located in a low-lying flat area with limited topographical features. However, IGOS West has more sloping topographical features that can result in lower closure values.

Similar to IGOS East, ICOS has a high closure rate (85%). ICOS has flat topography and because it is a crop field, the vegetation is more homogenous than any of the other sites. Overall, these EBC values validate that the site data is of good quality when compared to other studies. The low values over the Marena site (EBC ~ 60%) are most likely a result of uneven terrain, inhomogeneous vegetation, and the data having not been processed with the Eddy Pro software (unavailable at the time of data collection). For Marena, it is best to interpret the overall trends and variability of the fluxes rather than the magnitude. Additional figures corresponding to Figure 4.1 for the other sites/years can be found in Appendix A.

Table 4.1: EBC for each site/year at El Reno and Marena, Oklahoma.

Site	Date	Energy Balance Closure
IGOS East	2014	91%
IGOS East	2015	83%
IGOS West	2014	74%
IGOS West	2015	75%
ICOS	2015	85%
Marena	2012	59%
Marena	2013	59%
Marena	2014	62%
Marena	2015	59%

4.1.2 Monthly Cycles of the Surface Energy Budget

The net radiation in equation 2.2 is largely partitioned into latent heating, sensible heating, and ground heating. Figures 4.2-4.10 show how energy was partitioned during daytime hours at each flux tower site for each year. As expected, net radiation peaks at ~160 W m^{-2} day^{-1} at each during June and July.

Latent heating is typically the primary sink of the net radiation for a majority of the year at the grassland and cropland sites. This is especially the case at IGOS East and West in 2014 and 2015 (Figs. 4.3-4.6). During the growing season more energy was partitioned into latent heating than any of the other terms. On the contrary, during the dormant season (Figs. 4.5-4.9) the sites yielded higher sensible flux during this time because of the lack of LH due to dormant vegetation. For dry years, such as Marena 2012 (Fig. 4.7), the magnitude of latent heat flux was significantly lower compared to

other years. In fact, the sensible heat flux became the dominant term in July and August when flash drought occurred (Mo an Lettenmaier 2015; Otkin et al. 2013a). For wet years during the growing season, such as 2015 (Fig. 4.4 and 4.6), the latent heat flux can expend almost all of the downwelling net radiation. In the vegetated areas, the ground heat flux contributed very little to the partitioning of net radiation with values between -10 and 10 W m^{-2} day^{-1} (Fig. 4.2-4.10).

The ICOS site behaved differently than the grassland sites (Fig. 4.2). Because this site is composed of winter wheat the growing season is between February and June. Maximum values of latent heating (60 W m^{-2} day^{-1}) occurred in April. During May the winter wheat begins to senesce and dry which leads to lower latent heating and higher sensible heating. Winter wheat in central Oklahoma is typically harvested during June and after harvest the surface albedo, latent heat flux, and sensible heat flux change dramatically due to the bare soil. Depending on whether the agricultural practice of a certain field is to till or remain untilled will determine, in part, if native vegetation and grasses replace the barren land. These various land uses further affect the surface energy budget for a large portion of the SGP that is occupied by winter wheat.

As seen in the EBC values, not all of the incoming energy is measured by the flux towers. It is unclear as to where this unaccounted energy is partitioned. Most land surface models distribute this residual term (i.e., the unaccounted energy) based on the Bowen ratio, the ratio of sensible to latent heat. However many have argued that this may not be an accurate assumption (Foken 2008; Foken et al. 2011). Foken (2008) hypothesizes that the most likely cause for EBC disagreement is large scale eddies. The eddy covariance flux measuring systems are able to capture small scale eddies, but they

are unable to capture large scale eddies that can advect trace gases away from the sensors. Instrumentation error has been dismissed as a major source of error in eddy covariance measurements when the instruments are properly calibrated and data has been properly screened and calculated (Foken et al. 2011). Overall, energy balance closure and how to distribute the residual term of the surface energy budget is still an unsolved problem (Foken et al. 2011). Therefore, the residual term is left undistributed in this dataset (Fig. 4.2-4.10). The residual term is lower for the ICOS and IGOS sites than the Marena sites because of the better flagging and screening of the data with the help of the Eddy Pro software.

The most complete dataset with the highest EBC is IGOS West during 2015 (Fig. 4.6). Hence, it is best to use IGOS West 2015 as a representation of the average surface energy partitioning in grassland regions over Oklahoma during a wet year. For this site, net radiation varied between 50 W m^{-2} day^{-1} in the winter and 160 W m^{-2} day^{-1} during the summer. Latent heating ranged between 15 W m^{-2} day^{-1} during the winter and 120 W m^{-2} day^{-1} during the summer. Sensible heating is inversely related to latent heating, therefore sensible heating was typically the dominant term in the wintertime near 45 W m^{-2} day^{-1} and was near 5-10 W m^{-2} day^{-1} during the wet summer months. The ground heat flux remained relatively constant throughout the year with a slight minimum in the winter and slight maximum in the summer.

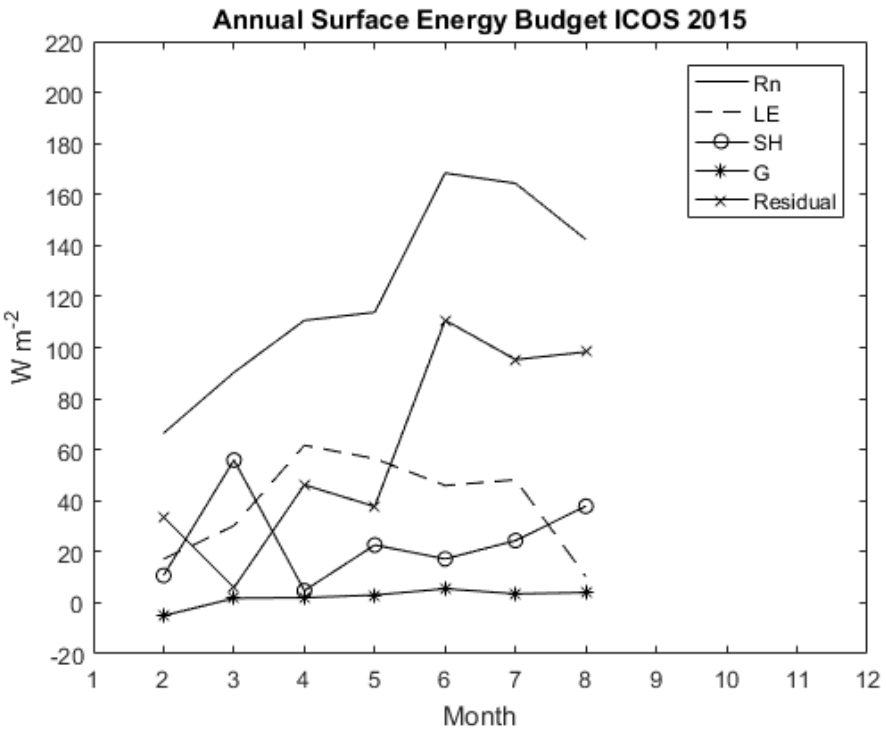

Figure 4.2: Monthly mean daily values of each variable in the surface energy budget equation and the residual of net radiation for ICOS 2015.

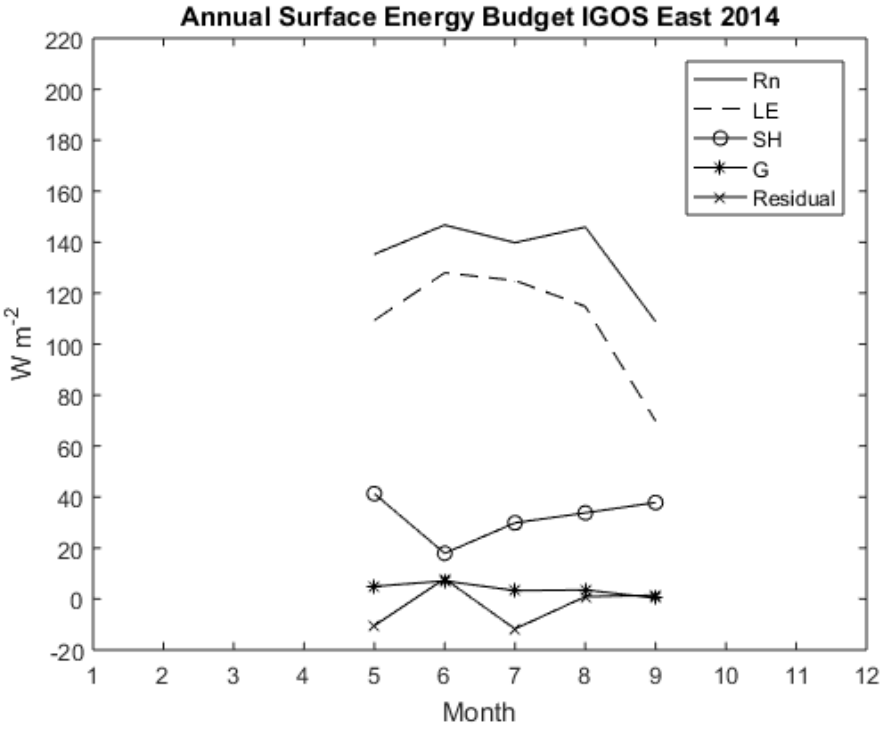

Figure 4.3: Monthly mean daily values of each variable in the surface energy budget equation and the residual of net radiation for IGOS East 2014.

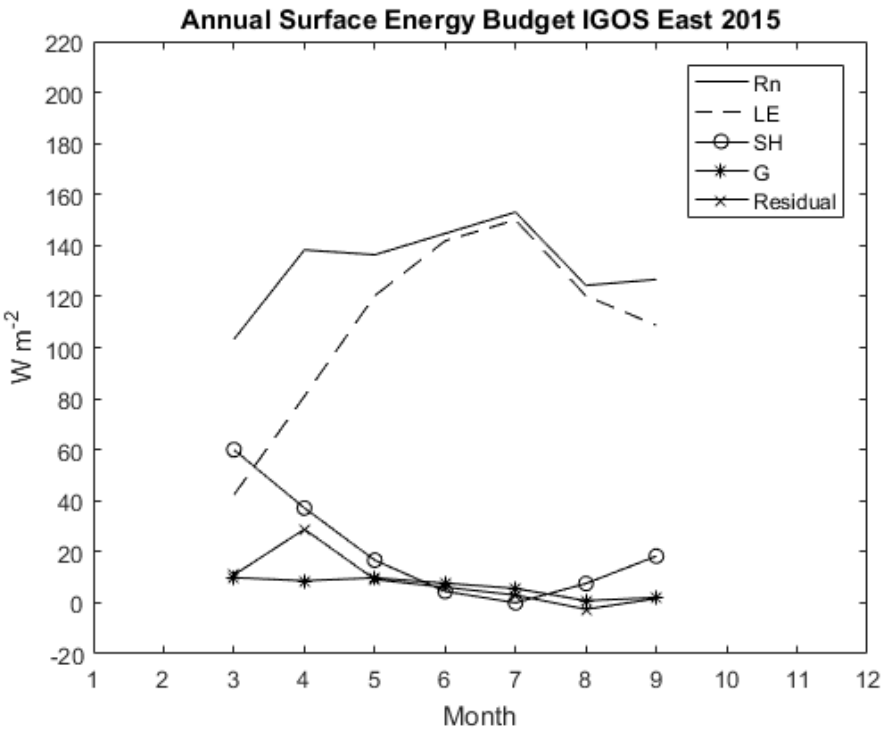

Figure 4.4: Monthly mean daily values of each variable in the surface energy budget equation and the residual of net radiation for IGOS East 2015.

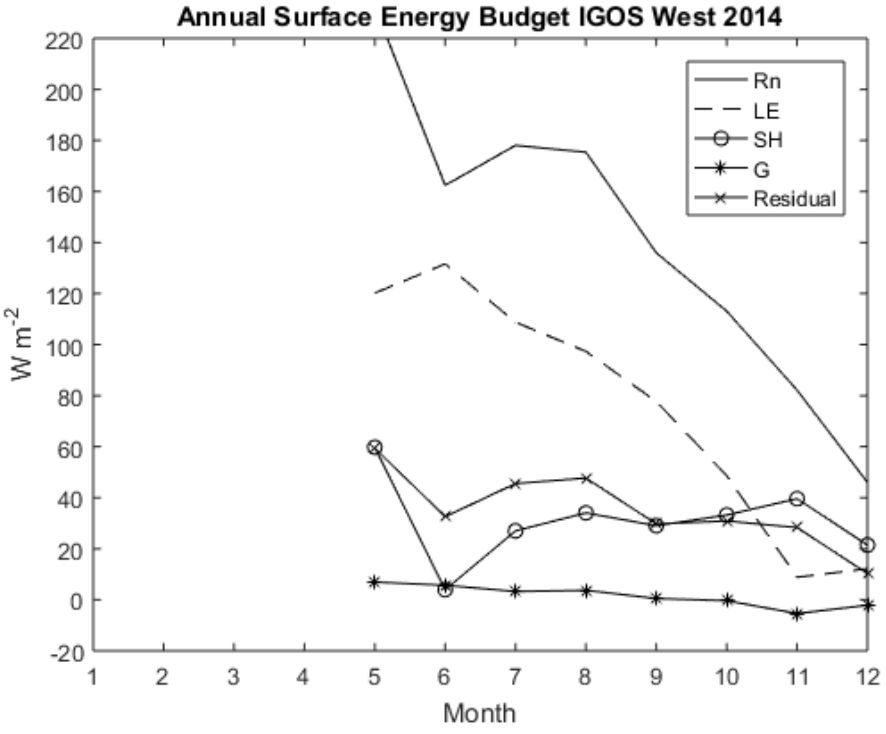

Figure 4.5: Monthly mean daily values of each variable in the surface energy budget equation and the residual of net radiation for IGOS West 2014.

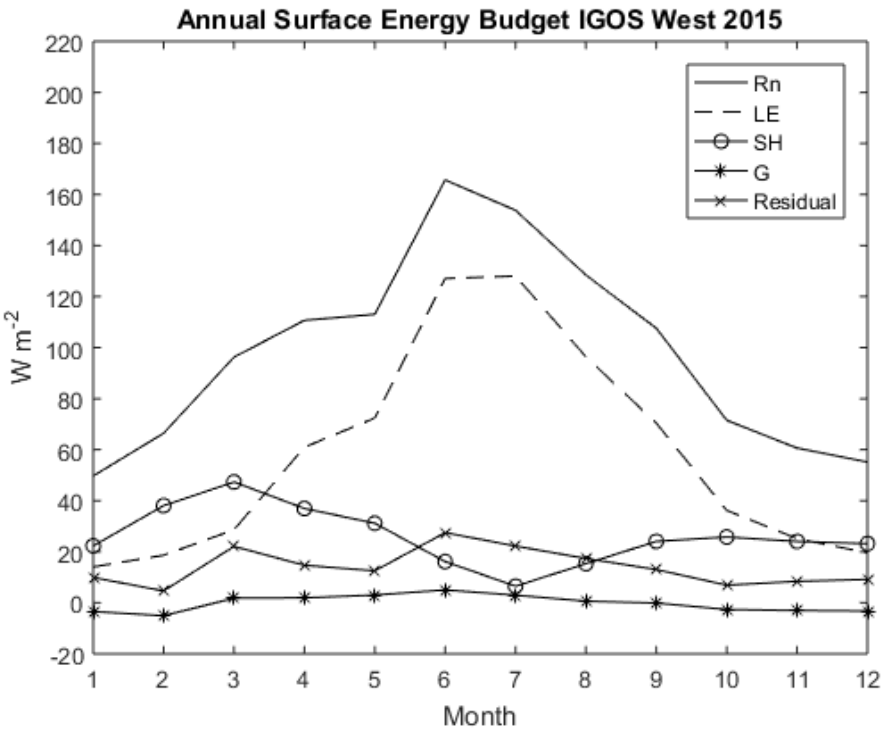

Figure 4.6: Monthly mean daily values of each variable in the surface energy budget equation and the residual of net radiation for IGOS West 2015.

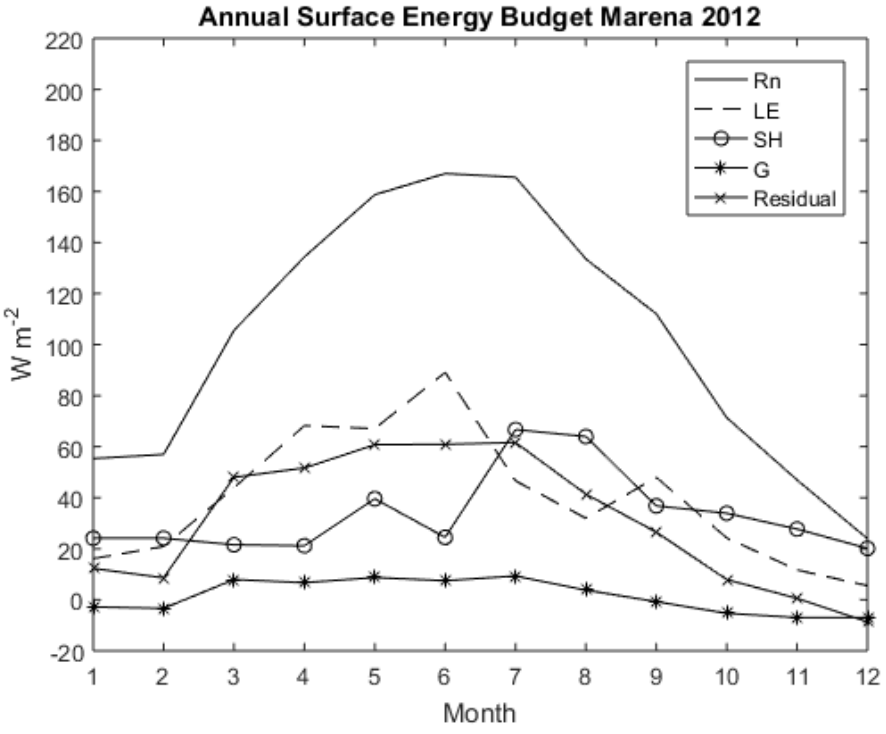

Figure 4.7: Monthly mean daily values of each variable in the surface energy budget equation and the residual of net radiation for Marena 2012.

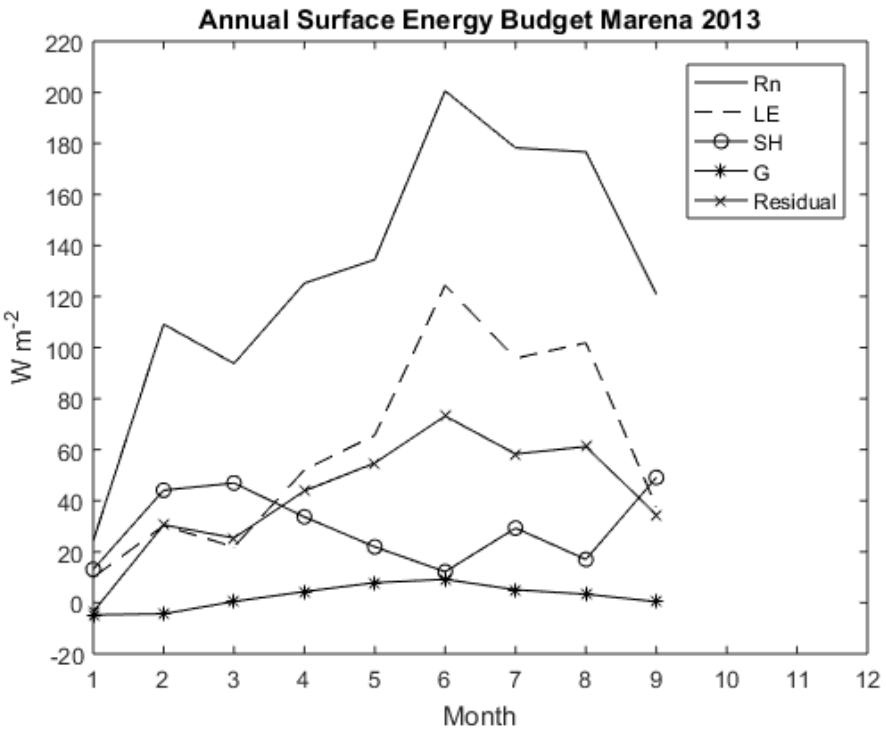

Figure 4.8: Monthly mean daily values of each variable in the surface energy budget equation and the residual of net radiation for Marena 2013.

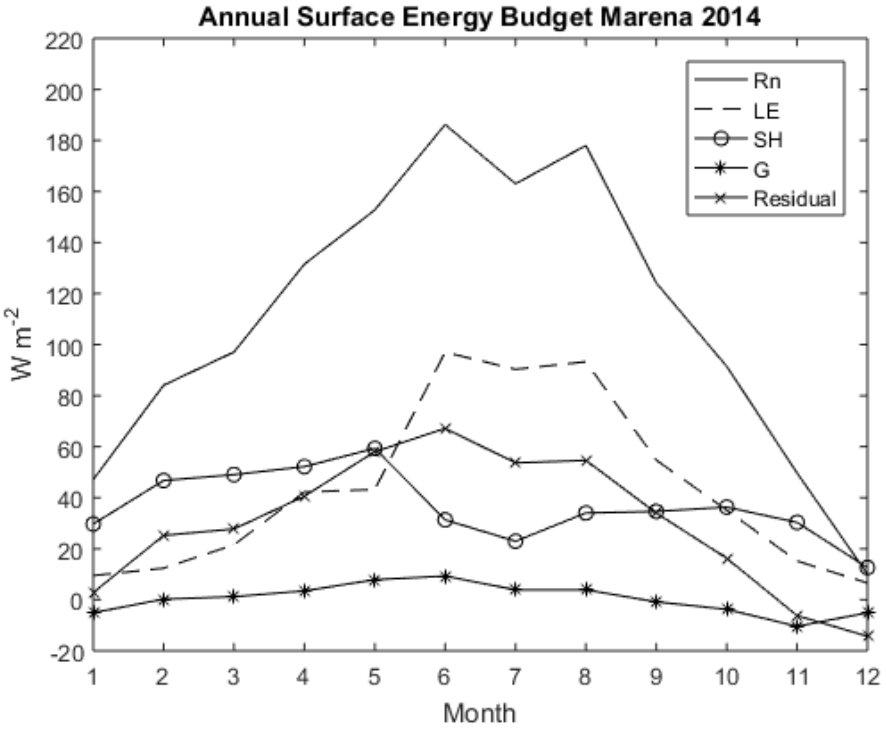

Figure 4.9: Monthly mean daily values of each variable in the surface energy budget equation and the residual of net radiation for Marena 2014.

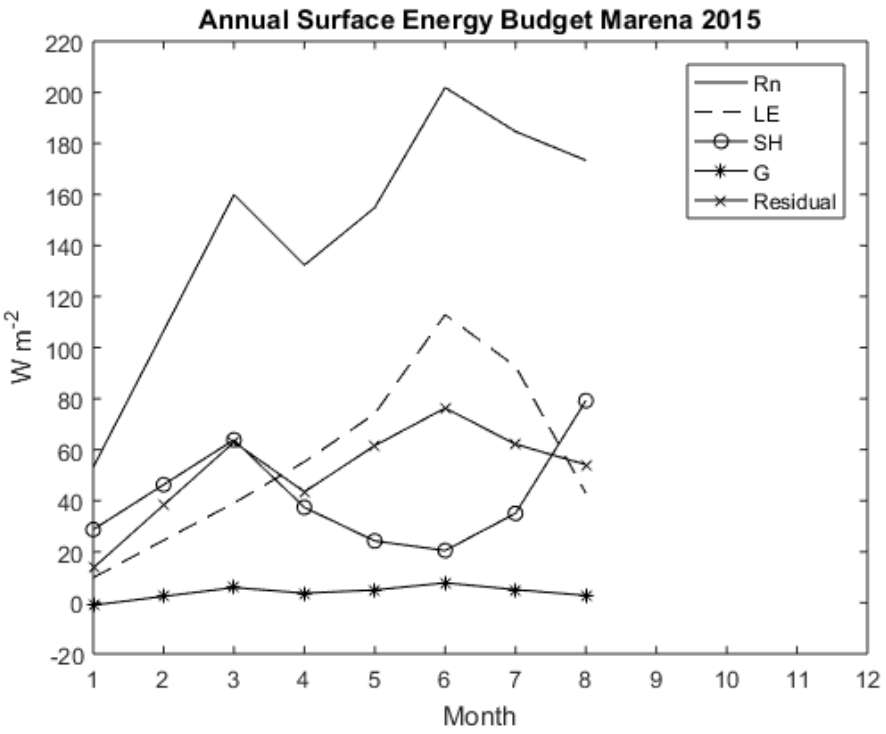

Figure 4.10: Monthly mean daily values of each variable in the surface energy budget equation and the residual of net radiation for Marena 2015.

4.1.3 Diurnal Patterns of Evapotranspiration

The diurnal pattern of ET describes how ET varies throughout a 24-hour day. Figures 4.11-4.17 show how ET varies on average per month for each of the sites in the dataset. Every site had nearly the same diurnal cycle. Little ET was measured during the overnight hours, corresponding to no incoming radiation while the peak rate of ET occurred during midday when net radiation was at a maximum. Symmetrical increases and decreases in ET surrounded the apex in ET of the diurnal curve.

The diurnal pattern of ET for ICOS 2015 from February-August (Fig. 4.11) peaked during the months of April and May at 0.12 mm $30min^{-1}$; this corresponds to a mature winter wheat crop, which has an earlier growing season than native grasses. This earlier growing season is most evident in March when ET rates were near 0.08 mm

30min^{-1} compared to 0.04 mm 30min^{-1} at the IGOS sites (Figs. 4.12 & 4.13). Because the maturity of the crop occurs in April and early May, the maximum values of ET during the middle of the day was 0.12 mm 30min^{-1}. After harvest the field was left fallow and native grasses replaced the empty field quickly. These grasses kept ET rates near 0.08 mm 30min^{-1}. However, during August the ET rates were near 0 mm 30min^{-1} as a result of tilling in preparation for the next crop planting.

The diurnal pattern of ET at the IGOS sites was similar but the magnitude was different. Unlike the ICOS site, IGOS West and East have maximum ET rates in June and July when the grasslands reached maturity and the radiation budget is highest. IGOS East had higher rates of ET (0.32 mm 30min^{-1}) compared with IGOS West (0.27 mm 30min^{-1}) during June and July. Further, IGOS East had higher ET rates in August (0.27 mm 30min^{-1}) than those at IGOS West (0.20 mm 30min^{-1}). September had similar ET rates, however October had slightly higher ET rates at IGOS West (0.07 mm 30min^{-1}) compared to IGOS East (0.05 mm 30min^{-1}).

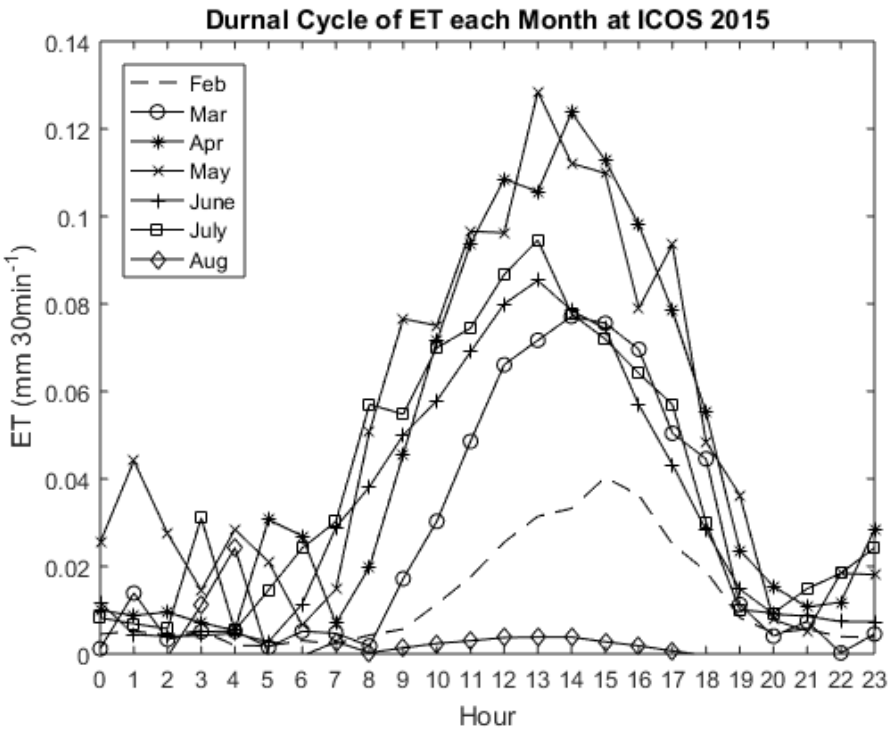

Figure 4.11: Diurnal pattern of ET values each month of the dataset at ICOS 2015.

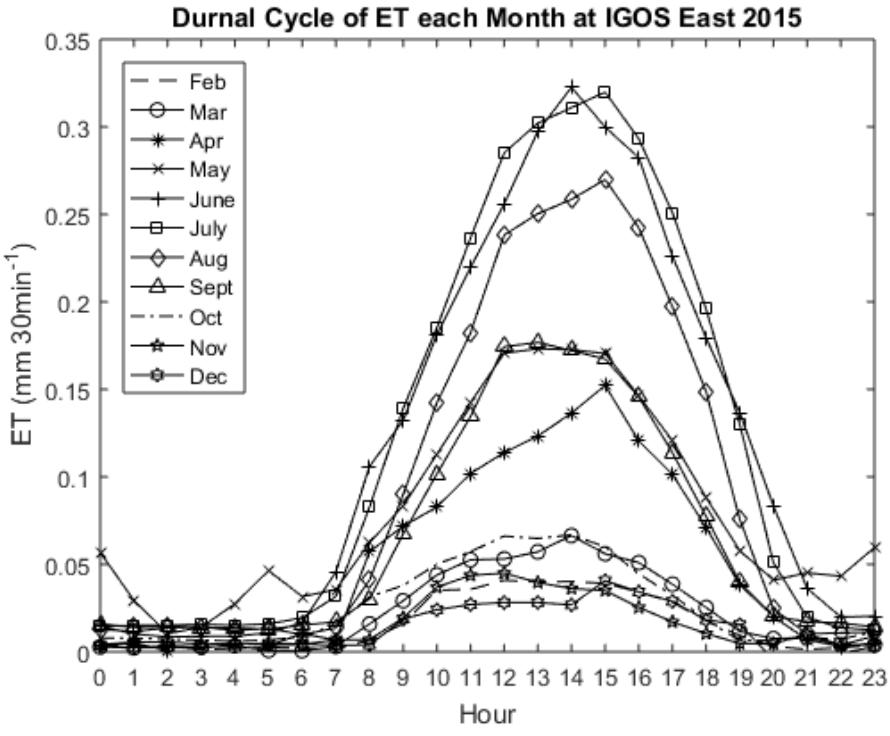

Figure 4.12: Diurnal pattern of ET values each month of the dataset at IGOS East 2015.

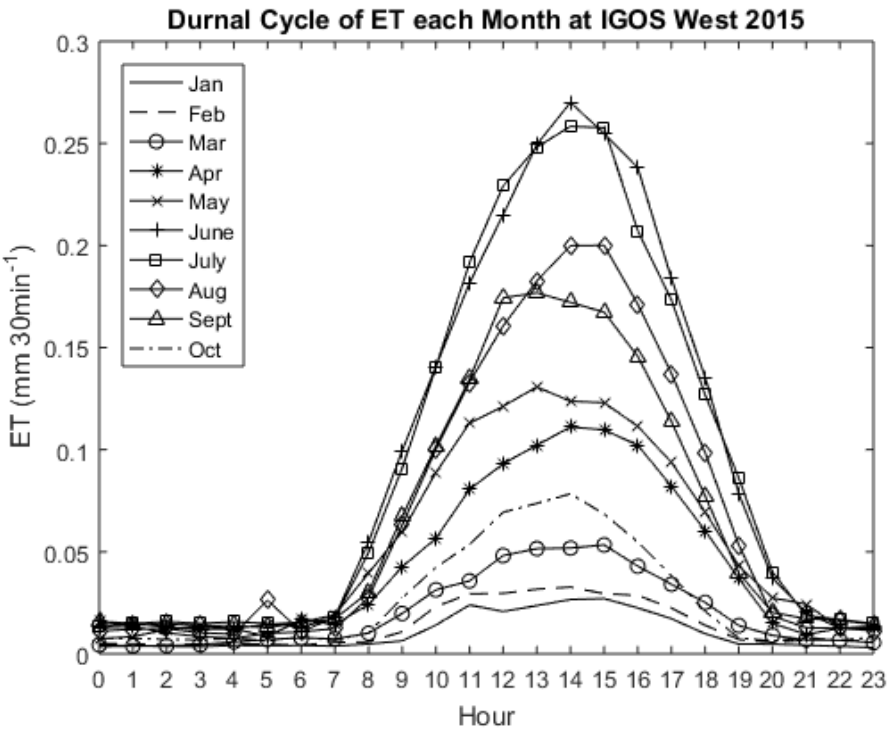

Figure 4.13: Diurnal pattern of ET values each month of the dataset at IGOS West 2015.

The Marena grassland site (Fig. 4.14-4.17) had lower magnitudes of ET rates compared to the IGOS sites (< 0.23 mm 30min^{-1}). These lower ET rates could be related to the lower EBC at the site. Considering that 40% of the available energy is unaccounted for, it is likely that a portion of that was used for latent heating. Further, drought conditions occurred in 2012 at the Marena site. During 2012 ET rates were highest in September (0.18 mm 30min^{-1}), but for non-drought years (Fig. 4.15 & 4.17) the rates were highest in June. July and August of 2012 ET rates were significantly lower than normal (> 0.1 mm 30min^{-1}). These abnormally low values are a result of flash drought that occurred in 2012. In addition, 2014 (Fig. 4.16) was also a drought year throughout the first five months (Fig. 3.3), but a wet June increased the ET rates from 0.08 mm 30min^{-1} to 0.18 mm 30min^{-1}. The increase in soil moisture also affected

the rest of the summer months by keeping ET rates higher than the first half of the year. Both 2013 and 2015 (Figs. 4.15 & 4.17) were wetter years than 2012 and 2014 (Fig. 3.3). This resulted in maximum ET rates during June of 0.23 mm $30min^{-1}$. Therefore, dry months can result in ET rates near 70% lower than normal.

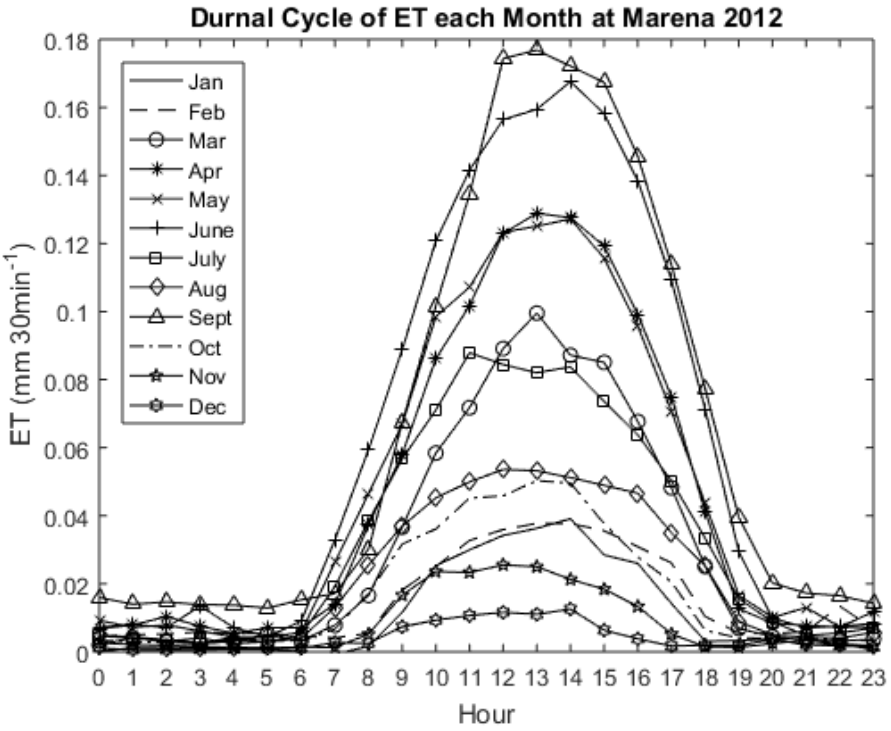

Figure 4.14: Diurnal pattern of ET values each month of the dataset at Marena 2012.

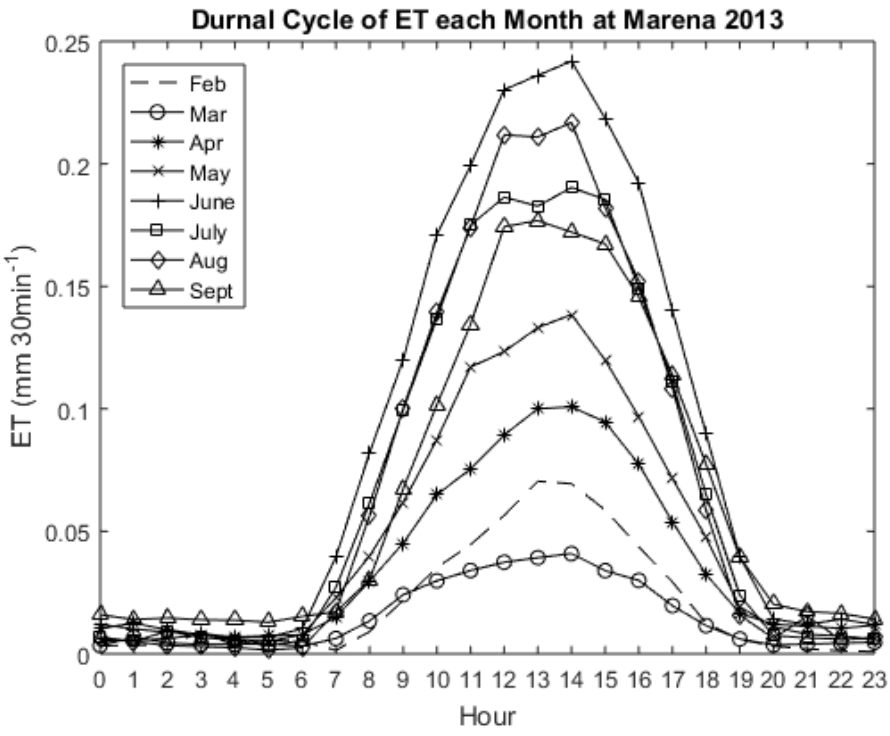

Figure 4.15: Diurnal pattern of ET values each month of the dataset at Marena 2013.

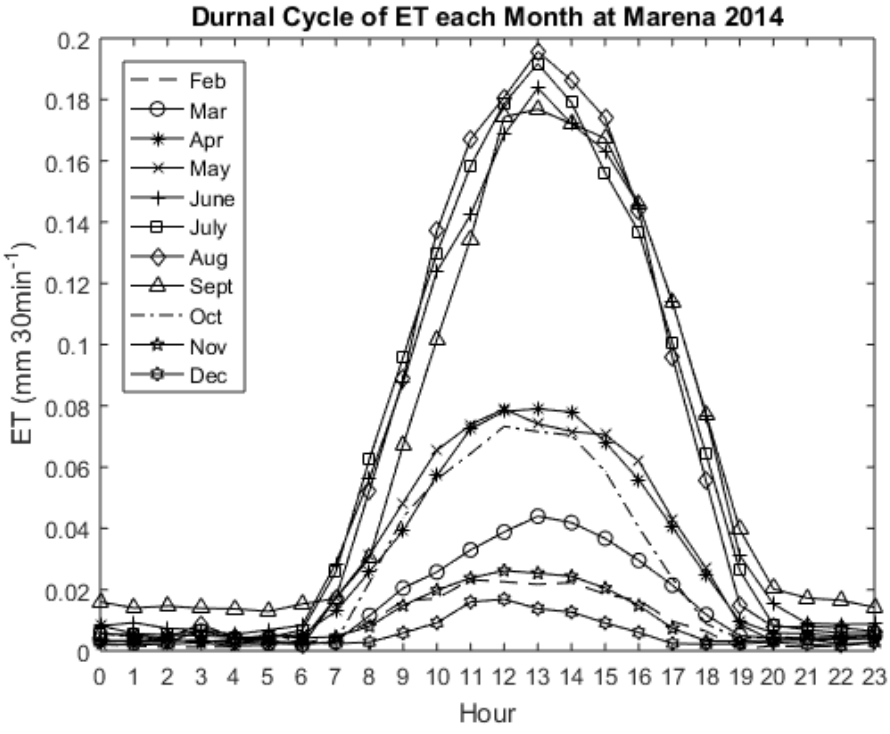

Figure 4.16: Diurnal pattern of ET values each month of the dataset at Marena 2014.

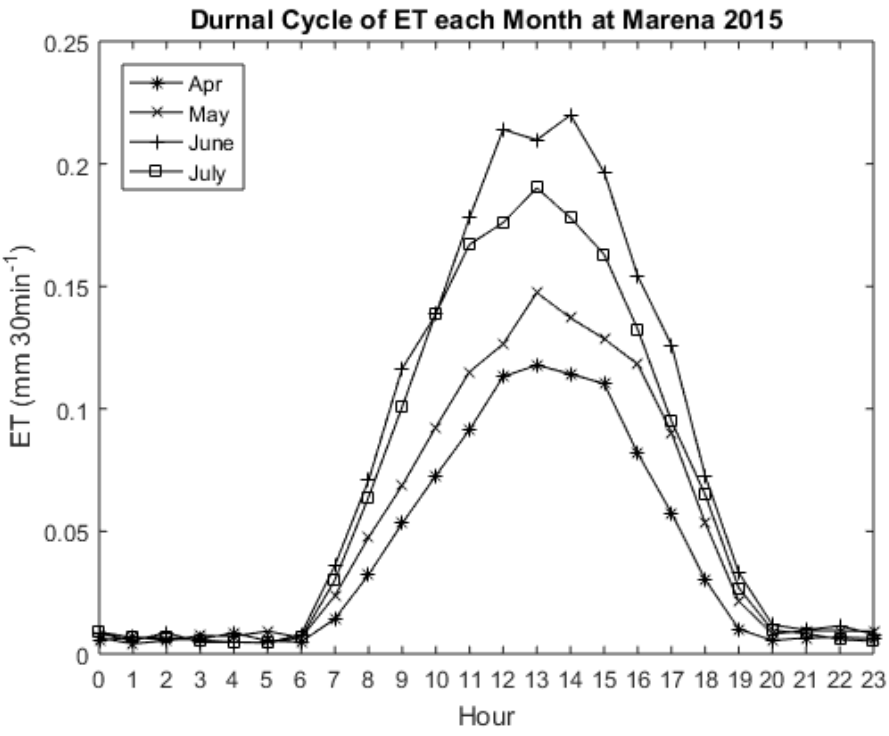

Figure 4.17: Diurnal pattern of ET values each month of the dataset at Marena 2015.

4.1.4 Seasonal Patterns of Evapotranspiration and Carbon Exchange

Time series of ET and GPP highlight how the water and carbon fluxes vary throughout the year (Figs. 4.18-4.26). When examining ET it is important to consider GPP because both are functions of vegetation health and maturity. Overall, the ET and GPP correlate well with each other over these sites (R^2 = .63).

The Maximum daily ET values ranged between 3.5 mm day^{-1} at ICOS (Fig. 4.18) to 7 mm day^{-1} at IGOS East (Figs. 4.19 & 4.20) while the maximum GPP values range from 20 gC m^{-2} day^{-1} at Marena 2012 to 70 gC m^{-2} day^{-1} at IGOS East 2014 and IGOS West 2015 (Fig. 4.22). In addition, the summer months typically had the highest ET and GPP for the grassland sites when vegetation was healthy.

ICOS has an earlier peak of ET and GPP in April due to the earlier growing season. This results in a lower magnitude of ET and GPP compared to the other sites because of the reduced radiation budget in the Spring. ET values began to increase in March and decreased in late May when the wheat began to senesce. Once the crop was harvested in June the ET values fell to around 1 mm day^{-1}. These remaining ET values were likely due to soil evaporation alone. An increase in ET seen in July occurred when post-harvest native grasses emerged. Then, shortly there after, tilling created another decrease in ET followed by another increase in ET before the dormant season.

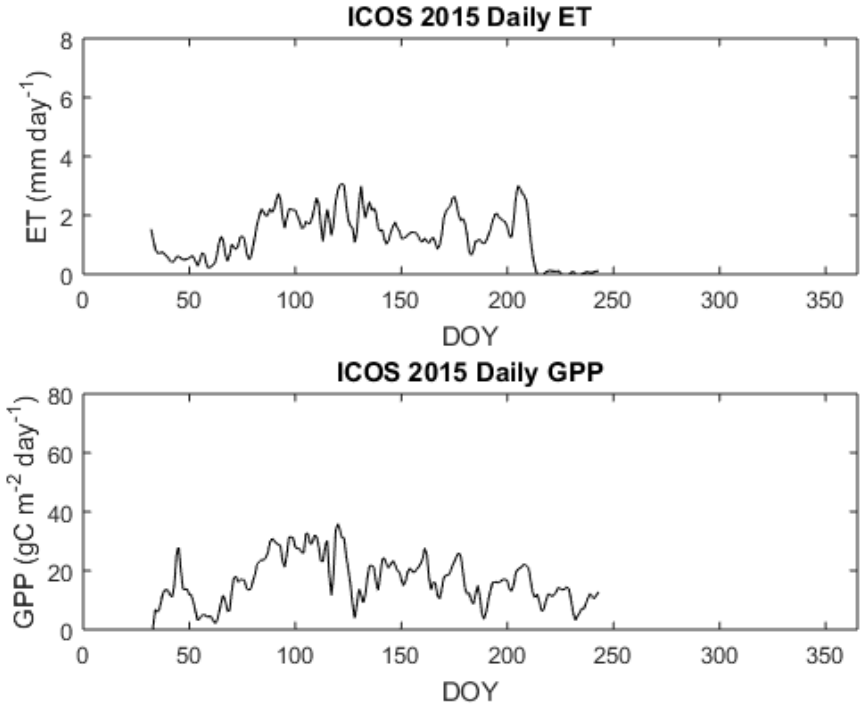

Figure 4.18: Time series of daily ET and GPP at ICOS 2015.

IGOS East 2014 (Fig. 4.19) ET increased to 7 mm day^{-1} as a result of heavy rain during June. In July, ET began to decrease and GPP dramatically decreased. This was

likely the result of grazing that occurred in this field for a brief period of time. Once the cattle were released from the field, the GPP rapidly increased and ET became more constant. The same decrease in ET and GPP can be seen at IGOS West 2014 (Fig. 4.21) when values decreased from 3.5 mm day^{-1} to below 1 mm day^{-1} and GPP values decreased from 40 gC m^{-2} day^{-1} to 20 gC m^{-2} day^{-1}. During April 2014, IGOS West was burned. The decrease in ET soon thereafter was a result of this and ET values never reached the magnitude of IGOS East during 2014. However, IGOS West during 2015 had ET values near 6 mm day^{-1} during the growing season.

Both IGOS East and West were more continuous and constant in ET and GPP (Fig. 4.20 & 4.22) during 2015. Maximum values of ET (6.5 mm day^{-1}) and GPP (45 gC m^{-2} day^{-1}) occurred in June and July at IGOS East 2015 (Fig. 4.20). Further, IGOS West 2015 had lower ET (5.5 mm day^{-1}) but higher GPP (60 gC m^{-2} day^{-1}). This may be a result of the canopy at IGOS West being shorter than the canopy at IGOS East.

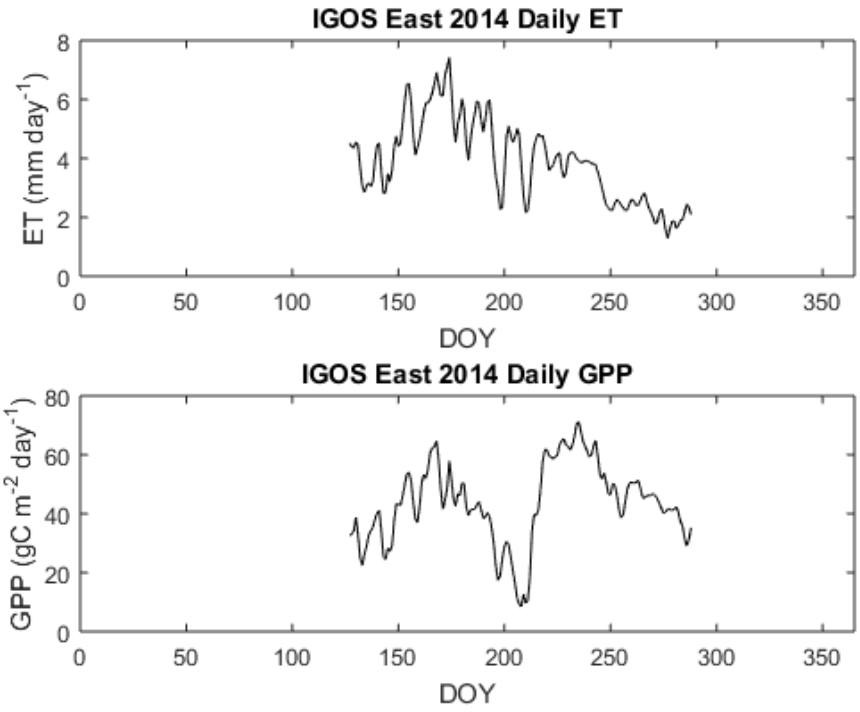

Figure 4.19: Time series of daily ET and GPP at IGOS East 2014.

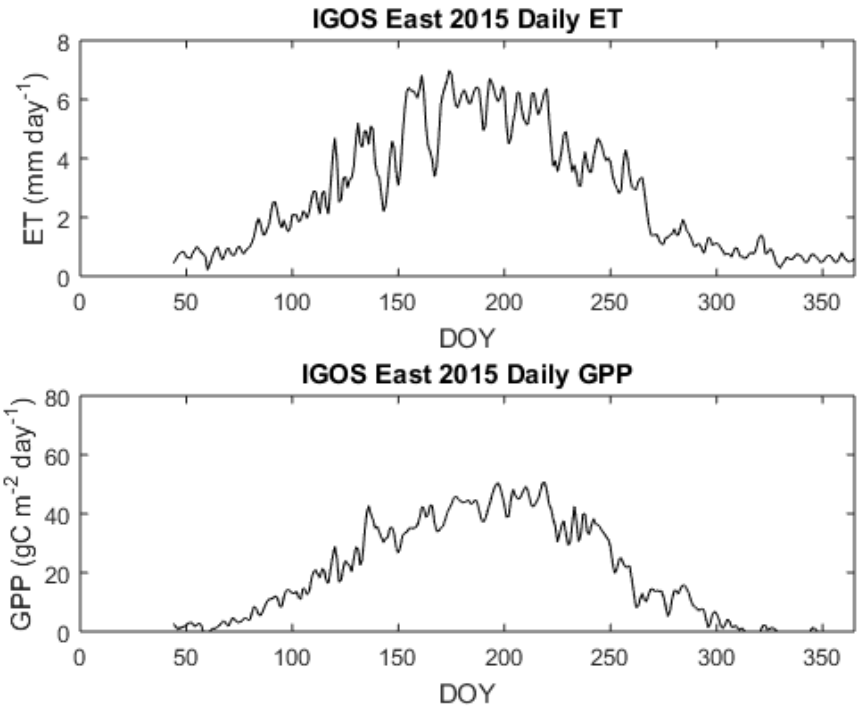

Figure 4.20: Time series of daily ET and GPP at IGOS East 2015.

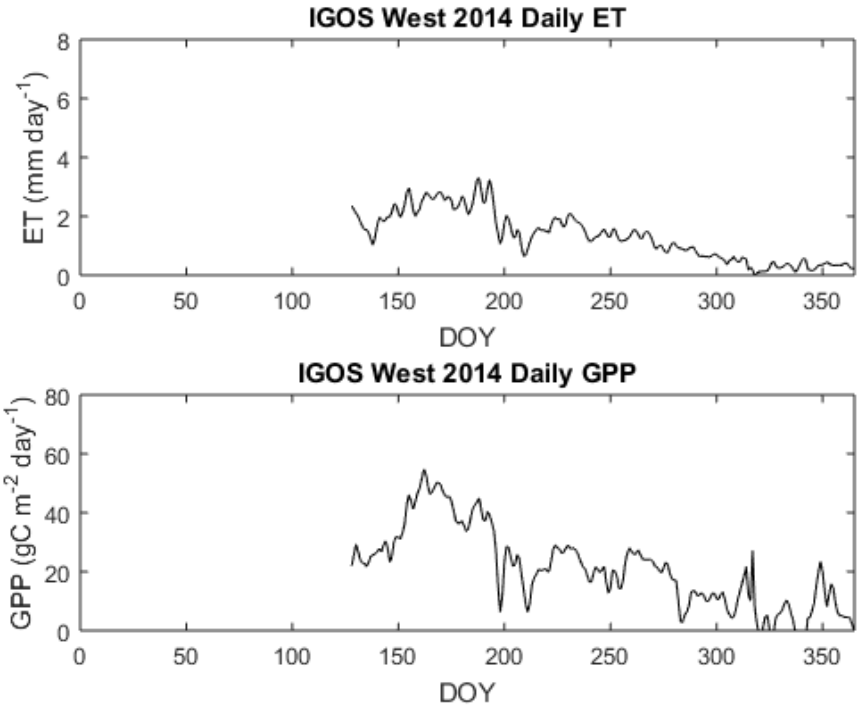

Figure 4.21: Time series of daily ET and GPP at IGOS West 2014.

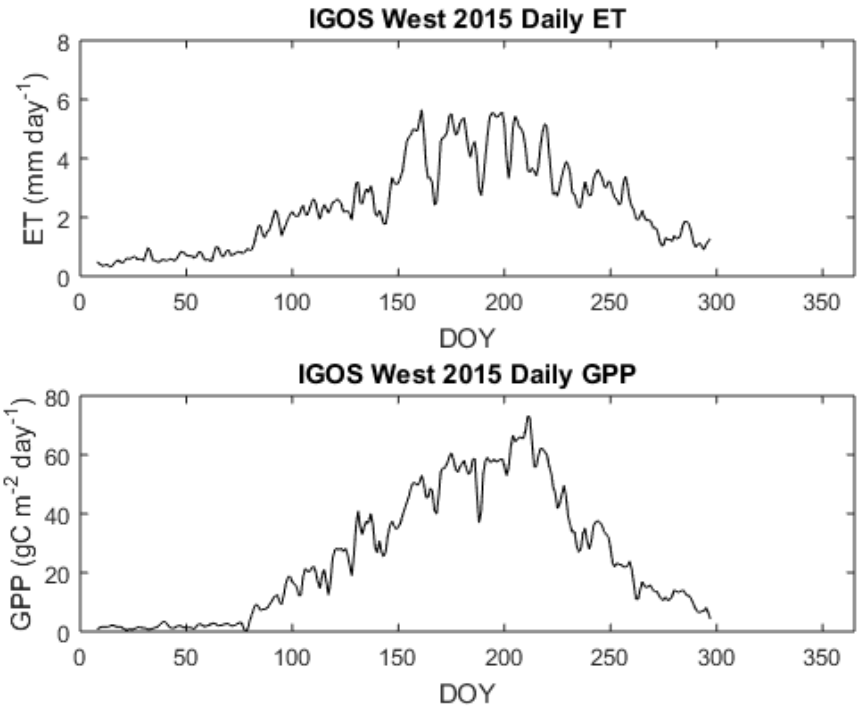

Figure 4.22: Time series of daily ET and GPP at IGOS West 2015.

Marena maximum ET was higher in 2013 (5 mm day^{-1}) and 2015 (5 mm day^{-1}) than 2012 (3.5 mm day^{-1}) and 2014 (4 mm day^{-1}) (Figs. 4.23-4.26). As mentioned previously, 2012 and 2014 were drier than 2013 and 2015. The GPP values of 2012 never rose above 20 gC m^{-2} day^{-1} indicating that the ecosystem was never fully mature (Fig. 4.23) and quickly fell in early July in response to the onset of flash drought. In 2014 the GPP and ET increased in June after copious amounts of rainfall (Fig. 4.25). The greatest correlation between ET and GPP (Fig. 4.26) at Marena occurred during 2015 whereby ET and GPP follow the same increasing and decreasing patterns and show nearly the same change in magnitude.

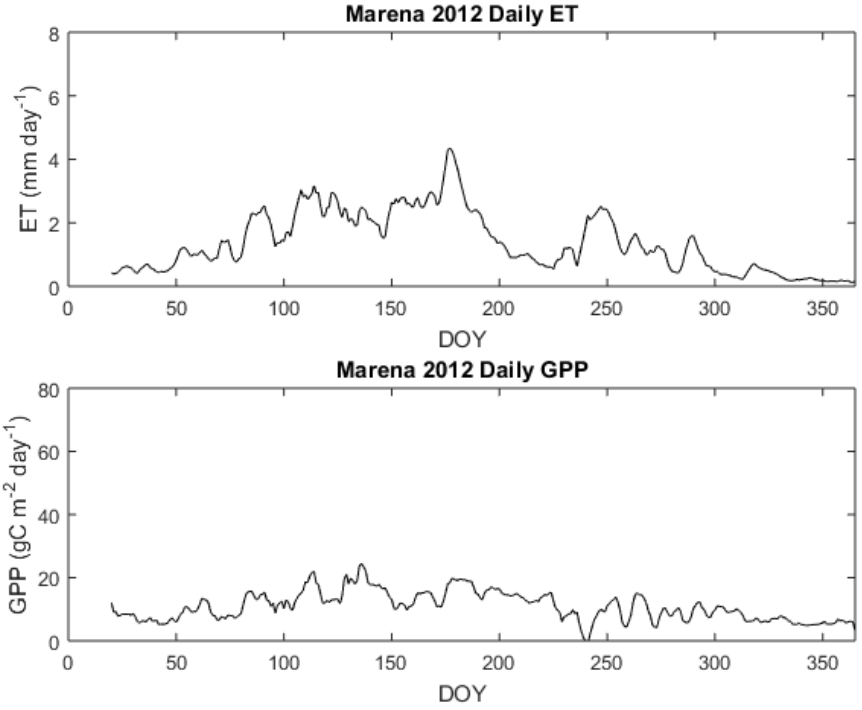

Figure 4.23: Time series of daily ET and GPP at Marena 2012.

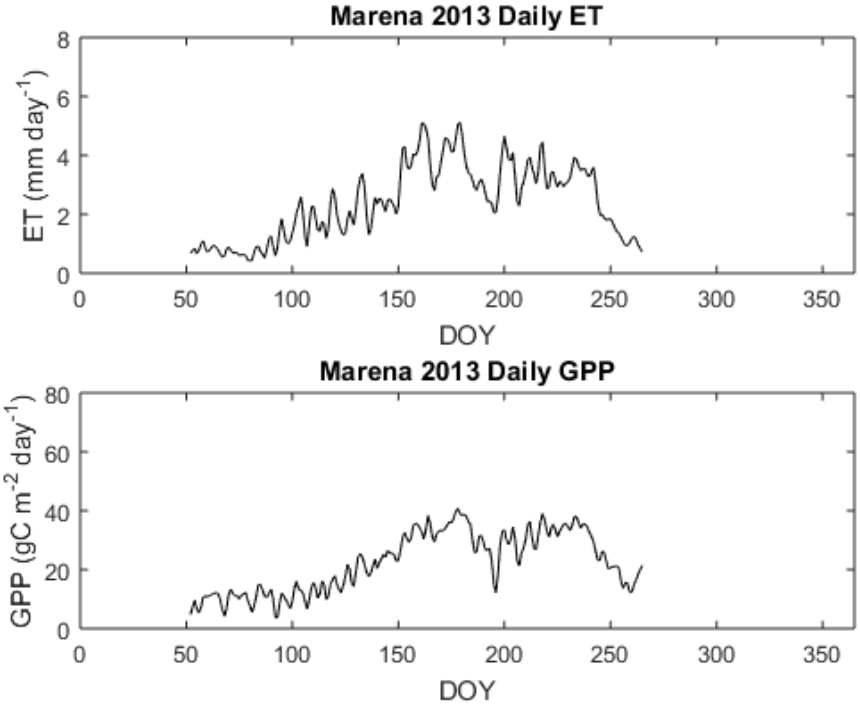

Figure 4.24: Time series of daily ET and GPP at Marena 2013.

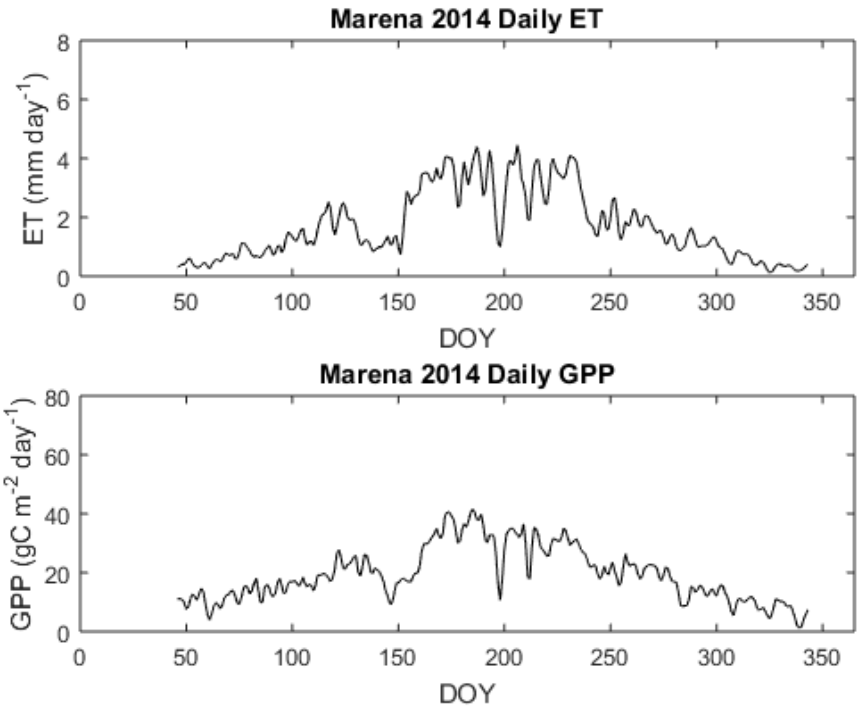

Figure 4.25: Time series of daily ET and GPP at Marena 2015.

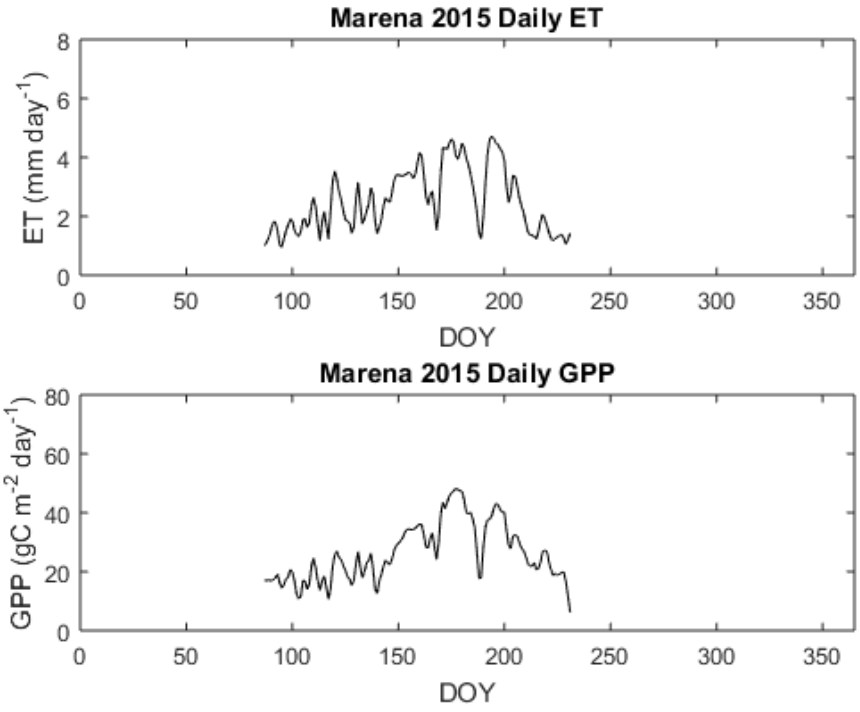

Figure 4.26: Time series of daily ET and GPP at Marena 2015.

Chapter 5 : Model Output and Analysis of Three Land Surface Models

5.1 TSEB Results

TSEBS domain was central Oklahoma in Gowda et al. (2016). The stations that lie within this domain are Marena, ARM SGP Main, ARM SGP Control, ARM SGP Control, and IGOS West/East. Landsat 8 was used to force TSEBS and create daily values of estimated ET. Figure 5.1 compares TSEBS modeled ET with the flux tower observed ET and shows a heteroscedastic relationship between the two. Overall, the correlation is $R^2 = 0.37$ and an RMSE of 1.3 mm/day that is 60% of the daily average ET.

Results of Figure 2.2a and 2.2b were recreated from the same dataset and show that the R^2 values were ~0.7 as reported in Gowda et al. (2016). However, when the same sites were analyzed for the next year (2006), which were not reported in the Gowda et al. (2016) study, results show that the correlation is much less ($R^2 \sim 0.35$). As such, the correlations can fluctuate rather significantly from one year to the next. At the ARM SGP Main sites the R^2 values ranged from 0.03 in 2005 to 0.6 in 2003, 2007, 2010, and 2014. Thus, while TSEBS performs well for some years and some sites, more investigation is needed to determine whether or not TSEBS should be applied across the SGP.

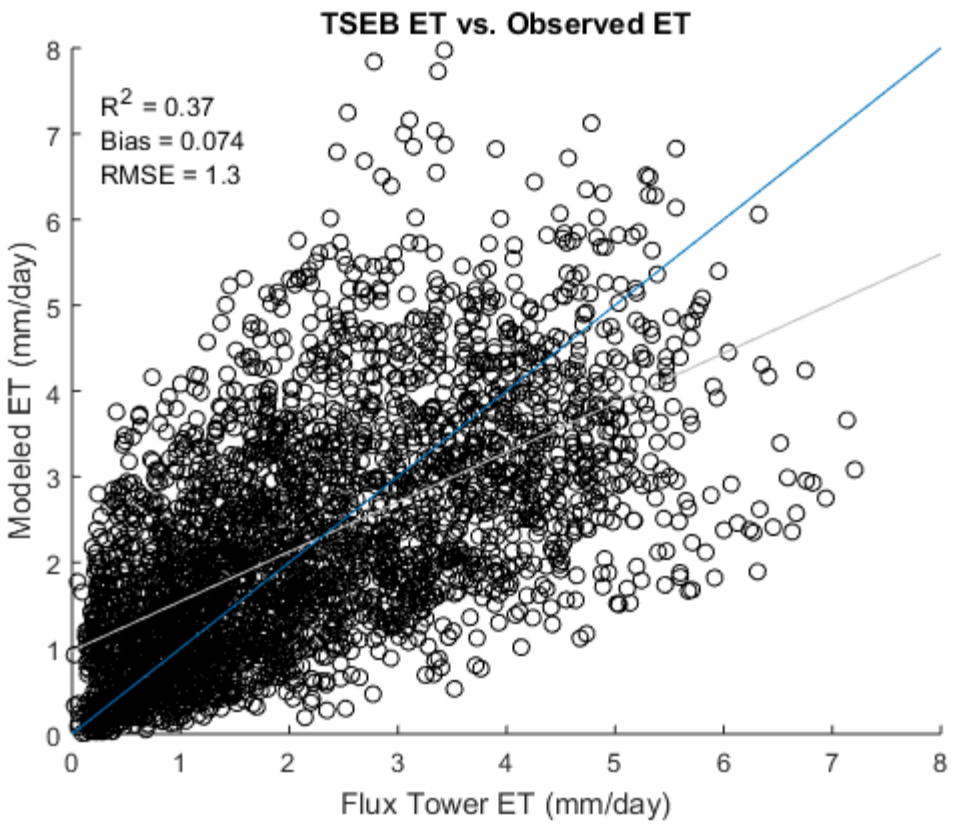

Figure 5.1: TSEBS modeled ET compared to observed flux tower ET at Marena, ARM SGP Main, ARM Control, ARM Burn, and IGOS West/East 2014 where the blue line is a 1:1 reference line and the grey line is the linear best-fit line.

5.2 Wagle Model Results

For comparison, the Wagle model was examined for the same sites and years as TSEBS (Fig. 5.2). The Wagle model was only evaluated every 8 days because of the MODIS-derived PAR and EVI being limited to every MODIS retrieval period of once every 8 days. Interpolation schemes that were used for TSEBS and BESS were not used for the Wagle model because interpolation schemes have not been developed for the Wagle model. As such, a significantly lower sample size existed and the correlation is slightly lower than TSEBS (R^2 = 0.33) with a lower bias and similar RMSE.

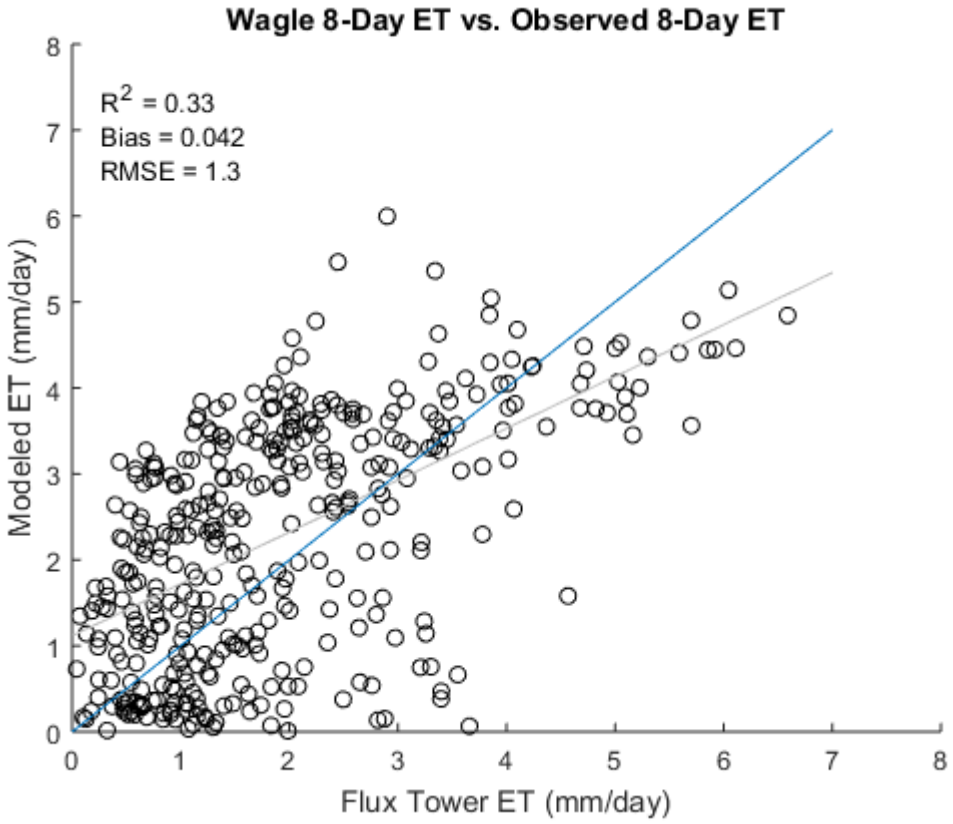

Figure 5.2: Wagle modeled 8-Day ET compared to observed flux tower ET at Marena, ARM SGP Main, ARM Control, ARM Burn, and IGOS West/East 2014 where the blue line is a 1:1 reference line and the grey line is the linear best-fit line.

In addition to the direct comparison to TSEBS, the Wagle model was also evaluated over all the grassland sites in the SGP. Because the Wagle model was created with a training dataset from only grassland data the winter wheat sites were not used in the verification (Fig. 5.3). The Wagle model does not produce a linear correlation between modeled and observed ET. Instead, the relationship appears logarithmic. As such, when a linear fit to the plot was applied the $R^2 = 0.59$, but when a logarithmic fit was applied the $R^2 = 0.66$. Further, the RMSE was 30% of the total average daily ET. A strong linear relationship ($R^2 = 0.89$) was found when Wagle et al. (2016) verified the

model with a testing dataset, but Wagle et al. (2016) used in-situ PAR data for their verification instead of remotely sensed PAR data. The purpose of the Wagle model was to create an empirical model that uses MODIS data in estimating ET over grassland regions. However, that study did not use MODIS-derived PAR in the testing and training dataset. The results shown in Figure 5.1 and 5.2 were forced with MODIS EVI and MODIS-derived PAR.

Comparisons of MODIS-derived PAR and in-situ measured PAR from the grassland sites reveal that MODIS-derived PAR overestimates in-situ PAR at the SGP sites. Because the empirical model was created with a dataset that consisted of MODIS EVI and in-situ measured PAR, it is not surprising that the model does not perform as well when using MODIS-derived PAR. Further, a linear correction term added to the PAR data would not solve the problem because the difference between MODIS-derived PAR and in-situ PAR differs from year-to-year and site-to-site.

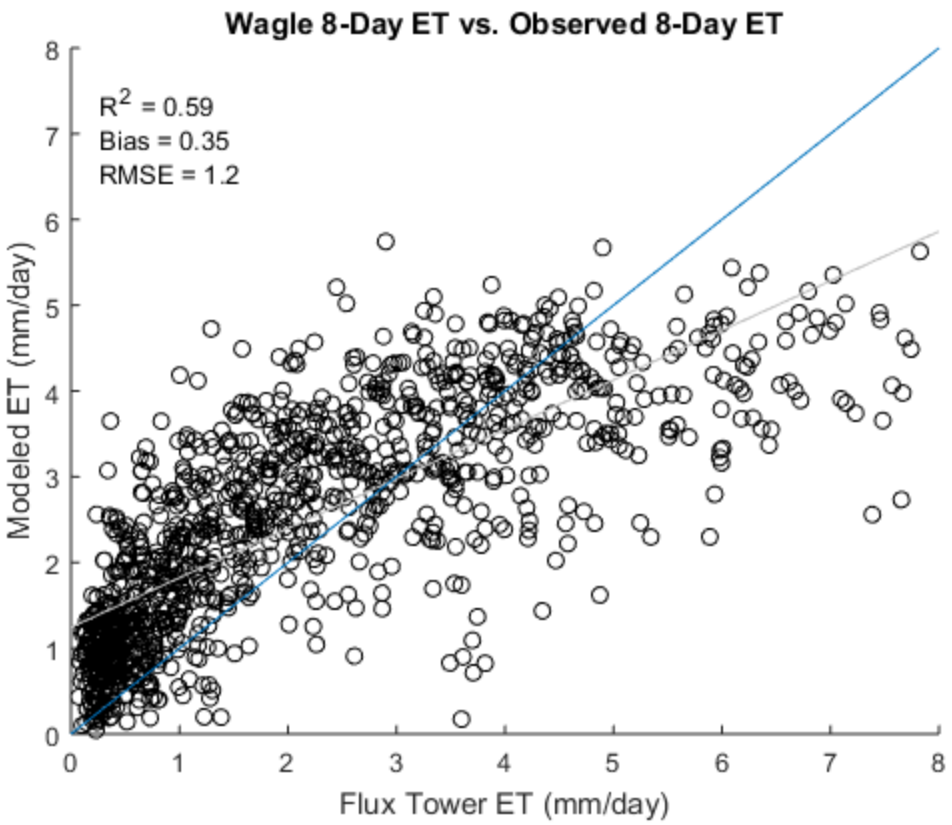

Figure 5.3: Wagle modeled 8-day ET compared to observed flux tower ET at all grassland SGP towers where the blue line is a 1:1 reference line and the grey line is the linear best-fit line.

5.3 BESS Results

BESS was initialized over the domain of the SGP (Fig. 1.1) and compared with 16 flux towers (Table 3.1) for 60 total years of data. BESS was upscaled from instantaneous ET to 8-day average ET, but can also be scaled to using the method developed by Ryu et al. (2012).

Similar to Figure 5.1 and 5.2, BESS was also analyzed for the same sites as TSEBS for direct comparison (Fig. 5.4). The correlation for BESS is slightly better than the Wagle model and TSEBS ($R^2 = 0.41$). The bias was the same as for the Wagle model but lower than TSEBS, and the RMSE of 1.1 mm was also lower than both

Wagle (1.2 mm) and TSEBS (1.3 mm). The BESS results were also more homoscedastic than TSEBS, and as such, an increase in ET values would not lead to a growth in estimation error.

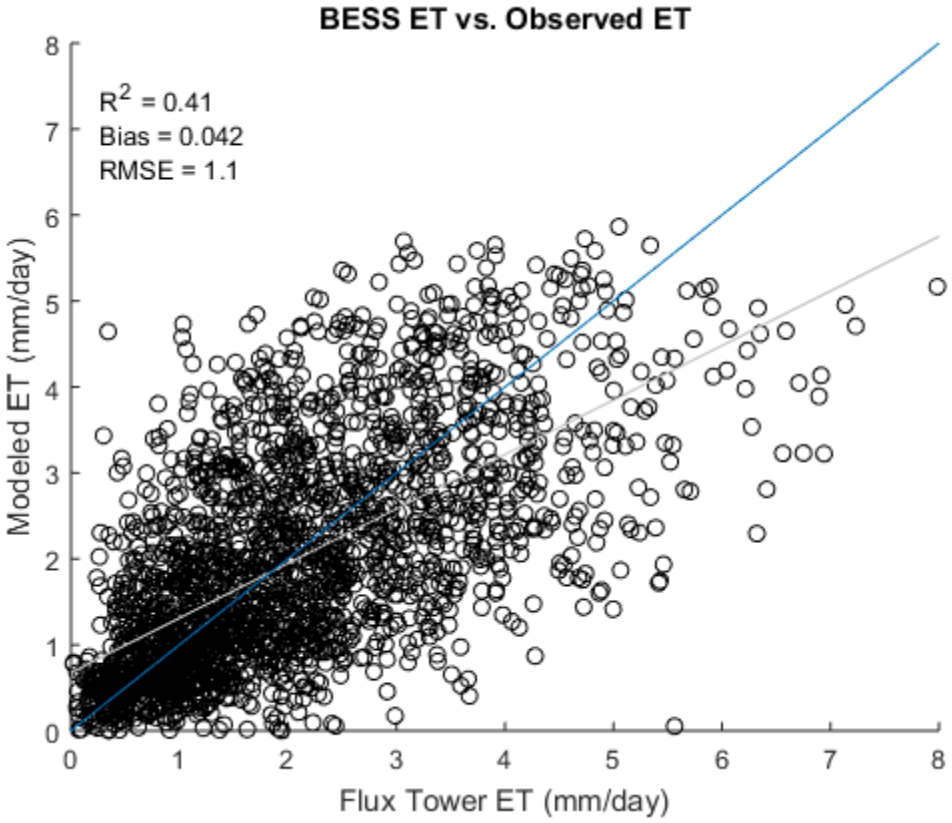

Figure 5.4: BESS modeled ET compared to observed flux tower ET at Marena, ARM SGP Main, ARM Control, ARM Burn, and IGOS West/East 2014 where the blue line is a 1:1 reference line and the grey line is the linear best-fit line.

BESS was also compared to the MODIS-derived ET (Fig. 5.5). The 8-day ET is better estimated by BESS (R^2 = 0.74) than by MODIS (R^2 = 0.60) over the SGP. BESS had a slightly larger bias, but the RMSE was 0.79 mm/day compared to 1.1 mm/day for MODIS. Overall, for the SGP, BESS performed better than TSEBS, the Wagle model, and MODIS-derived ET.

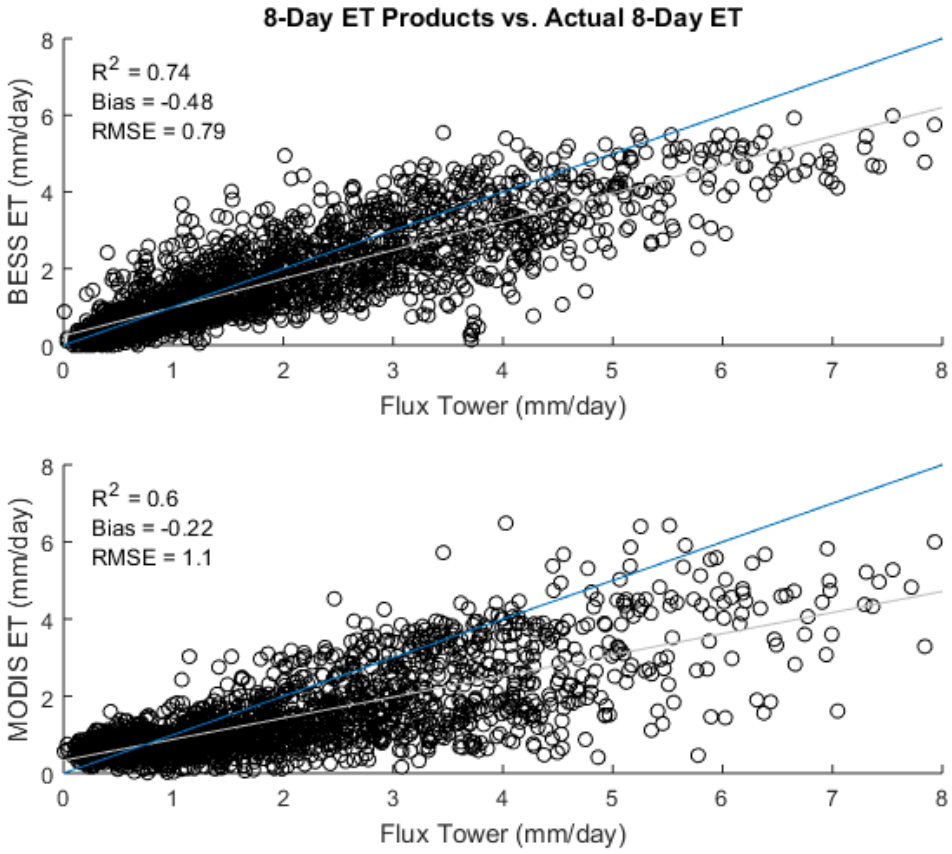

Figure 5.5: BESS modeled 8-day ET compared to observed flux tower ET at all SGP towers where the blue line is a 1:1 reference line and the grey line is the linear best-fit line.

A closer examination was conducted for grassland and winter wheat sites, individually (Fig. 5.6). Separating the data between grassland and cropland sites demonstrated that BESS is able to estimate ET better over the grassland regions (R^2 = 0.76) than winter wheat (R^2 = 0.54). The RMSE for winter wheat was 47% of the daily average ET observed and grasslands have an RMSE of 42% of the daily average ET observed. The bias was coincidentally the same for the two vegetation types, but it was a very small underestimation (-0.079 mm) of the observed ET.

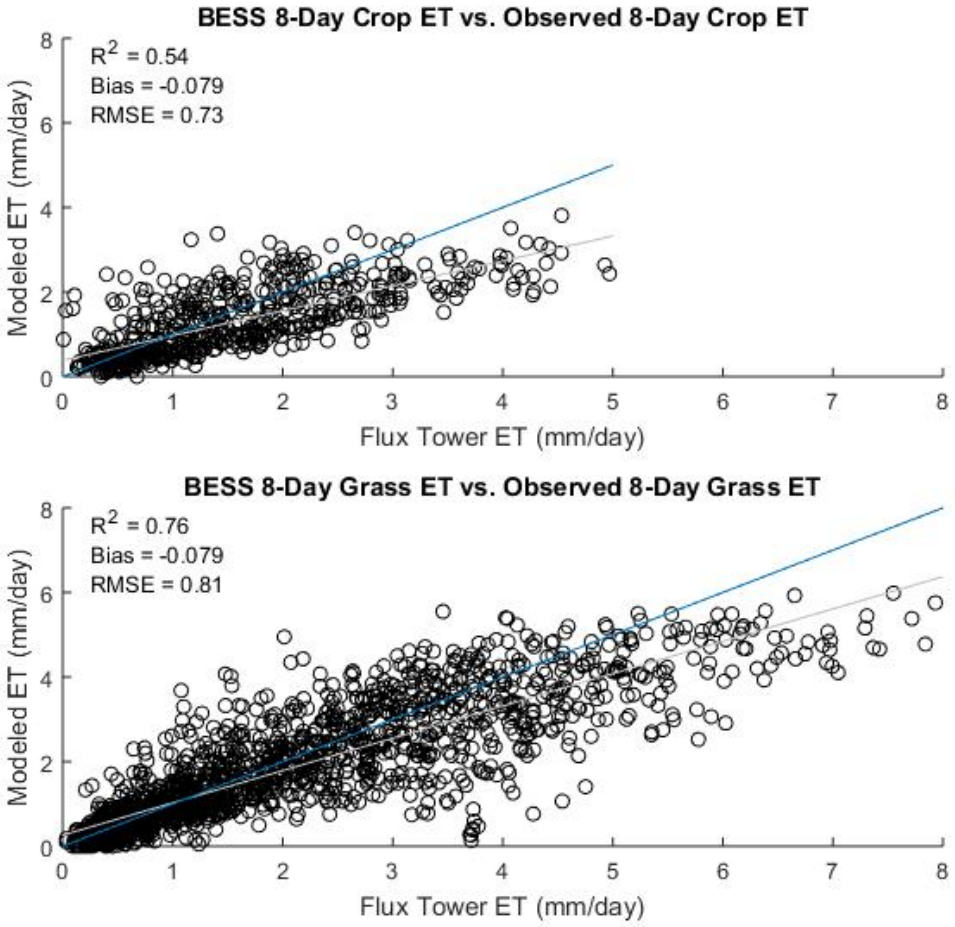

Figure 5.6: BESS modeled 8-day ET compared to observed flux tower ET at all grassland and cropland SGP towers separately where the blue line is a 1:1 reference line and the grey line is the linear best-fit line.

BESS daily ET compared to observed-daily ET was less accurate than the 8-day ET estimation for all the sites in the SGP (Fig. 5.7). The $R^2 = 0.61$ and the RMSE was 1.1 mm, which was 56% of the daily average observed ET. The separation of daily ET into grassland and winter wheat sites yielded the same discrepancy (Fig. 5.8 and 5.9). At the same time, the daily estimations of ET are expected to be less accurate than 8-day mean daily sums of ET given the interpolation scheme from MODIS snapshot to daily sums performs better when averaging over an 8-day period as it is likely to

remove random variability in the diurnal variation of ET due to cloud cover or rapid changes in soil moisture (Ryu et al. 2012).

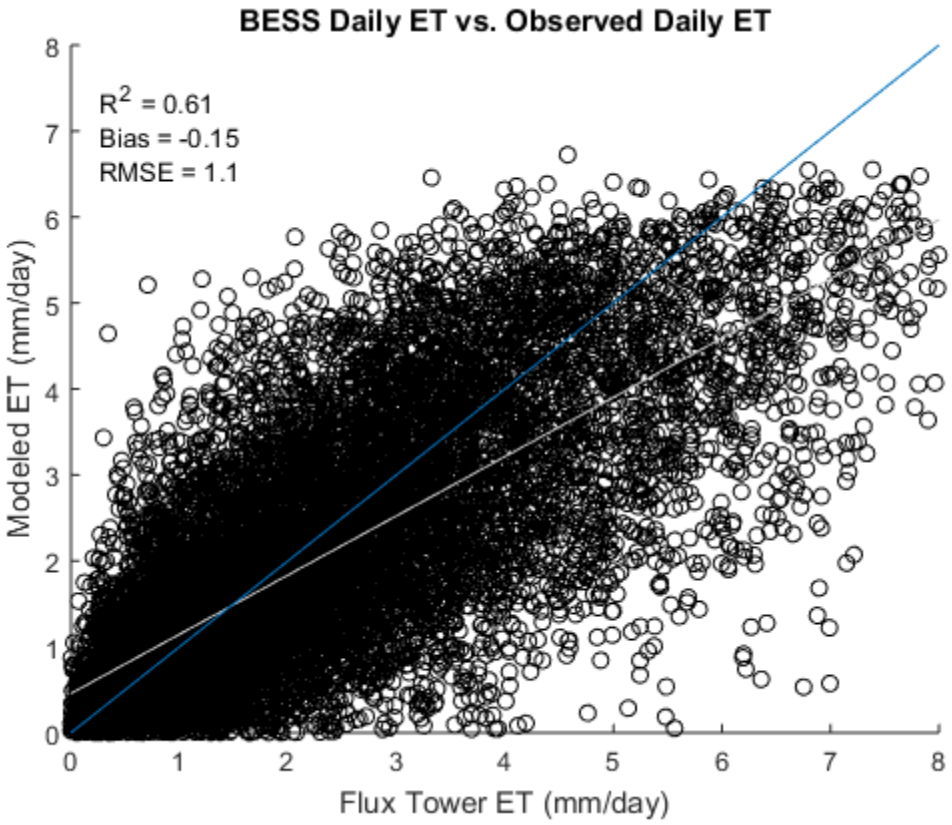

Figure 5.7: BESS modeled daily ET compared to observed flux tower ET at all SGP towers where the blue line is a 1:1 reference line and the grey line is the linear best-fit line.

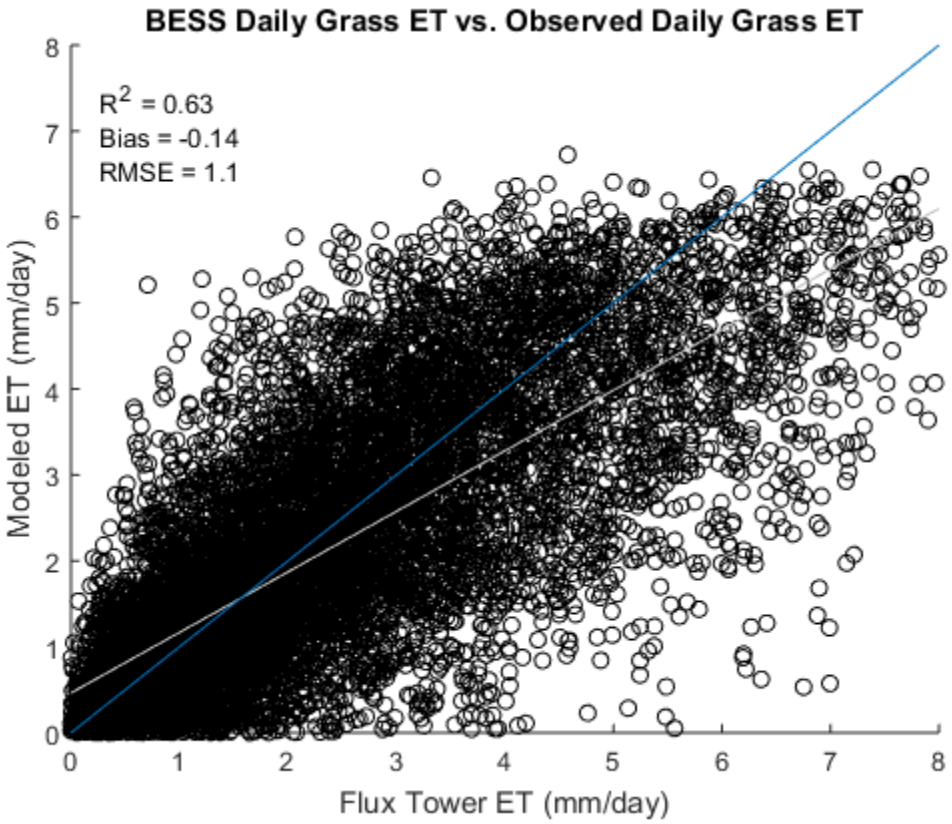

Figure 5.8: BESS modeled daily ET for compared to observed flux tower ET for at all SGP grassland towers where the blue line is a 1:1 reference line and the grey line is the linear best-fit line.

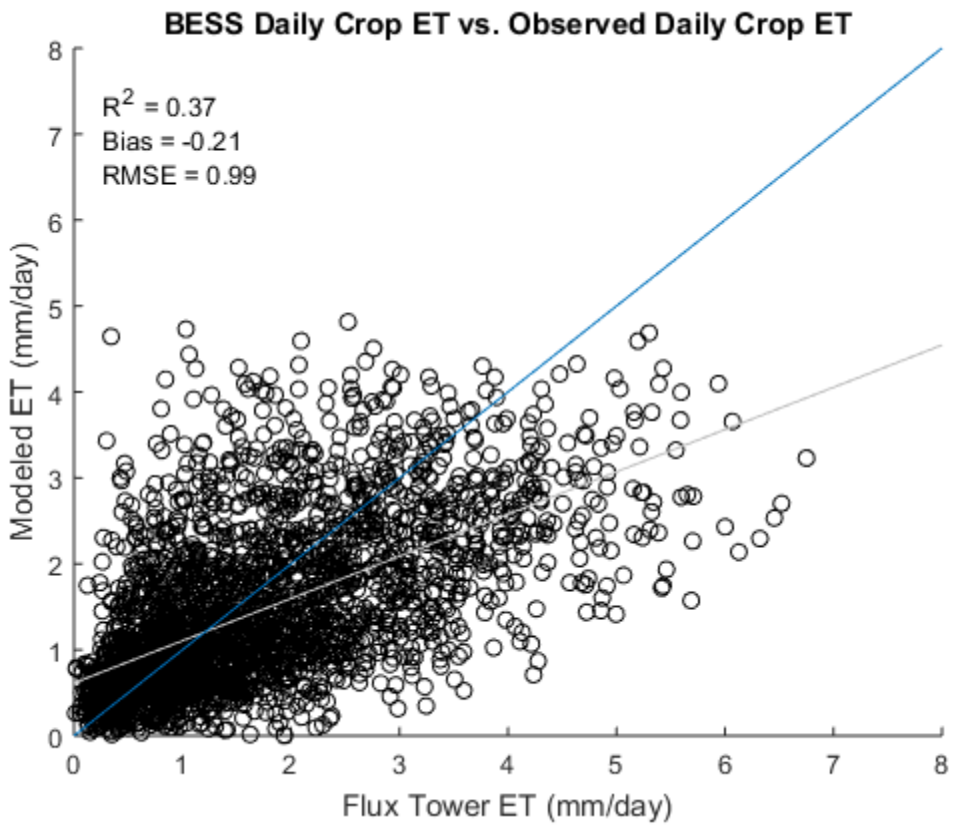

Figure 5.9: BESS modeled daily ET compared to observed flux tower ET at all SGP cropland towers where the blue line is a 1:1 reference line and the grey line is the linear best-fit line.

The time series of BESS estimated daily ET matches well to the observed daily ET at most sites (Appendix C). For example, the Kansas Field Station was represented accurately by BESS from 2008-2012 (Fig. 5.10). There were instances where BESS overestimated ET (e.g., 2010 BESS overestimated ET by a couple of millimeters around day 180, in 2011 BESS overestimated ET for a period between DOY 150 and 200, and in 2012 BESS overestimated ET during drought conditions around DOY 200). However, the variability of ET was well captured by BESS at the Kansas Field Station. Spikes in ET near DOY 190 in 2010 and DOY 250 in 2011 were also detected by BESS.

A few sites were not as well represented by BESS. The Kansas Land Institute station from 2012-2014 differs significantly between BESS and observations (Fig. 5.11). This site had some of the largest differences between BESS and observations of all the sites analyzed. In 2012 the variability of observed ET was not apparent in BESS. Several instances show spikes in ET that were not detected by BESS; BESS appears to estimate the average ET and does not appear to have an overall bias. During 2013 the same issue occurs where BESS is not able to represent the high ET rates observed at DOY 160 and DOY 275 and in 2014, in the high observed ET rates were not simulated by BESS at DOY 100 and DOY 160-190. However, overall BESS was able to represent the general variability and magnitude of ET at most sites.

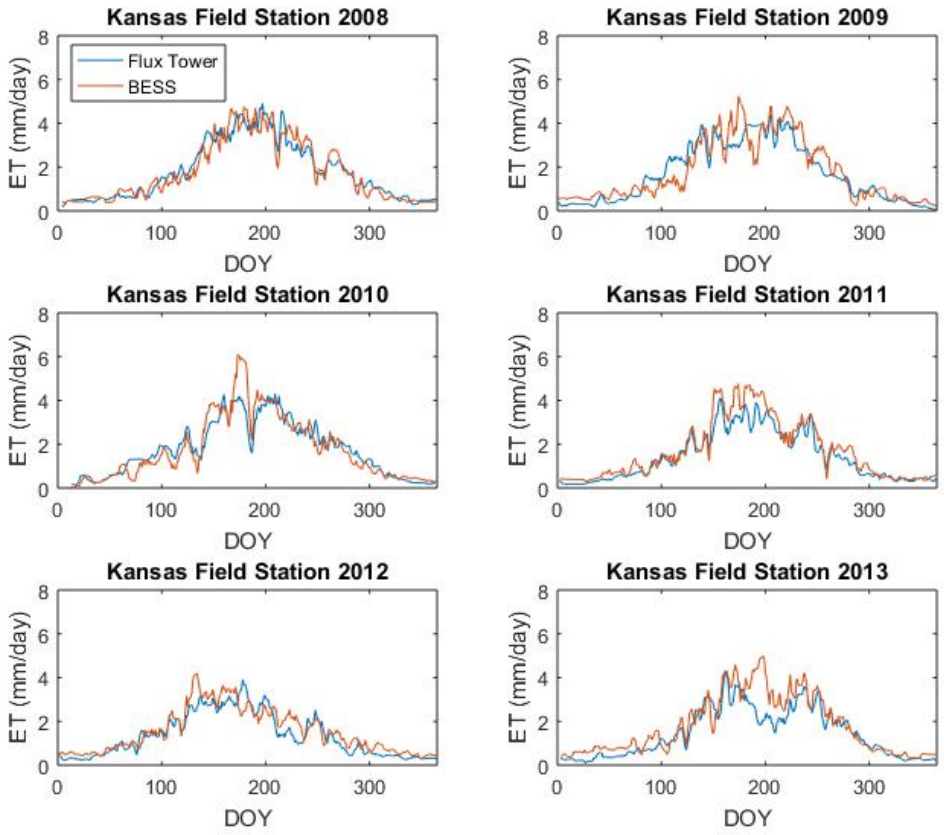

Figure 5.10: Time series of daily ET from BESS and observed ET at the Kansas Field Station.

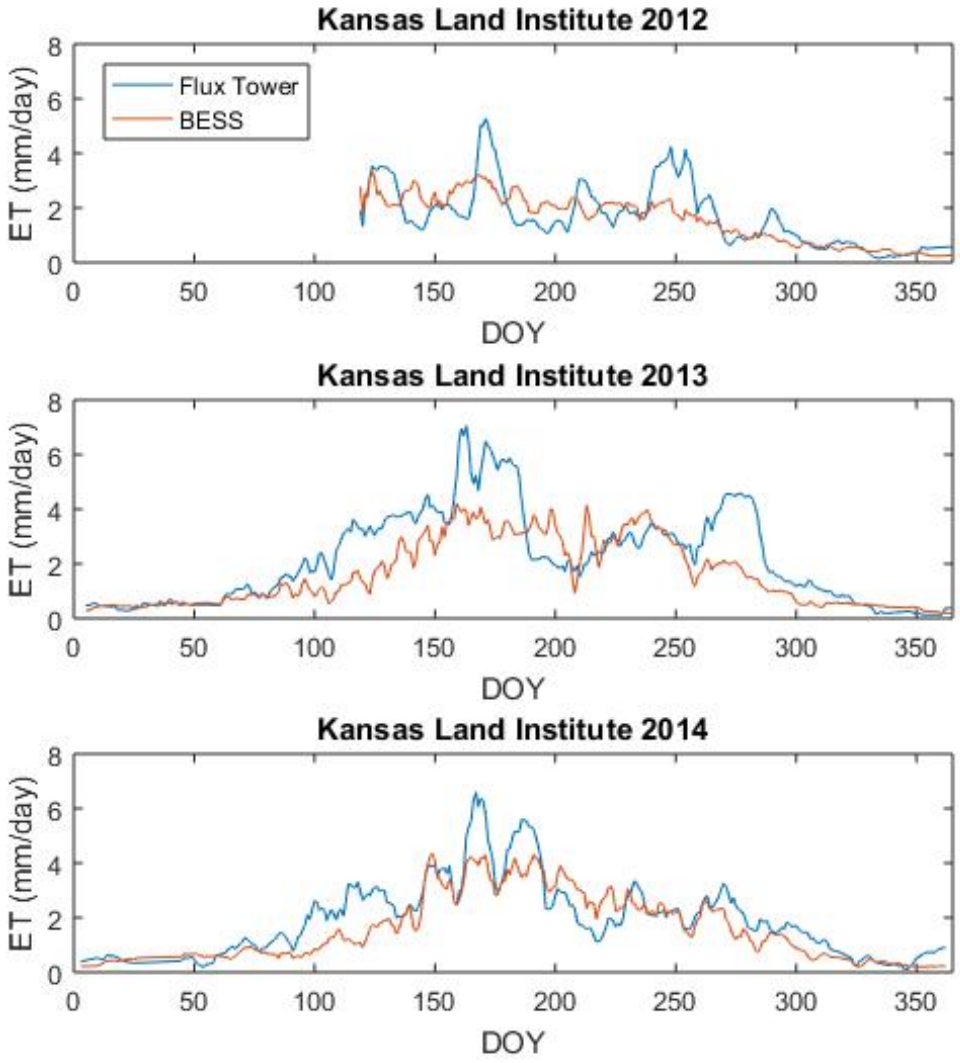

Figure 5.11: Time series of daily ET from BESS and observed ET at the Kansas Field Station.

5.3.1 Spatiotemporal Analysis

Average daily ET estimates for each month from BESS over the SGP from 2000 through 2015 reveal how ET varies throughout the year (Figs. 5.12-5.23). During January and February (Figs. 5.12-5.13) ET values were near 0 mm/day due to the dormant vegetation. In March (Fig. 5.14) ET increased in the southeast portion of the

domain as vegetation growth begins from southeast to northwest. In April higher ET values increase in the southeast to 3-3.5 mm/day and spread throughout a larger portion of the SGP (Fig. 5.15). An interesting feature that appears in April is the locally high values of ET ranging from 2.5-3 mm/day from central Kansas through western/southwestern Oklahoma (Oklahoma Climate Division 2). This feature is associated with the winter wheat belt that extends over the same area (McPherson and Stensrud, 2004) because peak growth of winter wheat occurs in April and early May. Despite previous results (Fig. 5.6) showing BESS does not represent winter wheat well at the three sites over the SGP, BESS is able to display the increased ET over the SGP due to winter wheat growth. By May the entire SGP ecosystem produced ET rates distinguishable by BESS (Fig. 5.16). Values ranged from 4.5 mm/day in the southeast SGP to near 2 mm/day in the northwest portion of the SGP. The winter wheat belt feature is still evident in May, however it is more faint due to the growth of native grasses and warm season crops with and adjacent to the winter wheat belt. By June the eastern portion of the SGP has ET values of ~5 mm/day, much of which is forested regions (Fig. 5.17). The local maxima in ET from the winter wheat crop is now a minima in ET for June because of senescence and harvest that occurs in early-to-mid June. At the same time, the peak in ET rates over the eastern portion of the SGP occurs in June with average daily ET exceeding 5 mm/day. In July other crop features are illuminated by BESS in the Texas/Oklahoma panhandles and western Kansas that exceed 4 mm/day (Fig. 5.18). The maximum ET rates in the western half of the SGP occur during July, aside from the winter wheat belt. The ET rates decrease across the entire SGP during August (Fig. 5.19) and the winter wheat belt is again a point of

interest because of the locally low values of ET due to tilling practices in preparation for winter wheat to be planted at the beginning of September. During September ET rates decrease across the northwest SGP below 2 mm/day while the southeast is between 3-4 mm/day (Fig. 5.20). A dramatic decrease in ET occurs between September and October as native grasses and vegetation senesce (Fig. 5.21). Similar to January and February, November and December have average ET rates near 0 mm/day (Figs. 5.22-5.23).

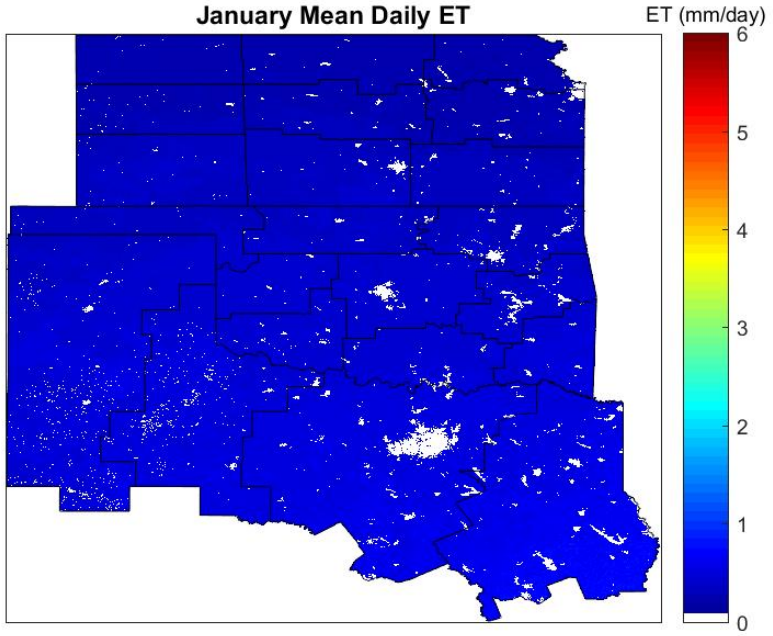

Figure 5.12: Average daily ET estimates from BESS during January from 2000-2015 over the SGP with climate division contoured.

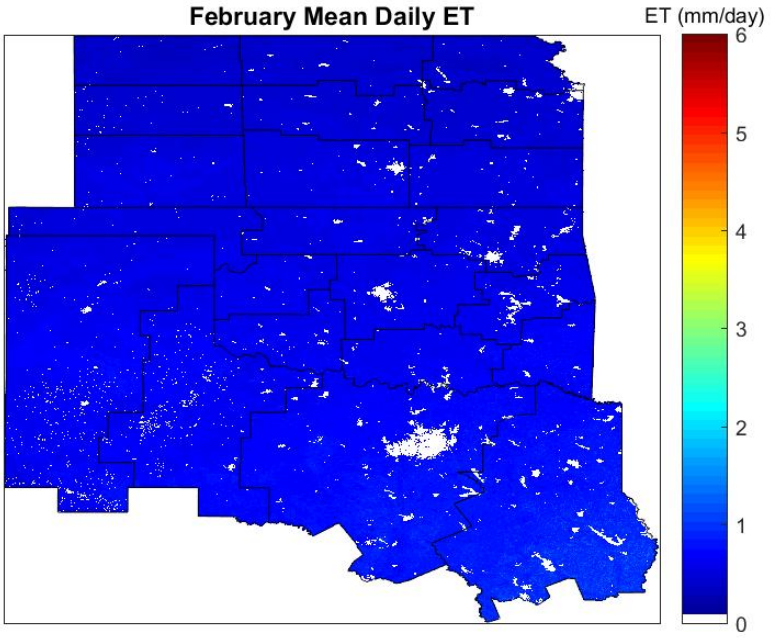

Figure 5.13: Average daily ET estimates from BESS during February from 2000-2015.

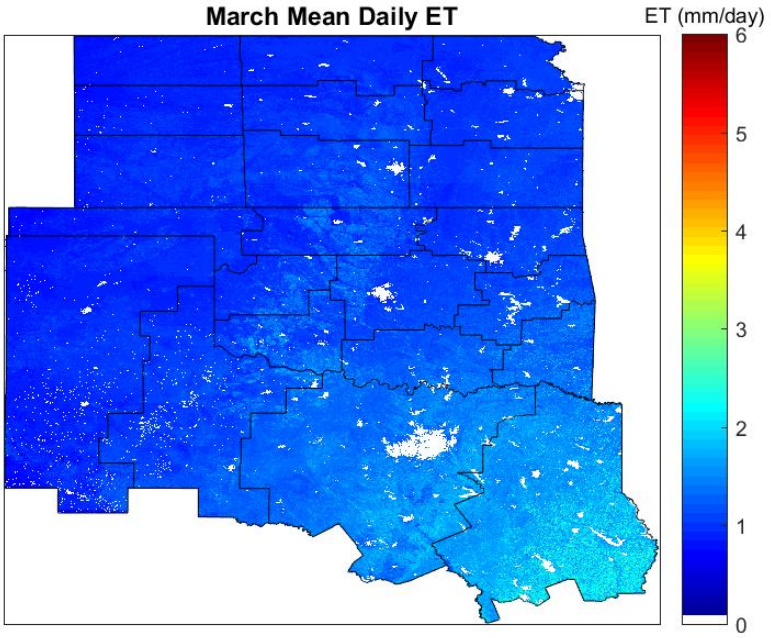

Figure 5.14: Average daily ET estimates from BESS during March from 2000-2015.

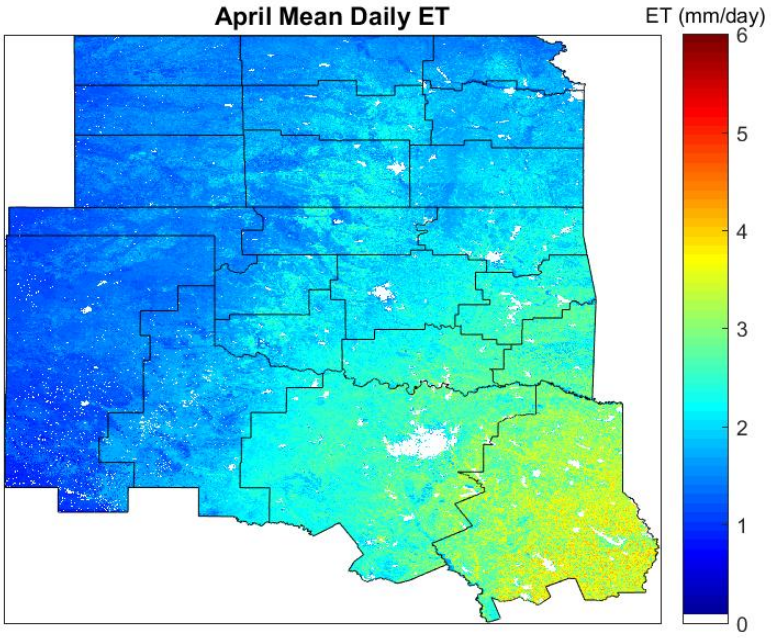

Figure 5.15: Average daily ET estimates from BESS during April from 2000-2015.

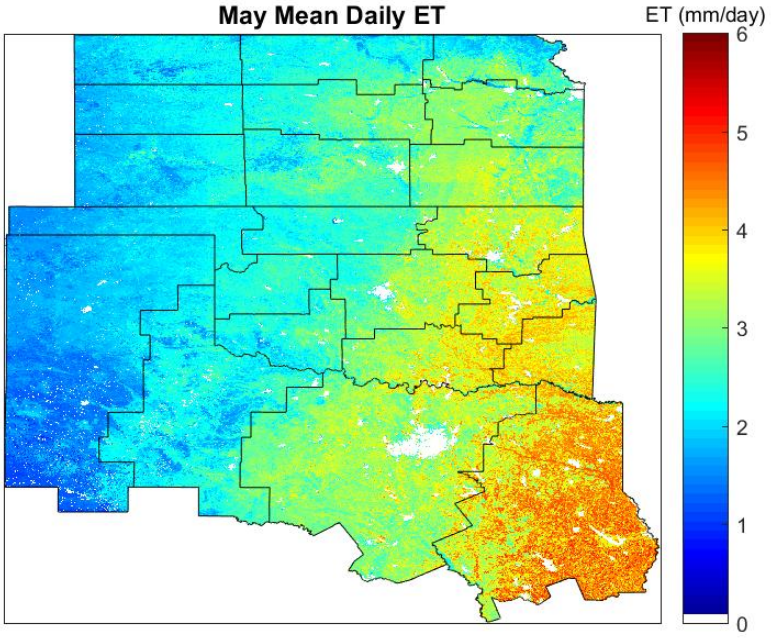

Figure 5.16: Average daily ET estimates from BESS during May from 2000-2015.

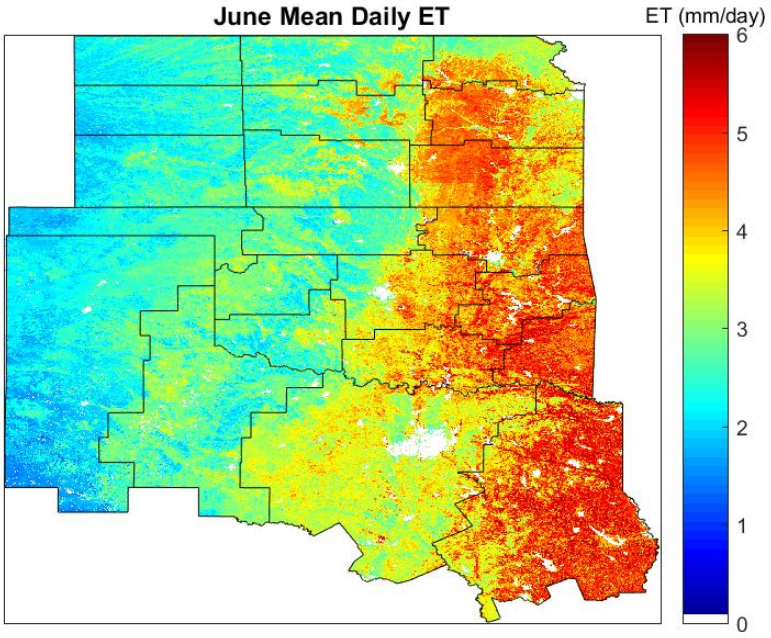

Figure 5.17: Average daily ET estimates from BESS during June from 2000-2015.

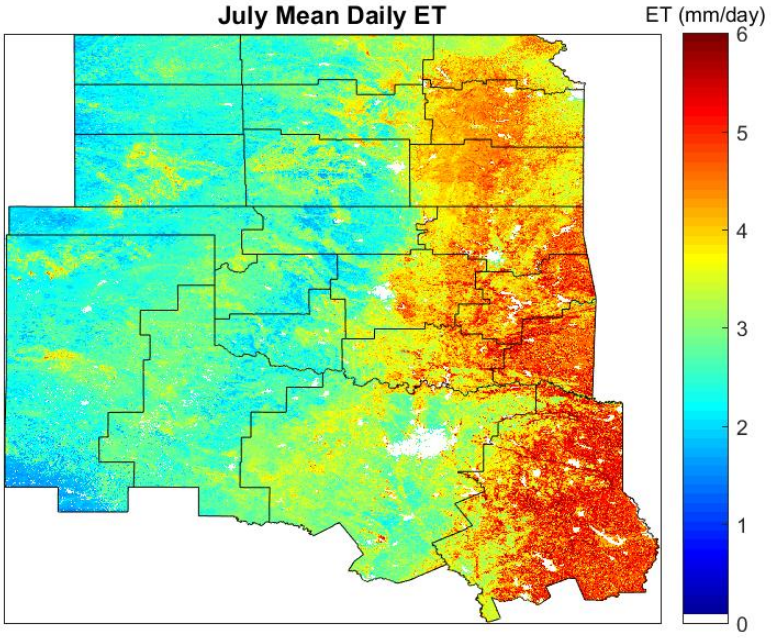

Figure 5.18: Average daily ET estimates from BESS during July from 2000-2015.

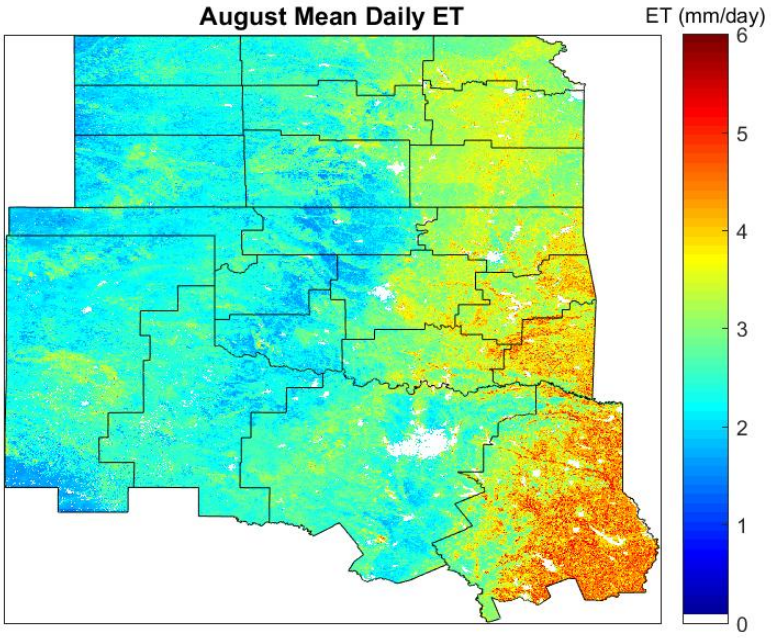

Figure 5.19: Average daily ET estimates from BESS during August from 2000-2015.

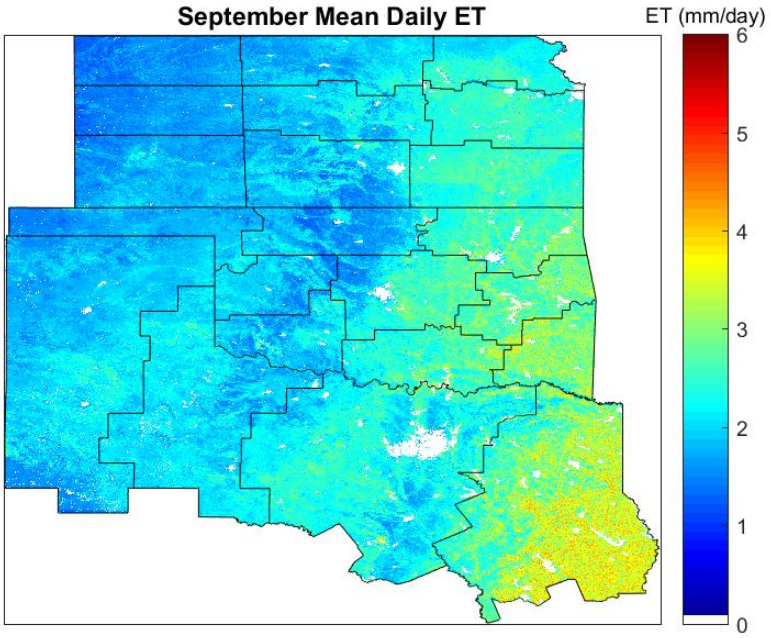

Figure 5.20: Average daily ET estimates from BESS during September from 2000-2015.

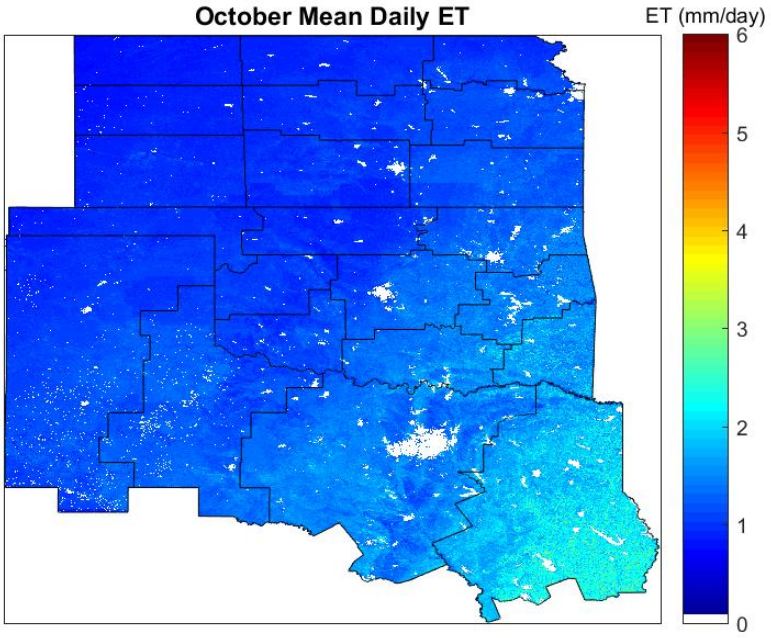

Figure 5.21: Average daily ET estimates from BESS during October from 2000-2015.

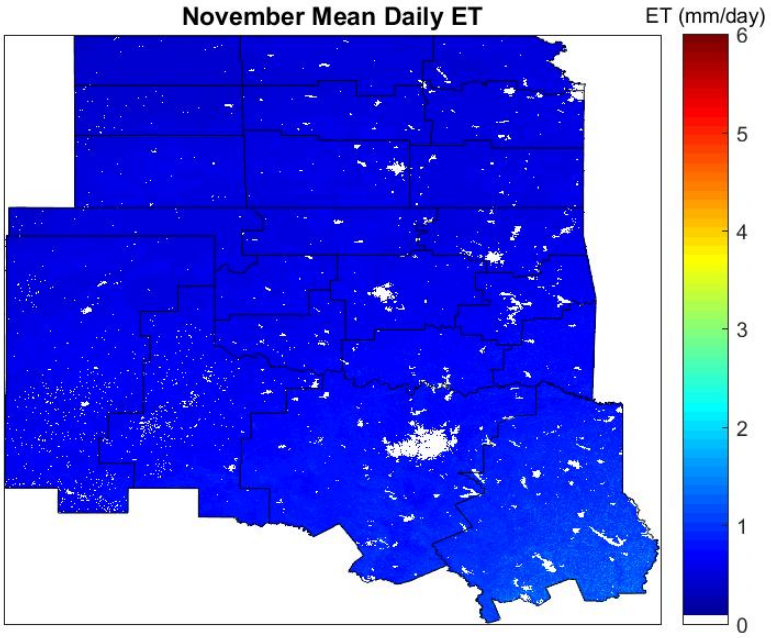

Figure 5.22: Average daily ET estimates from BESS during November from 2000-2015.

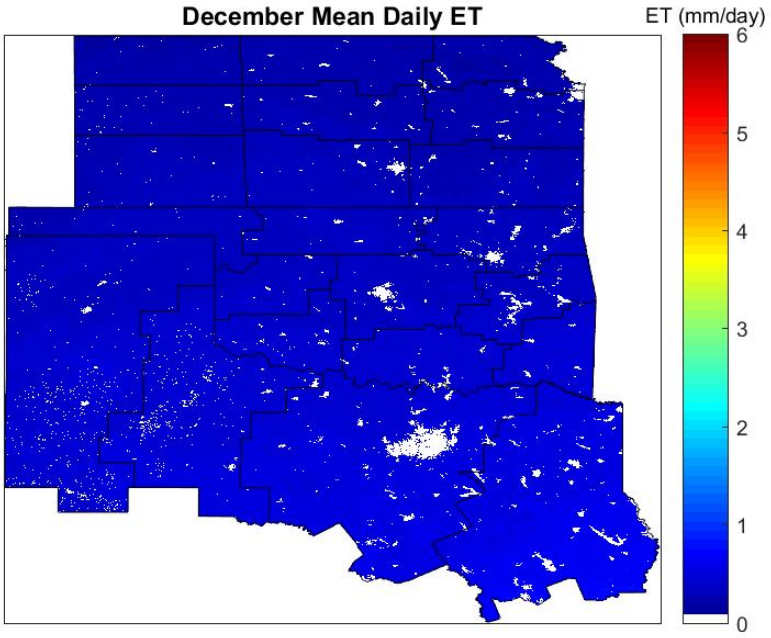

Figure 5.23: Average daily ET estimates from BESS during December from 2000-2015.

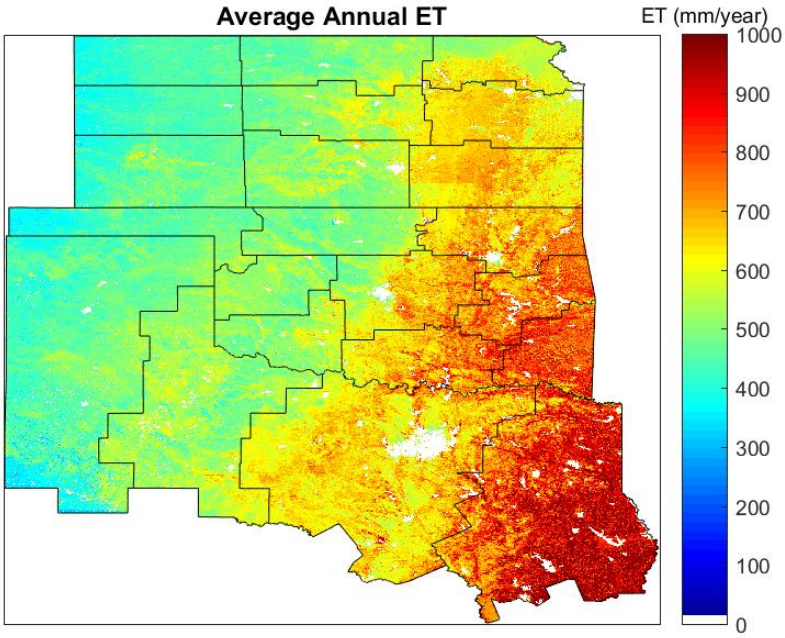

Figure 5.24: Average annual ET estimates from BESS values from 2000-2015.

5.3.2 Variability Analysis

Interannual variability of ET is poorly modeled by land-surface models, so it is important to determine whether BESS is able to represent the interannual variability of ET (Jiang and Ryu 2016). Only 34 years of the 60 total years of in-situ data analyzed was continuous for the entire year, so only those continuous years were used to compare how well BESS captures the interannual variability of ET (Fig. 5.25). The Kansas Land Institute, SGP ARM Main, Kansas Field Station, Walnut River, Konza LTER, and Konza Prairie sites are separated in Figure 5.25. Overall, BESS underestimated annual ET for 25 years, but overestimated ET only during 6 years. There were only 3 years in which BESS and the observed annual sum of ET were in agreement. When BESS overestimated ET it was not by more than ~100 mm, but BESS can underestimate ET by as much as 300 mm. The average bias of BESS was -106 mm for the 34 years.

Analyzing each site individually, KLI decreased by 100 mm of ET from one year to the next. BESS captured the decreasing trend in ET, but the magnitude was only 25 mm. SGP ARM Main varies significantly from year-to-year and BESS was able to capture the general trend of variability in 6 of the 12 years. There was little variability in observed and estimated ET at KFS, but BESS agreed closely with the magnitude of ET for the first three years and then BESS overestimated ET for the last three years. The increasing trend in ET was captured for WR with a slight overestimation in magnitude by BESS. ET varied significantly at LTER, but little variability was displayed by BESS. The same can be said for Konza Prairie, which is located close to the LTER so it is understandable that BESS performs similarly at both. Overall, BESS better represented years that have lower ET values than years that have high ET values.

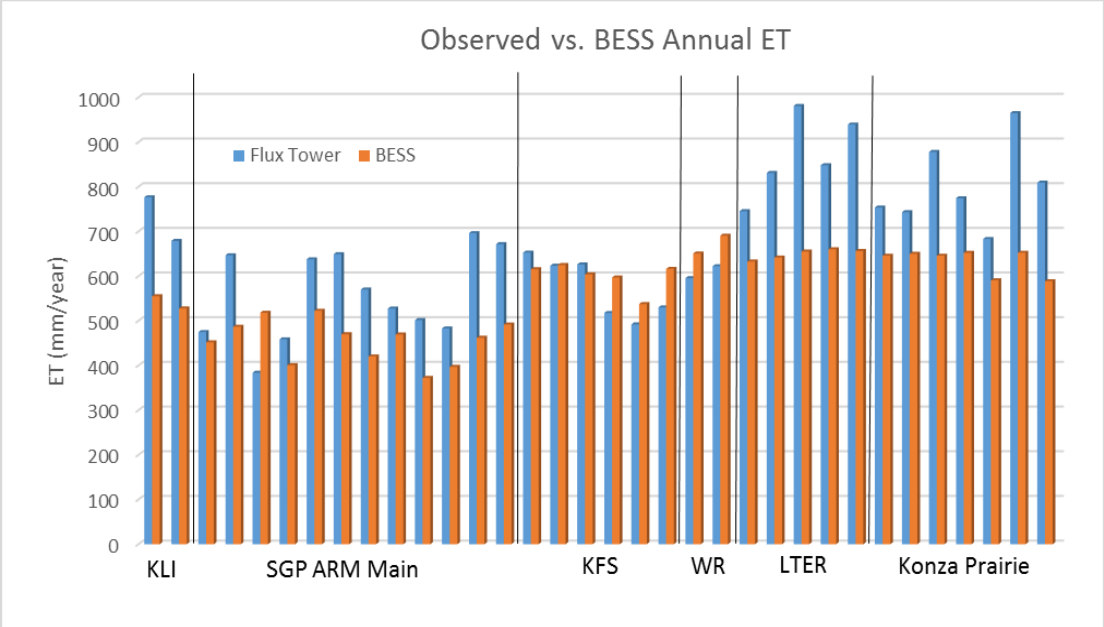

Figure 5.25: Annual sums of ET at each flux tower with a full year of data compared to the annual sum of ET from BESS at the corresponding tower. KLI-Kansas Land Institute (2013-2014), SGP ARM Main (2003-2014), KFS-Kansas Field Station (2008-2013), WR-Walnut River (2003-2004), LTER-Konza LTER (2008-2013), Konza Prairie (2008-2014).

ET anomalies, defined as the difference between the each year and the 2000-2015 yearly average, generated from BESS for 2000-2015 highlight which years experienced healthy vegetation with moist soil conditions versus years that were water stressed with poor vegetation health likely associated with drought conditions (Figs. 5.26-5.41). Years that experienced anomalously low ET include 2000 (Fig. 5.26), 2006 (Fig. 5.32), 2011 (Fig. 5.37), and 2012 (Fig. 5.38). Years with anomalously high ET include 2007 (Fig. 5.33) and 2015 (Fig. 5.41).

Drought conditions were assessed using the United States Drought Monitor (Svoboda et al. 2002) that categorizes drought conditions into 5 categories: abnormally dry, moderate drought, severe drought, extreme drought, and exceptional drought. In

2000 annual ET values over the southern half of the SGP were 100-200 mm below average (Fig. 5.26). These low values in ET correspond to severe drought conditions that encompassed much of the southern portion of the SGP for a longer period of time than regions further north. This explains why ET was lower in the southern portion of the SGP than the northern portion. In 2006 severe drought occurred in Texas and Oklahoma at the start of the growing season. Toward the end of the growing season extreme drought extended into Oklahoma with exceptional drought in northern Texas. ET was less anomalous in 2006 as 2000 because of drought relieving precipitation that occurred in April and May that created high ET rates during the peak portion of the growing season. The most significant ET departures on a scale that encompassed all but the three northern climate divisions of the SGP (Fig. 5.37) occurred in 2011 whereby the ET departures were over 200 mm below normal in some areas. These ET departures were associated with exceptional drought across Texas, Oklahoma, and Southern Kansas. The three northern climate divisions that did not experience anomalously low ET did not experience drought during much of the growing season in 2011. In 2012 ET departures appeared across Oklahoma, Kansas, and the Texas panhandle (Fig. 5.38). This same region experienced extreme to exceptional drought during 2012. Northern and northeast Texas were drought-free, which can explain the normal ET values in this area. Overall, BESS produced low ET values during periods of drought over the SGP.

In regards to pluvial years, BESS modeled above average ET across the SGP. Pluvial years were assessed using the Parameter elevation Regression on Independent Slopes Model (PRISM) precipitation dataset that is used as the USDA's climatological data (NCAR 2015). During 2007 and 2015, BESS produced above average ET (Figs.

5.33 and 5.41). In 2007 the western half of the SGP had ET values 100-200 mm above average. Monthly rainfall from March-August of 2007 was 150-400% above normal. The wettest area of the SGP was in the southwestern portion of the domain. This area also corresponds to the highest departures from average ET. 2015 was also another abnormally wet year in the SGP that is associated with high ET produced by BESS (Fig. 5.41); ET values range from 75-150 mm above normal across the western half of the SGP. Precipitation was 200% above normal in northern Texas and southern Oklahoma as well as in the Texas and Oklahoma panhandles. The above normal ET that occurred in the western potion of the domain did not occur in southern Oklahoma and northern Texas despite this area receiving above normal rainfall as well.

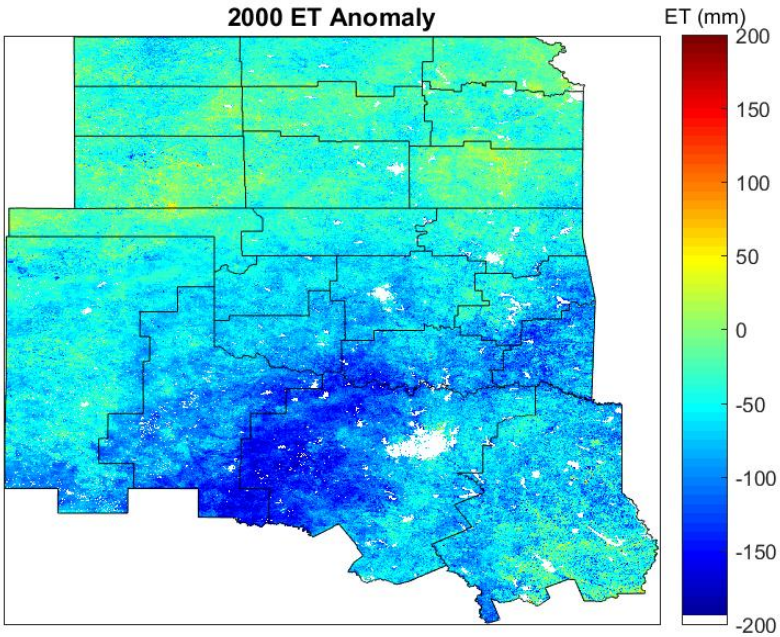

Figure 5.26: ET anomaly estimates from BESS during 2000 for the SGP with climate divisions contoured.

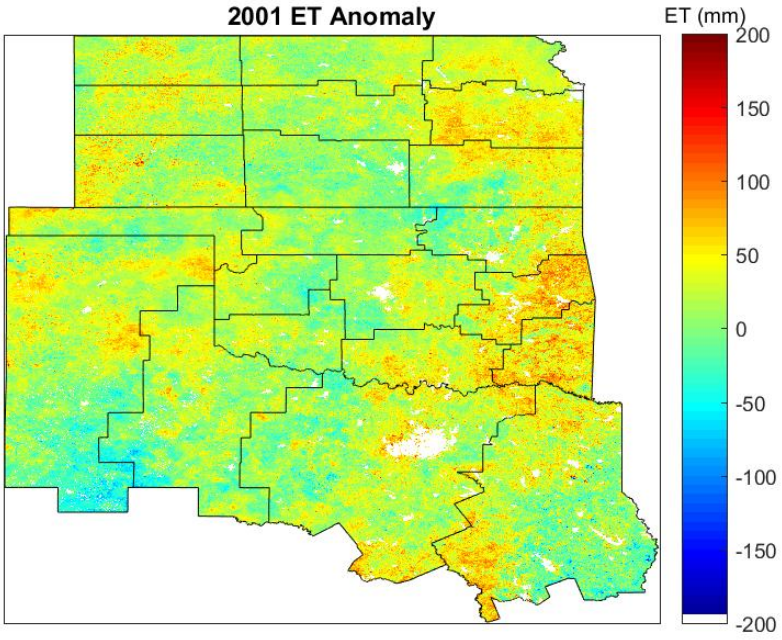

Figure 5.27: ET anomaly estimates from BESS during 2001.

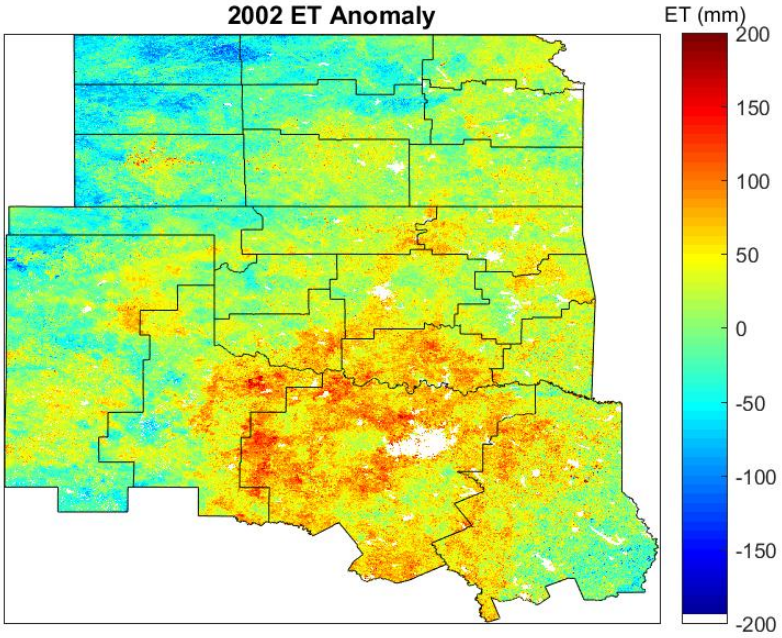

Figure 5.28: ET anomaly estimates from BESS during 2002.

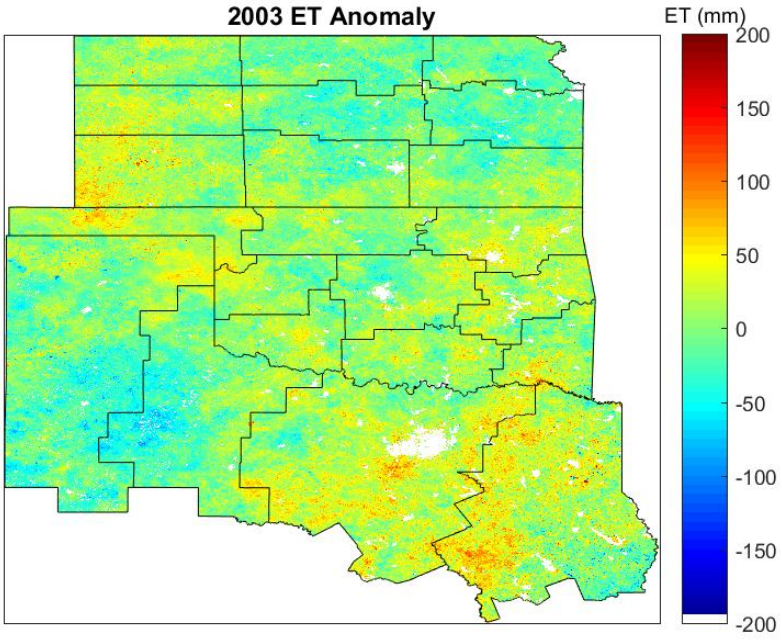

Figure 5.29: ET anomaly during 2003.

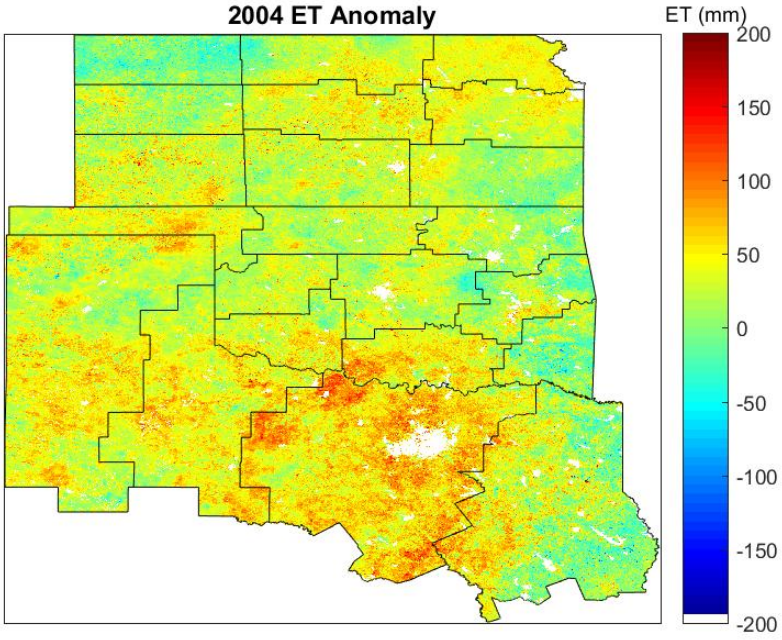

Figure 5.30: ET anomaly estimates from BESS during 2004.

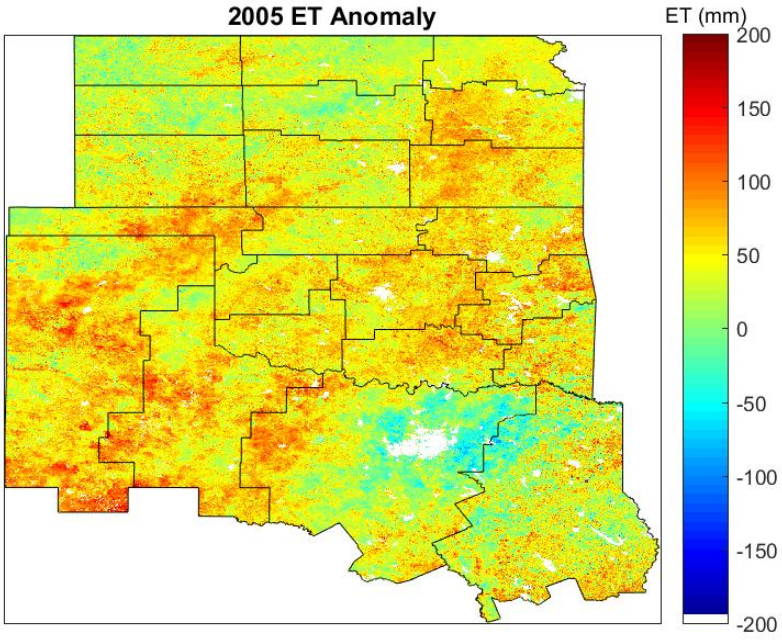

Figure 5.31: ET anomaly estimates from BESS during 2005.

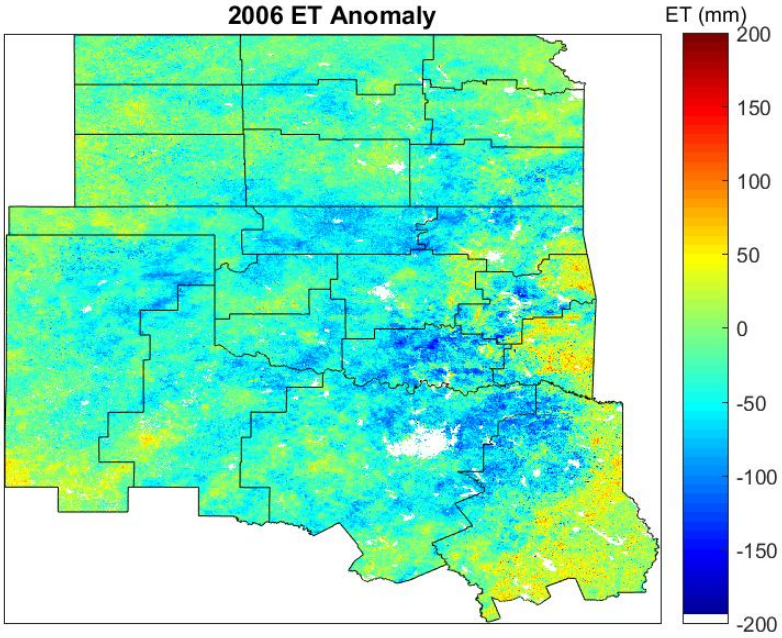

Figure 5.32: ET anomaly estimates from BESS during 2006.

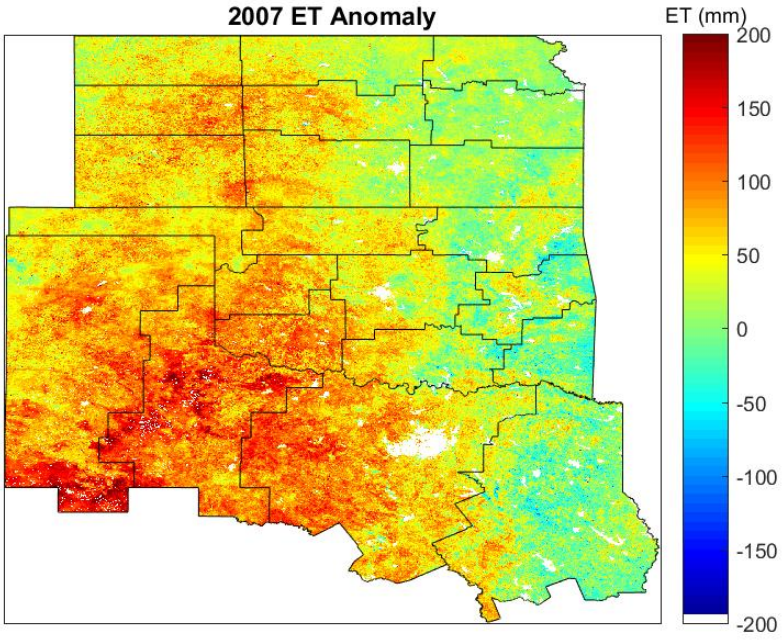

Figure 5.33: ET anomaly estimates from BESS during 2007.

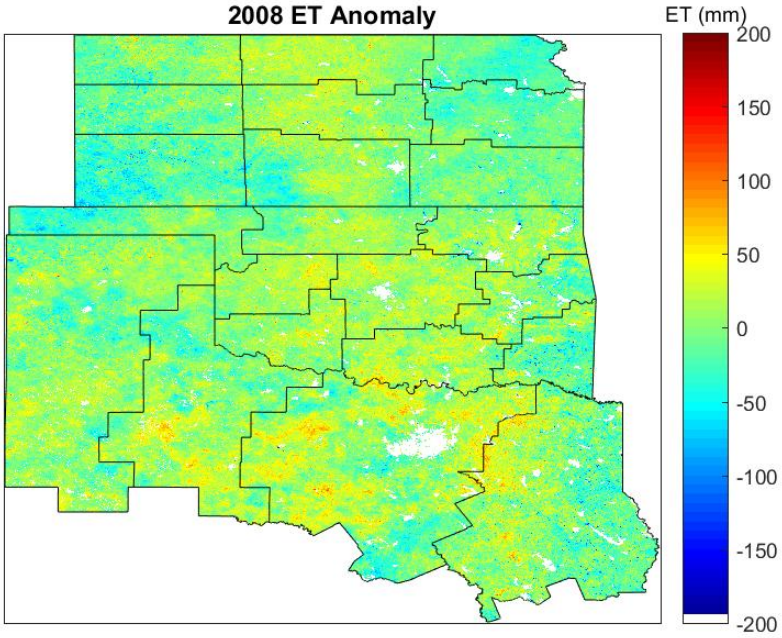

Figure 5.34: ET anomaly estimates from BESS during 2008.

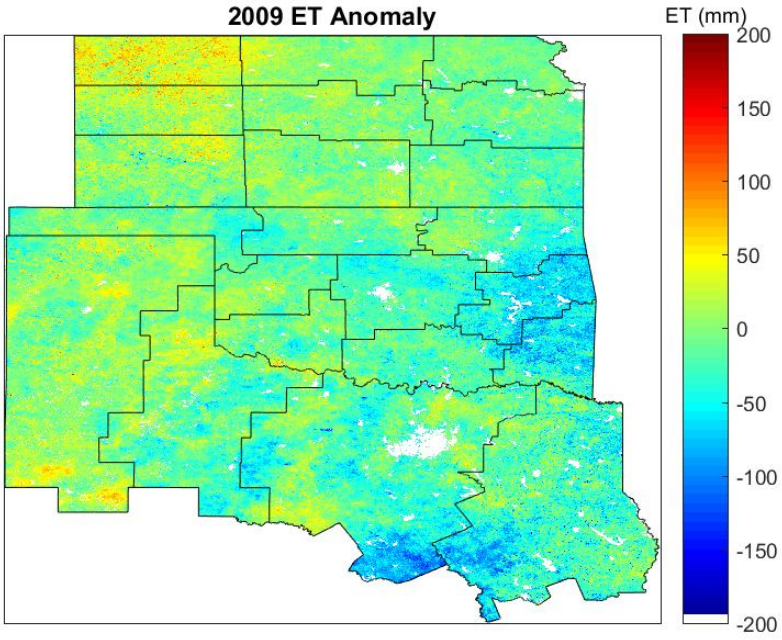

Figure 5.35: ET anomaly estimates from BESS during 2009.

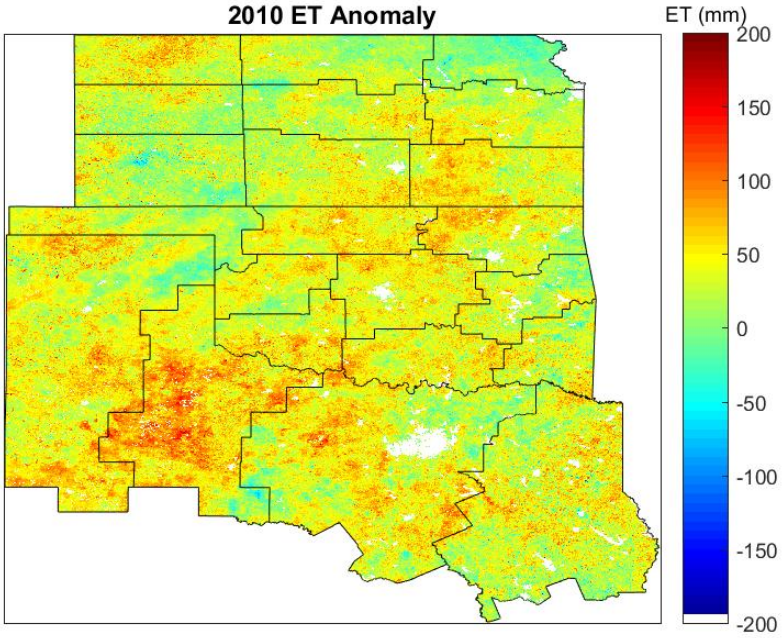

Figure 5.36: ET anomaly estimates from BESS during 2010.

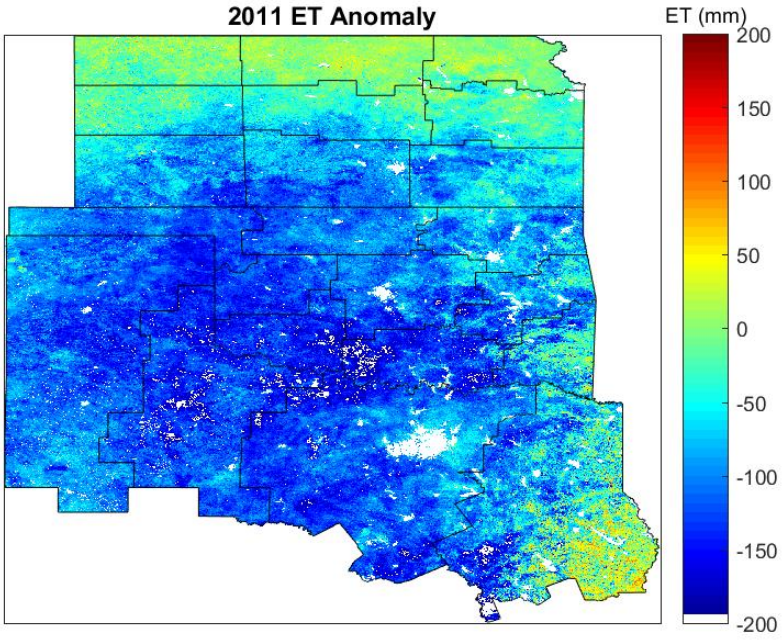

Figure 5.37: ET anomaly estimates from BESS during 2011.

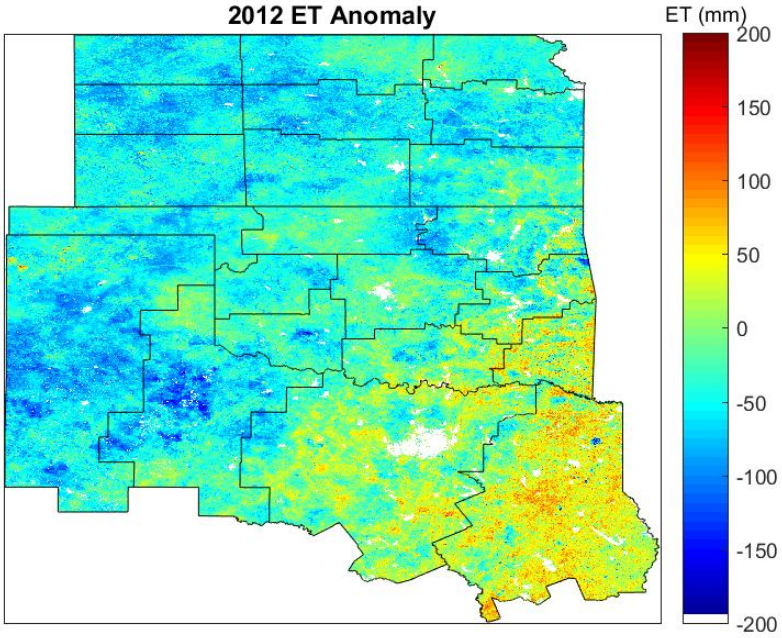

Figure 5.38: ET anomaly estimates from BESS during 2012.

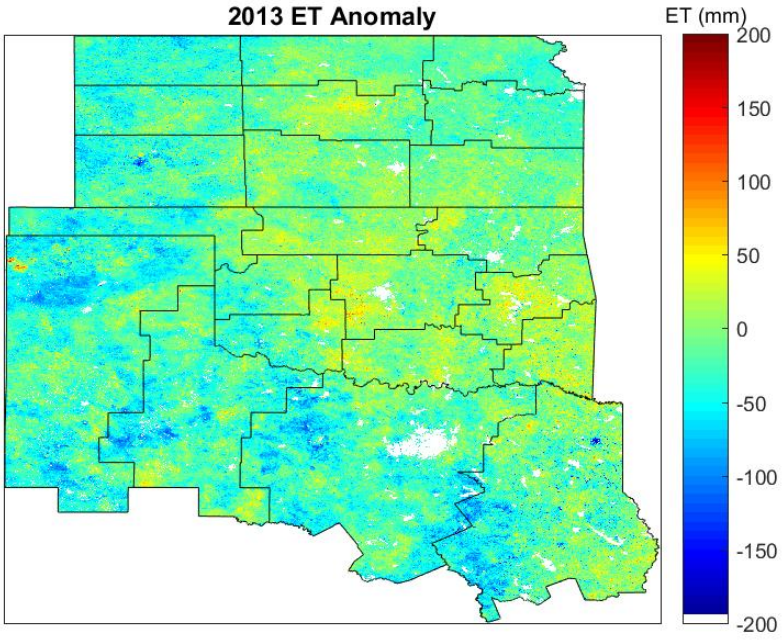

Figure 5.39: ET anomaly estimates from BESS during 2013.

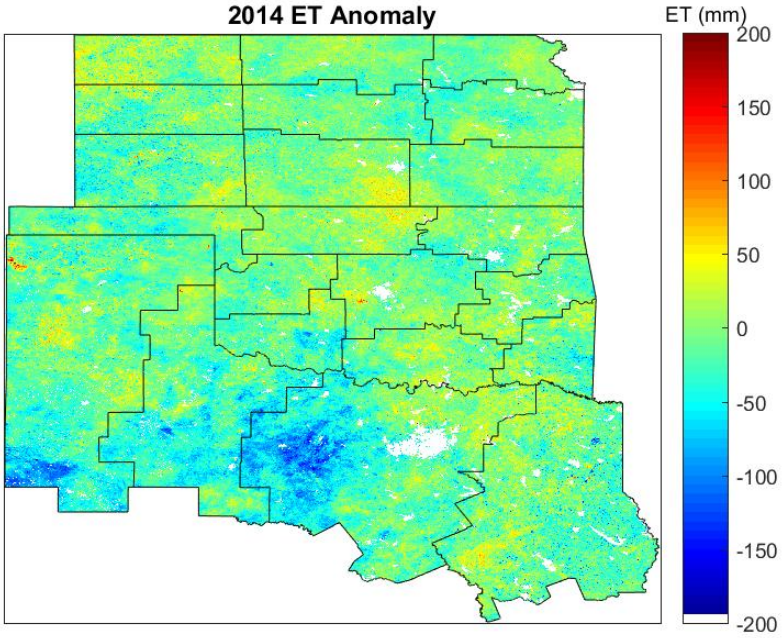

Figure 5.40: ET anomaly estimates from BESS during 2014.

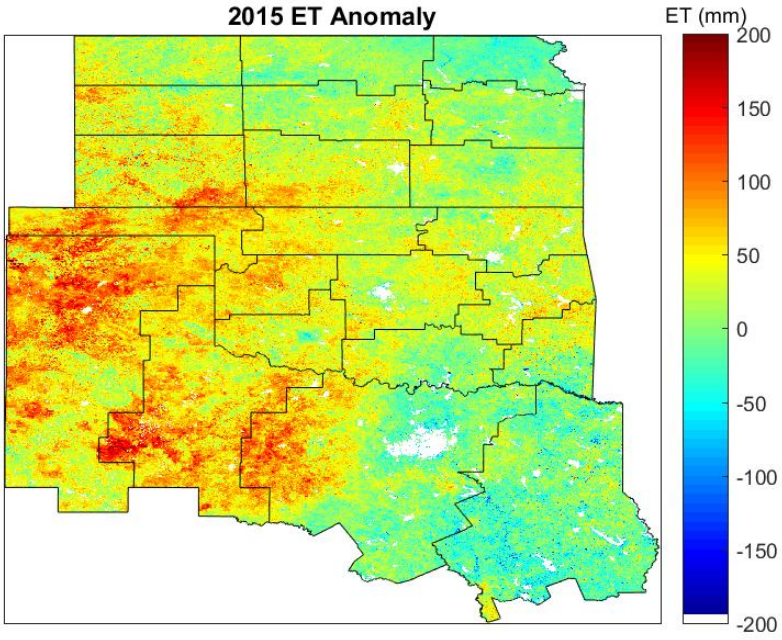

Figure 5.41: ET anomaly estimates from BESS during 2015.

Annual variability of ET is greatest over the southwestern portion of the SGP where ET varied between 90-100 mm/year (Fig. 5.42). The least variable portions were in the southeast and northern SGP where variability is less than 40 mm/year. A hypothesis as to why such variability exists is that land-use and land-change practices occur in this region of the SGP from crop rotations. Because flux towers were not deployed in this area of high variability, it is unclear whether or not this variability is real or if it is an artifact from BESS. For example, the Konza LTER and Konza Prairie sites mentioned in Figure 5.25 show high interannual variability, but BESS shows very little interannual variability. Thus, it is difficult to determine whether BESS is able to capture the interannual variability in all portions of the SGP.

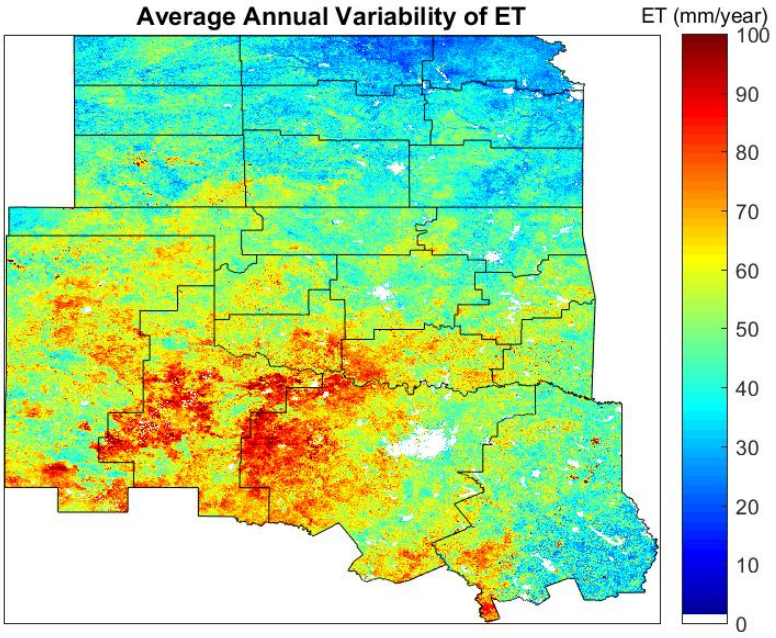

Figure 5.42: Standard deviation of ET estimates from BESS from 2000-2015.

5.3.3 Water Budget Analysis

Average precipitation was calculated for 2000-2014 over the SGP using the nclimdiv dataset (Christian et al. 2015). Precipitation ranged from 550 mm in 2011 to 977 mm in 2004, and ET ranged from 488 mm in 2011 to 624 mm in 2007 (Fig. 5.43). As precipitation in a given year increased, ET increased as well. The average amount of precipitation for the SGP over this period was 760 mm and the average ET was 566 mm. Precipitation partitioning varied interannually and ranges from 62% in 2004 to 93% in 2005 (Fig. 5.44). Thus, on average 76% of precipitation that enters the SGP leaves the system via ET. These values agree with the findings of Ford et al. (2007) that showed 50-90% of precipitation was converted to ET. However, this 76% is 16% higher than the 60% average calculated from Trenberth et al. (2007).

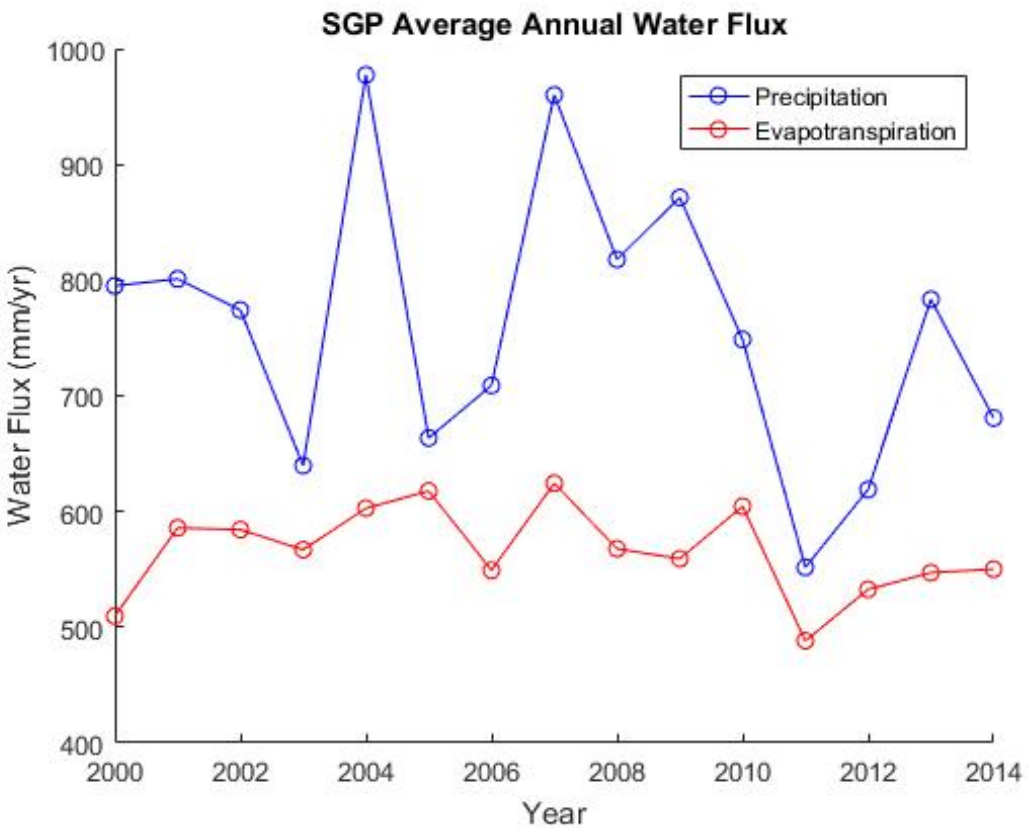

Figure 5.43: SGP spatial and annual average of precipitation from nclimdiv dataset and average ET from BESS from 2000-2014.

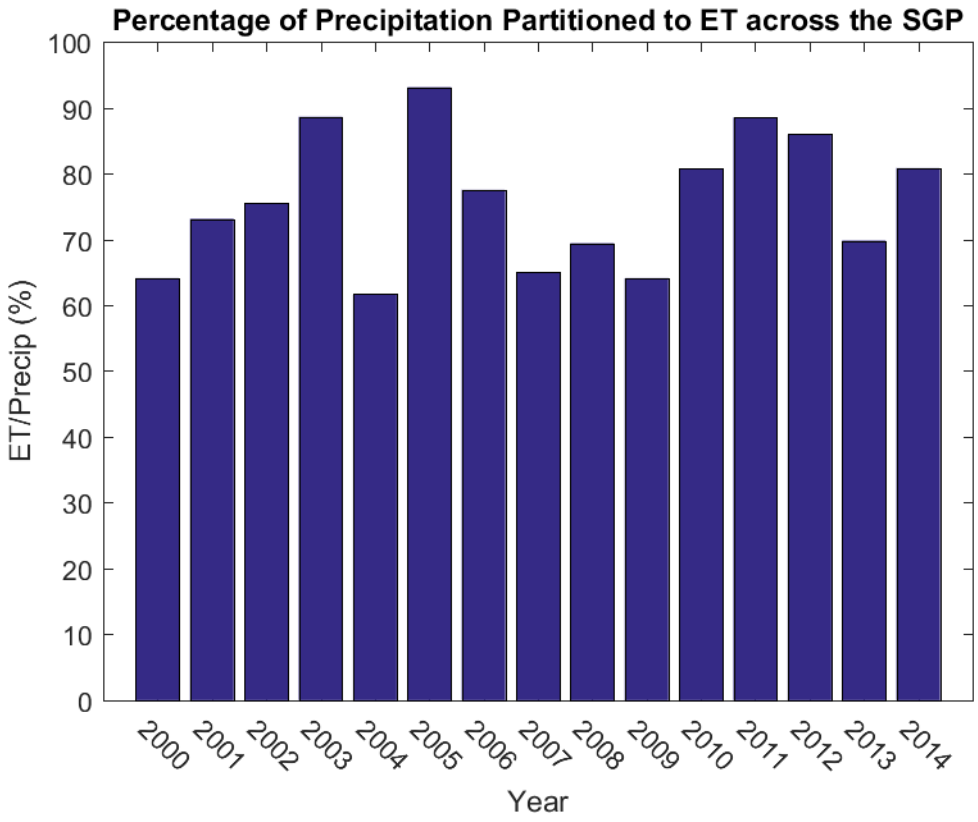

Figure 5.44: Ratio of ET to Precipitation across the SGP from 2000-2014.

5.3.4 Sensitivity Analysis

A relative sensitivity of ET was calculated using an index (Beven, 1979; McCuen, 1974; Ryu et al. 2011):

$$S_i = \frac{\partial ET}{\partial V}\frac{V}{ET} \quad \textbf{(5.1)}$$

where S_i is the relative sensitivity, ET is the Penman-Monteith equation for evapotranspiration, and V is the input variable into the equation. In this analysis V is available energy (Rn – G), vapor pressure deficit (VPD), canopy conductance (gs), aerodynamic conductance (ga), and the energy balance closure (I). When S_i is -1 the input variable is highly negatively correlated with ET and when it is +1 it is highly

positively correlated. Figure 5.44 shows that BESS-derived ET over the SGP is most highly positively correlated (>0.7) with available energy during the growing season, moderately positively correlated (>0.5) with canopy conductance, slightly positively correlated (>0.2) with vapor pressure deficit, and slightly negatively correlated (<-0.2) with aerodynamic conductance. The energy balance closure is 0 because BESS equates the available energy coming into the system to the energy leaving the system via latent and sensible heating. Therefore, BESS-derived ET is most sensitive to changes in available energy. This may not be the case during water-stressed periods as available energy becomes less correlated when water is limited; canopy conductance becomes more correlated during these periods (Ryu et al. 2011; Hasler and Avissar, 2007).

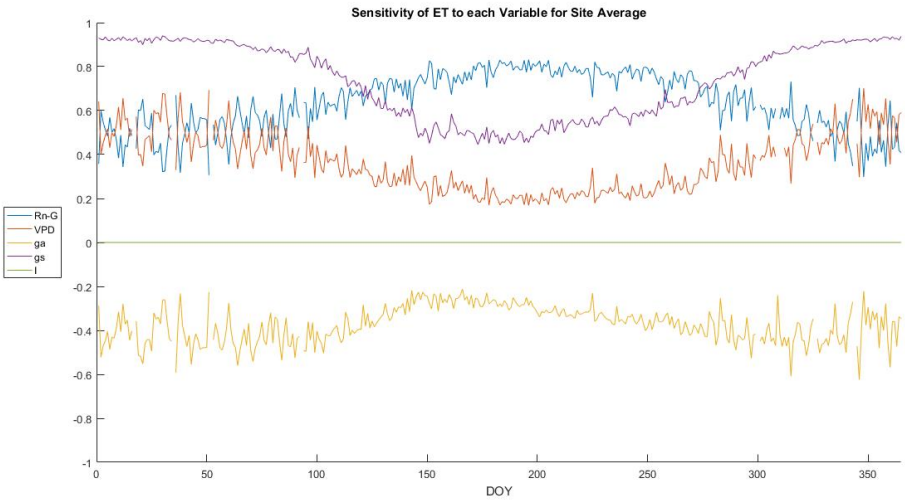

Figure 5.45: Average sensitivity of ET in the Penman-Monteith equation to five controlling variables at each flux tower site. Where available energy is Rn-G, vapor pressure deficit is VPD, gs is stomatal conductance, ga is aerodynamic conductance, and energy balance closure is I.

Chapter 6 : Flash Drought Case Study

6.1 Flash Drought Development

During 2012, flash drought conditions occurred at the Marena location as conditions transitioned from no drought in April to D4 (exceptional drought) in mid August. The array of instruments captured the dramatic transition of land-surface conditions at the Marena site. Results for the analyses demonstrated that both meteorological conditions and surface conditions were critical components to flash drought development. Further, BESS was analyzed as a proxy for predicting the flash drought conditions.

6.1.1 Flash Drought Category Evolution

Flash drought is a relatively new concept in understanding drought dynamics (Senay et al. 2008; Hunt et al. 2009). Flash droughts are characterized by anomalously high temperatures, below normal precipitation before onset, and increased ET prior to onset that leads to a decrease in soil moisture followed by a decrease in ET and rapid intensification of drought on the scale of days and weeks (Mo and Lettenmaier 2015; Mo and Lettenmaier 2016). Several studies have concluded that a large portion of the SGP (specifically Oklahoma, Kansas, and the Texas Panhandle) experienced flash drought during 2012 (Otkin et al. 2013a; Otkin et al. 2013b; Mo and Lettenmaier 2015; Mo and Lettenmaier 2016).

During June of 2012 drought conditions across Oklahoma were confined to the southeast, southwest, and pandhandle regions of the state with only abnormally dry conditions at the Marena site (Fig. 6.1). Within two months Marena escalated from no drought to exceptional drought, the highest classification (Fig. 6.2). At the Marena site a

phenological camera (phenocam) collects images of the vegetation on a daily basis to visually observe the health and growth of the ecosystem. Further, the images can be used to calculate greenness indices. On July 1, 2012 the vegetation was still green and visually healthy (Fig. 6.3). A month and a half later the entire ecosystem collapsed (Fig. 6.4).

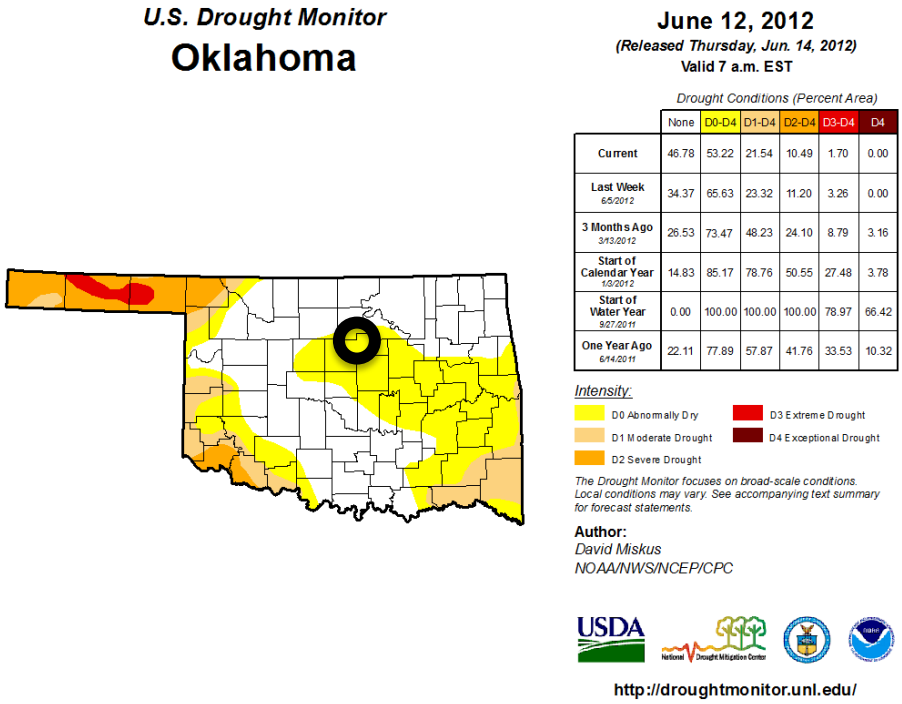

Figure 6.1: United States Drought Monitor depicting the drought conditions during the onset of flash drought with the Marena site circled.

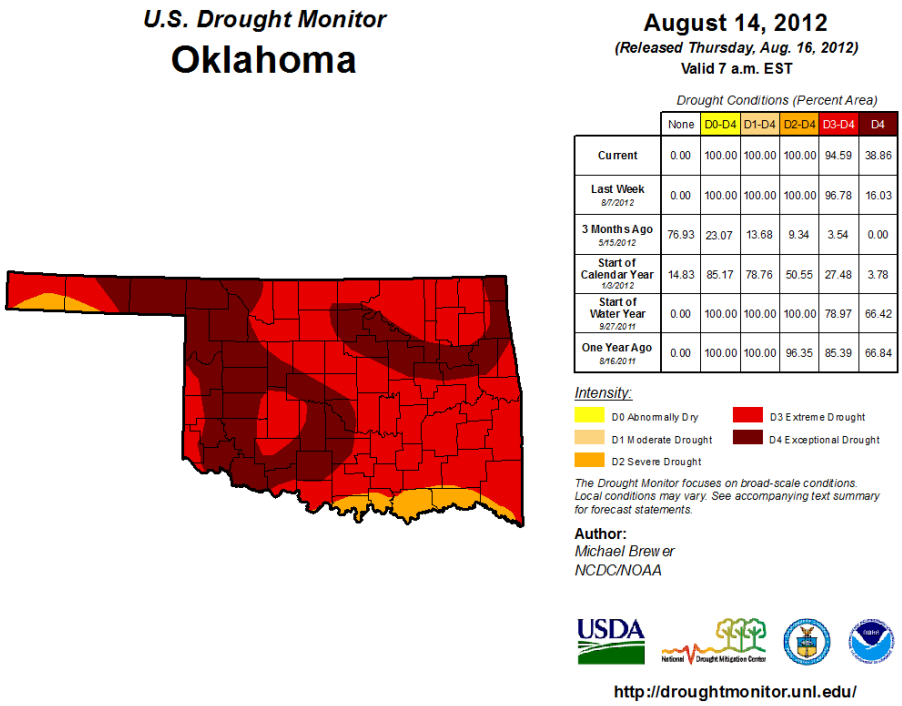

Figure 6.2: United States Drought Monitor depicting the drought conditions as a result of the flash drought.

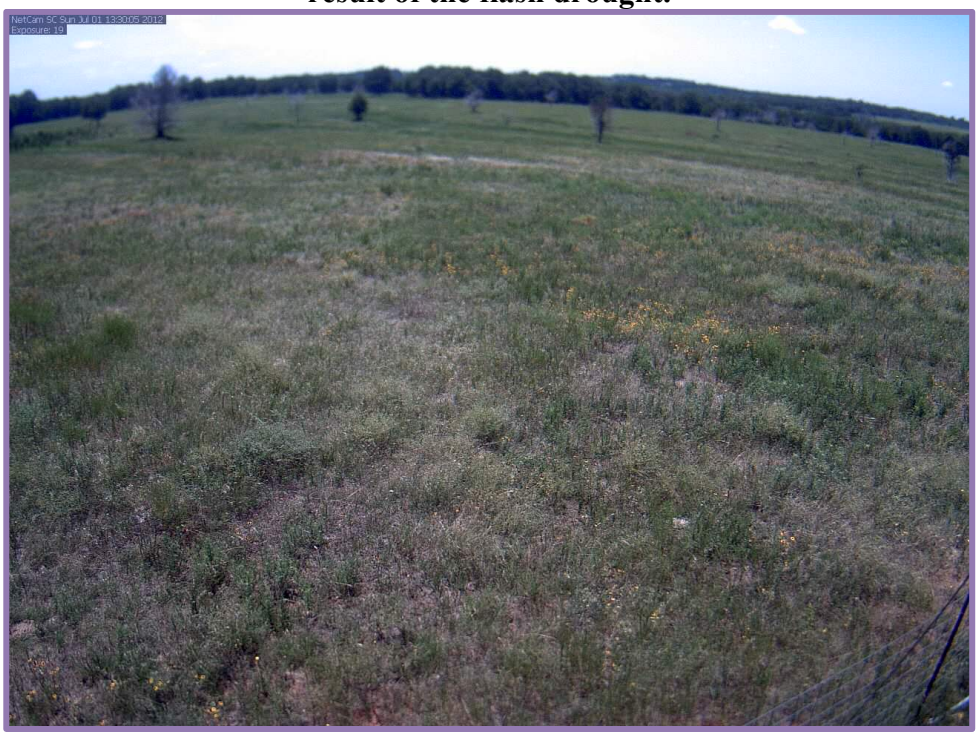

Figure 6.3: Phenocam image taken at Marena on July 1, 2012.

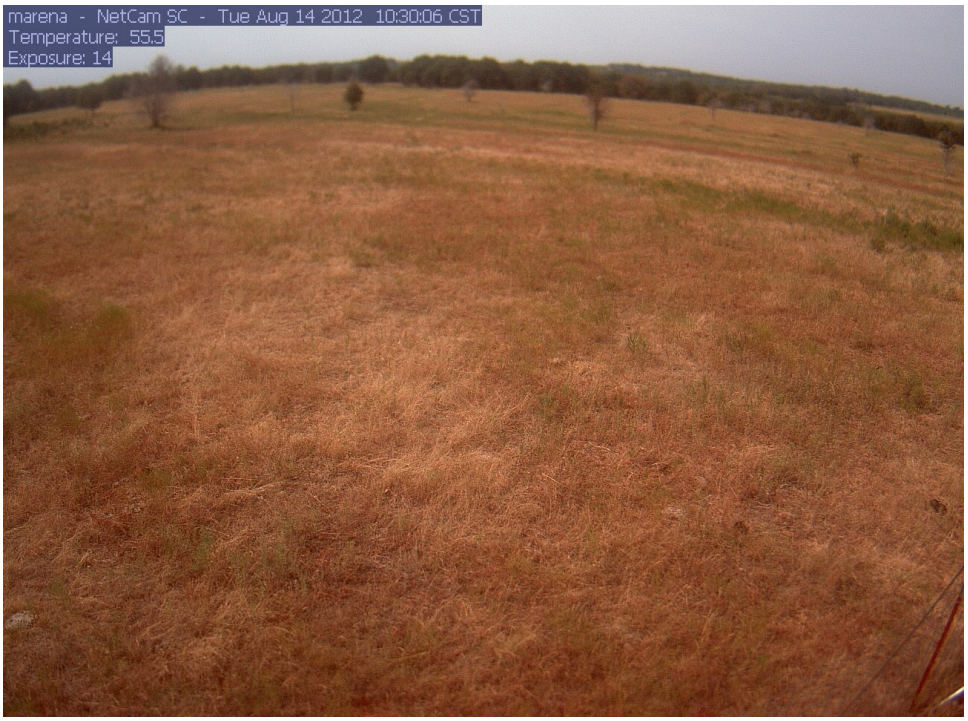

Figure 6.4: Phenocam image taken at Marena on August 14, 2012.

6.1.2 Flash Drought Meteorological Influence

The main meteorological drivers that accompanied the 2012 flash drought were precipitation and air temperature. Before the onset of flash drought precipitation, was 100 mm above normal during the spring (Fig. 6.5) and air temperatures values were 2-7^{o}C above normal. This led to an early onset of the growing season and for a pre-mature growth in vegetation. Towards the end of April and throughout May very little precipitation fell leading to abnormally dry conditions. However, a key feature in the precipitation pattern was the large amount of rain that fell in June. However, a second dry spell occurred from July until the middle of August during which almost no precipitation fell, and air temperatures remained above normal by 2-5^{o}C.

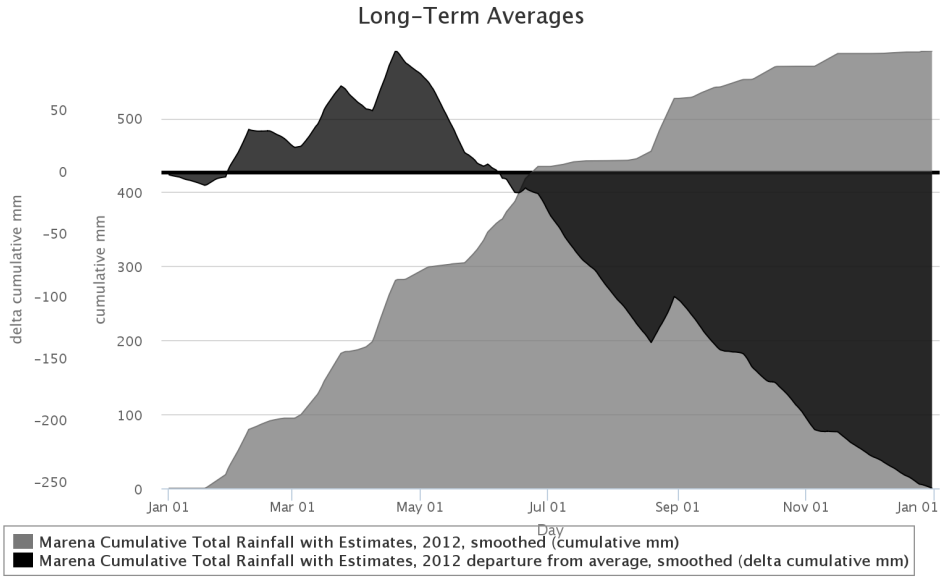

Figure 6.5: Cumulative precipitation and anomalous cumulative precipitation at the Marena Mesonet site in 2012.

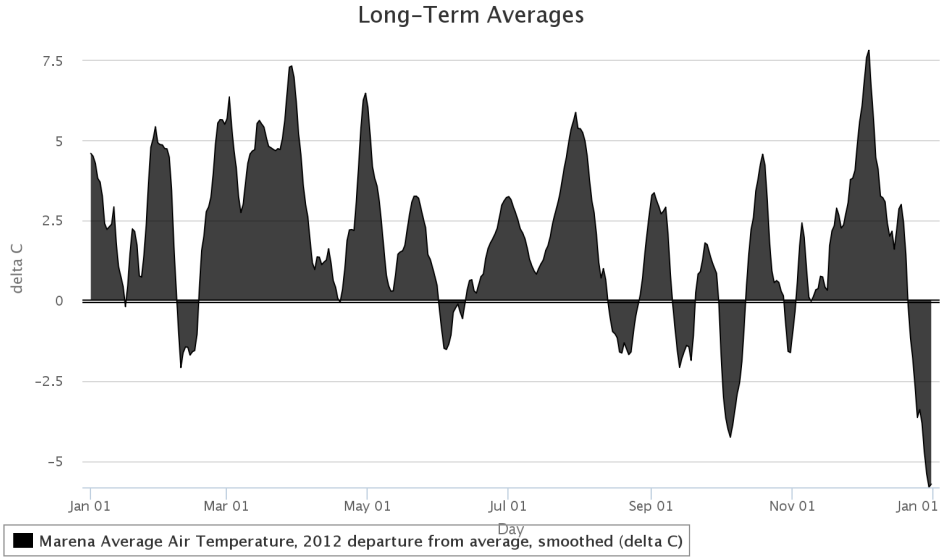

Figure 6.6: Anomalous average air temperature at the Marena Mesonet site in 2012.

6.1.3 Flash Drought Soil Moisture Conditions

Understanding the soil moisture component is pivotal for diagnosing the onset of flash drought. A cosmic soil moisture observing system (COSMOS) instrument was deployed at the Marena site during the flash drought period (Shuttleworth et al. 2010). COSMOS instruments estimate soil moisture by measuring cosmic-ray neutrons emitted from the soil. The intensity of the neutrons is directly related to water content. The COSMOS has a measuring radius of 350 m and a penetration depth of 15-70 cm. The soil moisture profile at Marena was moist (~20%) through April due to the above normal precipitation (Fig. 6.7). However, by mid-April soil moisture decreased to about half (~10%) of the content of the early spring. Soil moisture rebounded above 15% in June associated with the increased precipitation which was followed by a sharp decline in soil moisture (~ 5%) during the development of the flash drought.

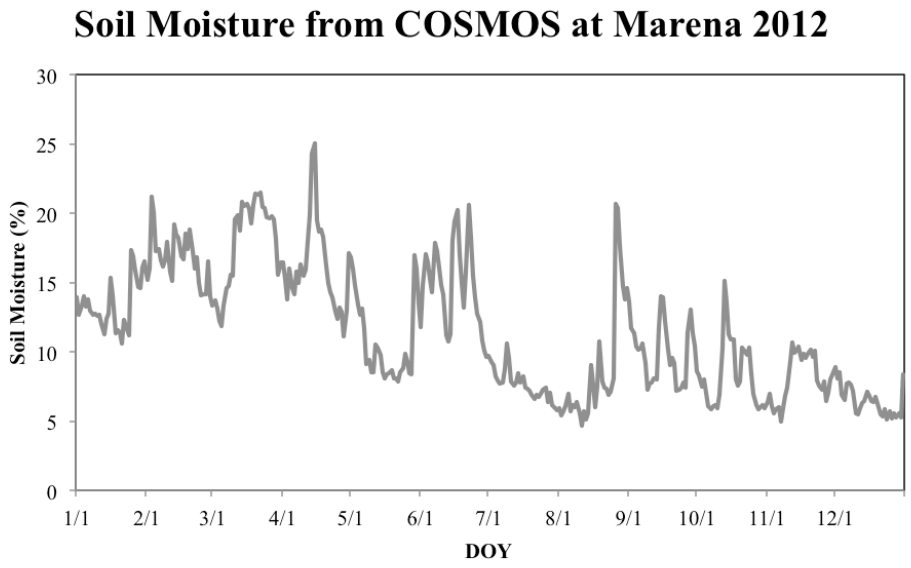

Figure 6.7: Soil moisture percentage measured by COSMOS at Marena 2012.

The Marena Mesonet site, co-located at the MOISST site, provided additional soil moisture data at 5, 25, and 60 cm (Fig. 6.8). During the moist part of the year, all depths yielded fractional water content values near 1 signifying very moist conditions. Soil moisture at all depths decreased during the dry period from mid-April through May. The 5 and 25 cm soil moisture fell to nearly 0.1 while the 60 cm measurement reached 0.6. With the June rain the shallow soils recovered to near 0.8; however this precipitation never penetrated deeper such that the 60 cm soil moisture remained quasi-constant at approximately 0.6. During the second dry period the shallow soil moisture diminished again to 0.1, and the deeper soil moisture decreased to 0.2. Even though the second dry period was the main contributor to the decrease in soil moisture throughout the entire column it is the first dry period that initially decreased the soil moisture, especially deeper than the surface layer, and led to rapid drying in July and August.

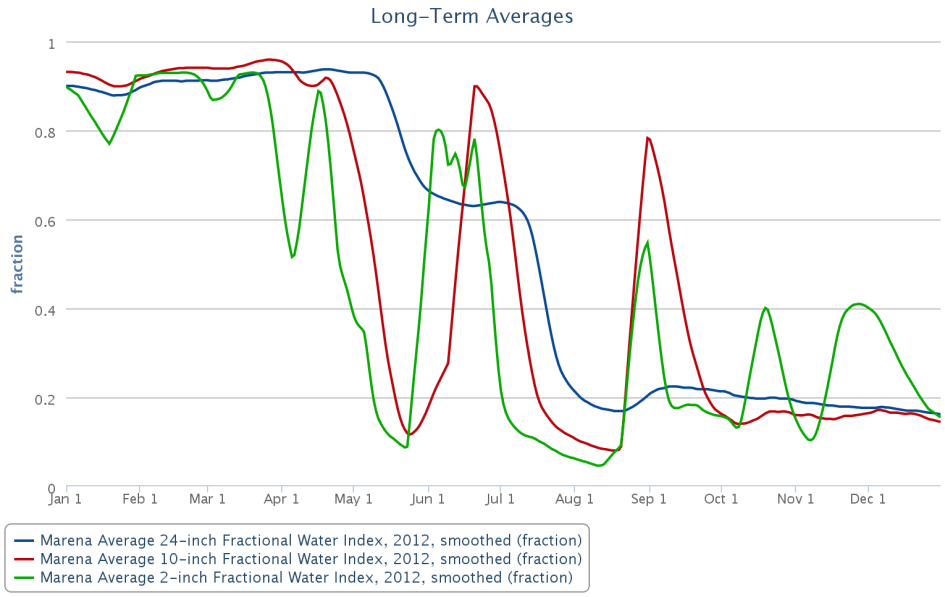

Figure 6.8: Marena 2012 Mesonet fractional water index at 2, 10, and 24 inch depths.

6.1.4 Evaporative Perspective on Flash Drought

Evaporative fraction (EF) is the ratio of latent heat to the sum of latent and sensible heat

$$\boldsymbol{EF = \frac{LE}{LE + SH}} \tag{6.1}$$

where LE is latent heat flux and SH is sensible heat flux. Values below 0.5 indicate that sensible heating is the dominant term and that more energy is partitioned towards sensible heating versus latent heating. Conversely, values above 0.5 indicate that latent heating is the dominant term. The variability of EF at Marena in 2012 corresponds well with the changes in soil moisture (Fig. 6.9). For example, EF values were near 0.9 prior to the first dry period and is indicative that soil moisture was being extracted during this

period. Due to the abnormally warm conditions in the early part of the season, vegetation reached peak maturity earlier in the season. This created a longer period for mature vegetation to utilize more soil moisture. Thus, during the first dry period EF fell to 0.5 because of decreased shallow soil moisture. Once the shallow soil moisture was reduced the deeper soil moisture was used to meet the demand in ET rates. With the wet June only shallow soil moisture was recharged and the latent heating term became dominant again. This second period had ET rates (~4.5 mm/day) that were near the average ET rates for this time of year when soil moisture is normal (Fig. 6.10). However, soil moisture was below normal, especially at deeper detpths. Due to the high temperatures, abundant shallow soil moisture, healthy vegetation, and high ET rates, the deep soil moisture was quickly depleted once the precipitation stopped. This chain of events led to a rapid development of drought noted by the dramatic change in vegetation conditions via the phenocam images, depleted soil moisture, and ET rates 3 mm/day below normal (Fig. 6.10).

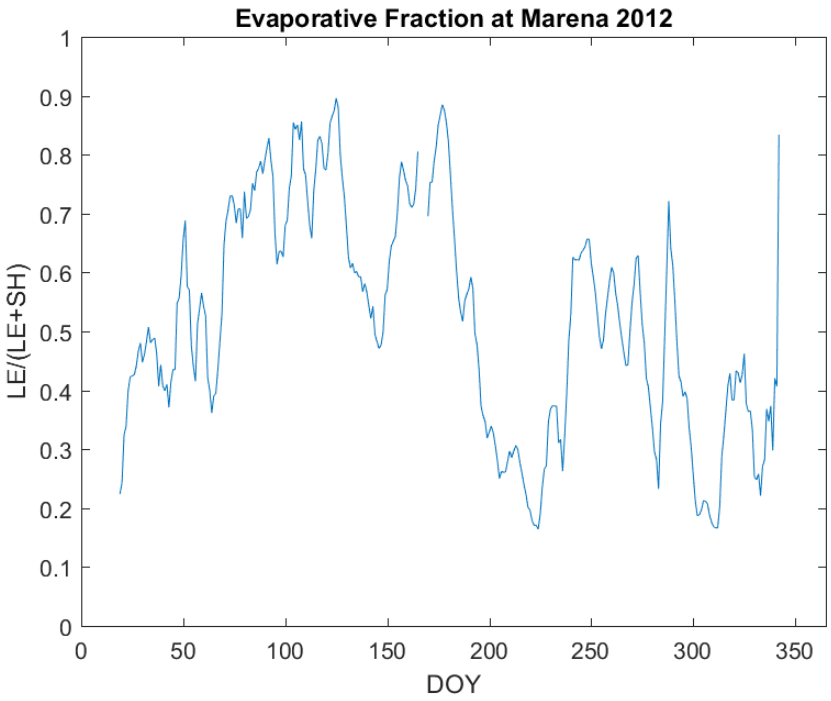

Figure 6.9: Evaporative fraction computed using flux tower data at Marena 2012.

6.2 BESS Performance for Flash Drought

BESS was used to determine whether flash drought can be identified on an at-site scale. Similar to Otkin et al. (2013a,b) a drought index (evaporative stress) was computed using the ratio of estimated ET to potential ET calculated from the Penman-Monteith equation.

6.2.1 ET Evaluation

Because BESS yield favorable results over the SGP and at the Marena site (R^2 = 0.64) and ET observations at the Marena site were limited in temporal scope, an annual time series average of ET was created using BESS (Figure 6.10). This average ET was compared to the ET measured by the flux tower. Up until DOY 120 (May 1) BESS agreed well with the in-situ observations. However, between DOY 120 and 175 (mid June) a large discrepancy between the magnitudes of BESS and observations of ET

were observed; BESS estimated near-normal ET rates for the first dry period, but observed ET rates were 0.5-1 mm/day below normal. Even so, the variability between BESS and flux measurements did correspond well. It was not until after the rainy period that BESS and observations agreed again. Once that flash drought began, the flux observations fell to approximately 3 mm/day below average. BESS was able to capture the same trend but missed the magnitude by approximately 1 mm/day. Once the ET rates returned to near normal values (i.e., DOY 250) BESS and the flux measurements agreed again in magnitude and variability around DOY 250 when.

It is worth noting that Marena had an EBC value of 60%, and thus, the magnitude of the difference may not be as substantial as it appears. However, BESS and the observations agree fairly well for the period spanning 2013-2015 (Fig. 6.11). During dramatic fluctuations in ET, it appears BESS becomes more erroneous. For example, in 2014 around DOY 130, a large decrease in ET rates occurred that differs significantly from BESS. This again occurred near the end of the year in 2015. These discrepancies could be due to the fact that flash drought occurs on a small temporal scale and BESS uses data from MODIS that is collected every 8 days.

Another source of error is likely from BESS not replicating the soil moisture very well. BESS uses a soil moisture scheme that relates soil moisture to the adjacent atmospheric moisture (Fisher et al. 2008). Essentially, the assumption is that the atmospheric moisture and soil moisture are in equilibrium. When considering large spatial and temporal scales this is usually the case. However, for flash drought in 2012, this was not the case. During the first dry period when shallow layer soil moisture was depleted the atmosphere was still moist despite a lack of precipitation (Fig. 6.12). This

period was not simulated well by BESS because the soil moisture and atmospheric moisture were not in equilibrium. On the contrary, BESS was able to depict ET better during the second dry period because the soil moisture and atmospheric moisture were in equilibrium.

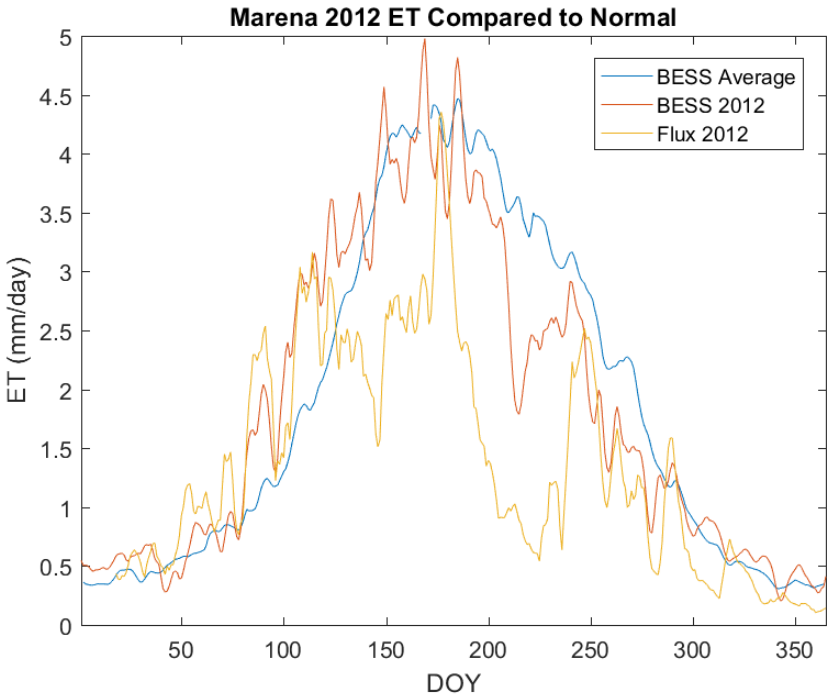

Figure 6.10: BESS ET compared to flux tower ET at Marena 2012. BESS average ET is the average ET from 2000-2015 computed by BESS.

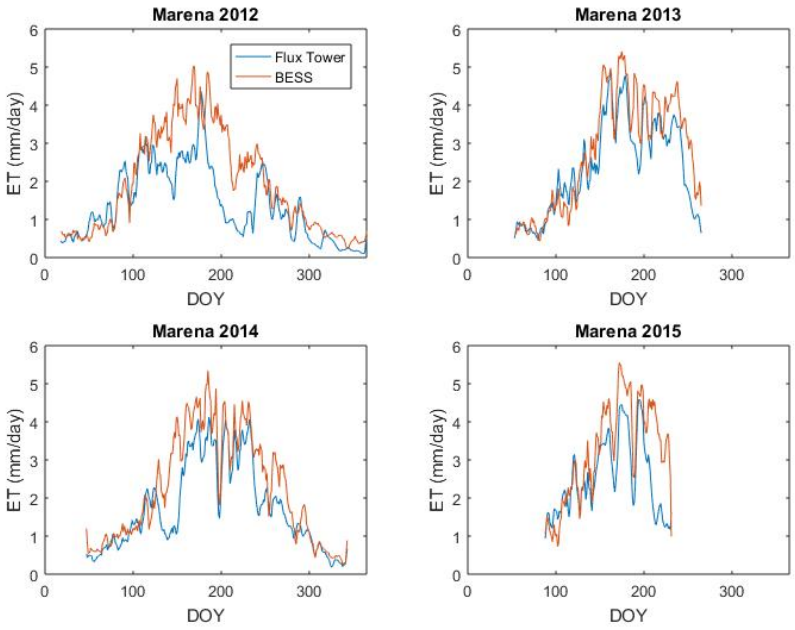

Figure 6.11: BESS ET compared to flux tower ET at Marena 2012-2015.

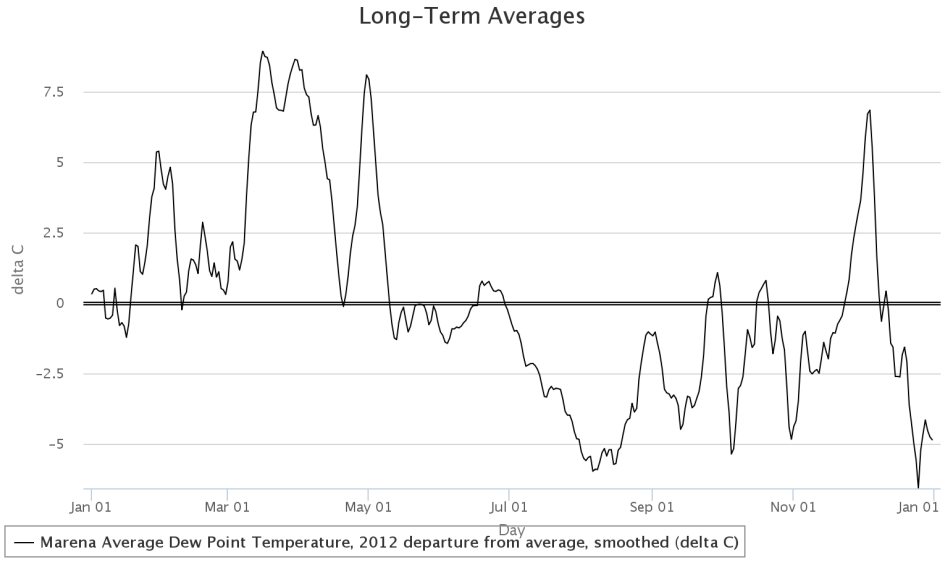

Figure 6.12: Marena 2012 Mesonet dew point departures.

6.2.2 Using BESS to Compute Evaporative Stress

The Evaporative Stress Index (ESI) defined by Otkin et al. (2013a,b) can be used with BESS modeled ET in the numerator as opposed to the modeled ET from their study (Fig. 6.13). This is an indicator of how moist or dry the soils are because potential ET is the amount of ET the system would produce under saturated conditions. When compared to actual ET, it can be used to determine how much relative moisture is in the system. When this ratio is >0.75 it indicates unusually wet warm-season conditions (Changnon et al. 2002). This occurrence is much more frequent in the eastern portion of the SGP, whereas the western portion of the SGP experiences 1/5 the occurrences (Changnon et al. 2002). For instance, during a pluvial year such as 2007, the ESI shows very high values indicating wet conditions. Conversely, during 2011 low values indicate that drought conditions were present. Of course, this index is not useful if the ET cannot be estimated correctly. For example, during the 2012 flash drought case ESI values were not indicative of dry conditions during the first dry period, but low ESI values were detected during the second dry period (Fig. 6.14).

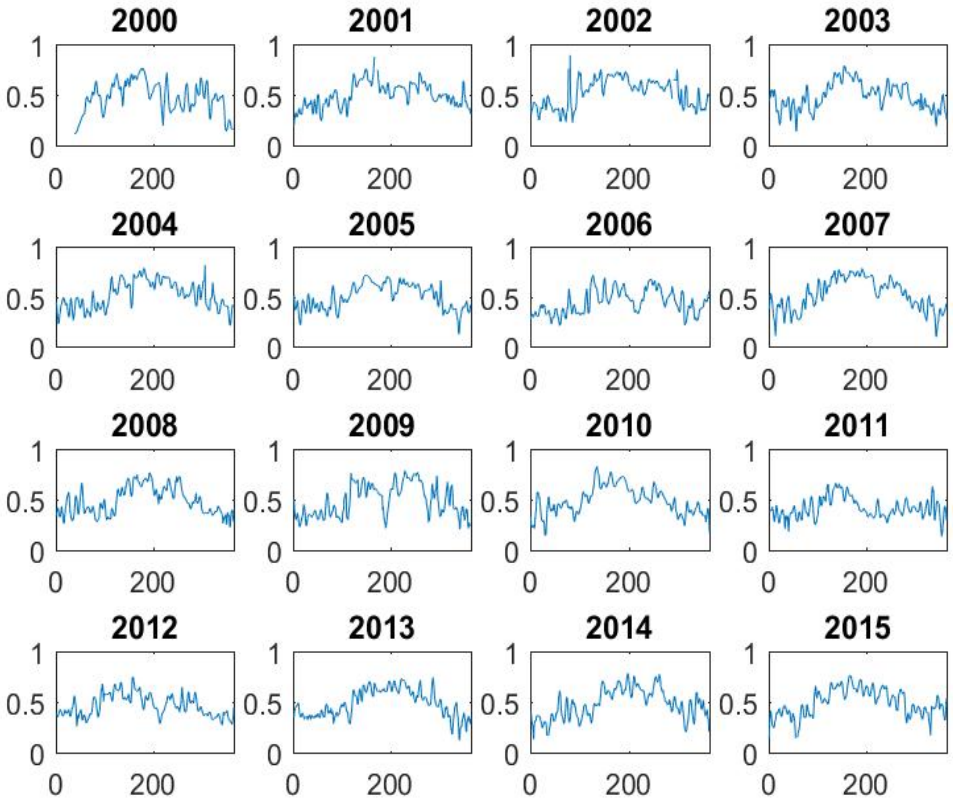

Figure 6.13: BESS evaporative stress index for Marena 2000-2015 with the y-axes being actual ET/potential ET and the x-axes being doy.

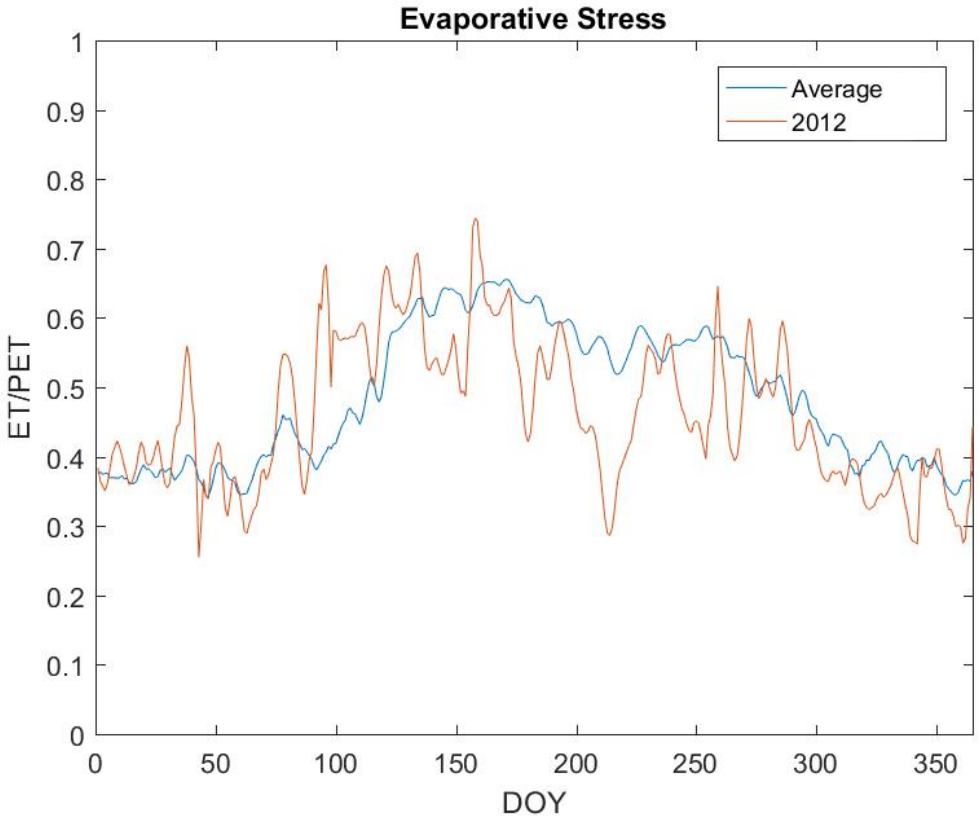

Figure 6.14: Evaporative stress index calculated by BESS for Marena Average (2000-2015) and Marena 2012.

Thus, BESS may have difficulty detecting flash drought and onset of flash drought conditions because flash drought develops on short temporal scales and BESS is forced with MODIS data that is collected on 8-day intervals. Further, BESS also yields errors when soil moisture and atmospheric moisture are out of phase. However, BESS has the ability to depict drought and pluvial conditions on larger time scales.

Chapter 7 : Conclusions

After extensive analysis of ET over the SGP, this study produced a greater understanding of the surface energy budget, diurnal and annual patterns of ET, and implications of ET on the water budget. The data collected from four flux tower sites in central Oklahoma was quality-controlled with research quality energy balance closure. Findings from this dataset include:

- Net radiation was partitioned more for sensible heating and latent heating in the dormant and growing season, respectively (except for the 2012 drought year when sensible heating was the dominant term for July and August), and ground heat flux was a relatively small term.
- Winter wheat had the largest diurnal cycle of ET in April and May due to an earlier growing season, whereas grasslands ET cycles peaked in June and July (except for the 2012 drought year when it peaked in September).
- ET rates at ICOS peak at approximately 3 mm/day during the growing season, whereas the IGOS sites were near 6 mm/day and Marena was around 4 mm/day. The difference in these results are likely due to the differences in growing season for the winter wheat, but the Marena site is likely underestimated due to the higher closure.
- GPP during the growing season peaked at approximately 35 $gCm^{-2}day^{-1}$ at ICOS, 50-60 $gCm^{-2}day^{-1}$ at the IGOS sites, and 30-40 $gCm^{-2}day^{-1}$ at the Marena site.

After the analysis of ET was completed at the site scale, it was paramount to determine how ET varied across the entire SGP. Data collected from 16 flux towers

across the SGP were used to compare ET estimation techniques. It was found that BESS BESS performs better than TSEBS over the sites analyzed even though TSEBS is forced using Landsat data that has better spatial resolution (30 m vs. 1km) but less temporal resolution (16 days vs. 8 days). Further BESS performed better than the Wagle et al. (2017) model because of the inherent bias in the Wagle model from MODIS-derived PAR. BESS also performed better than the MODIS-derived ET. The results from BESS include:

- BESS derived 8-day ET agrees well with observed 8-day ET ($R^2 = 0.74$; RMSE = 0.79) with poorer daily estimations ($R^2 = 0.61$; RMSE = 1.1).
- BESS estimated ET better for grasslands ($R^2 = 0.76$; RMSE = 0.81) than winter wheat ($R^2 = 0.54$; RMSE = 0.73).
- A pseudo-climatology of ET was created for the period between 2000-2015, including yearly and monthly averages of ET.
- Annual ET ranges from 400 mm/year in the northwest SGP to 1000 mm/year in the southeast SGP.
- ET anomalies displayed negative anomalies in drought years (i.e., 2000 and 2011) and positive anomalies during pluvial years (i.e., 2007 and 2015).
- Annual ET is more variable in the southwest SGP (50-100 mm/year) and less variable in the northeast SGP (10-40 mm/year), although the ET variability at some sites was less accurate than at others.

The water budget in the SGP is also heavily influenced by ET. On average, 75% of the incoming precipitation into the SGP leaves the system via ET. This is probably slightly biased due to the large amounts of irrigation in the SGP. Because water that is

used from irrigation comes from ground storage, higher ET relative to precipitation will occur as a result of water being added to the basin.

One area of improvement for BESS is the soil evaporation term assumed to be in equilibrium with surface atmospheric moisture content. For example, the results demonstrated that during 2012, equilibrium was not achieved when drying soils were paired with moist atmospheric conditions that led to an overestimation of ET in BESS. However, BESS was able to depict drought and pluvial conditions for many years. When ESI falls below 0.5, drought conditions are likely occurring and when ESI is above 0.75 then pluvial conditions are likely occurring.

Future work is needed to improve ET estimations for the SGP as a whole including:

- More surface flux towers across Texas and the southeast SGP are needed to verify BESS (and similar methodologies) is those regions.
- More continuous annual datasets are vital for understanding interannual ET variability and the water budget more clearly. It would also be beneficial to perform the water budget regional analysis on smaller scales, such as individual climate divisions.
- Largely irrigated regions within the SGP may display higher ET rates than areas that are not irrigated. Therefore, it is necessary to perform pixel-to-pixel comparisons between irrigated and non-irrigated pixels in BESS to quantify these differences.
- Different seasons have different ET characteristics, and as such, it is imperative to conduct these same studies on seasonal time scales that can compliment the monthly and annual evaluations.

- BESS also estimates GPP; a similar analysis needs to be completed over the SGP for GPP to determine BESS's accuracy and quantify GPP at different timescales.

Overall, ET across the SGP is highly variable compared to other parts of the world because of the highly variable climate that results in a wide range of interannual precipitation and temperature. Because this region of the United States contributes heavily to the agriculture and livestock industry it is important to focus efforts to create an observation network that allows for complete understanding of the dynamic water budget. These results are important in establishing this understanding for the SGP.

References

Allen, R. G., Walter, I. A., Elliott, R. A., Howell, T. A., Itenfisu, D., Jensen, M. J., & Snyder, R. L. (2005). ASCE standardized reference evapotranspiration equation. Baltimore, MD: Am. Soc. Civil Eng.

American Meteorological Society, cited 2012: Evapotranspiration. Glossary of Meteorology. [Available online at http://glossary.ametsoc.org/wiki/evapotranspiration].

Ameriflux Management Project, cited 2016. [accessed 2016 Jun 10]. http://www.ameriflux.lbl.gov.

Auble, D.L. and Meyers, T.P., 1992: An open path, fast response infrared absorption gas analyzer for H_2O and CO_2. Boundary Layer Meteorology, 59: 243-256.

Baldocchi, D., 2013: A Brief History on Eddy Covariance Flux Measurements: A Personal Perspective. FluxLetter, 5(2):1-8.

Burba, G., 2013: Eddy Covariance Method for Scientific, Industrial, Agriculture, and Regulatory Applications. LI-COR, 331 pp.

Businger, J.A., 1971: Flux profile relationships in the atmospheric surface layer. Journal of Atmospheric Science, 28: 181.

Changnon, S.A., Kunkel, K.E., Winstanley, D., 2002: Climate factors that caused the unique tall grass prairie in the central United States. Phys. Geogr., 23(4): 259-280.

Christian, J., K. Christian, and J.B. Basara, 2015: Drought and pluvial dipole events within the Great Plains of the United States. Journal of Applied Meteorology and Climatology, 54: 1886-1899.

Colaizzi, P.D., S.R. Evett, T.A. Howell, P.H. Gowda, S.A. O'Shaughnessy, J.A. Tolk, W.R. Kustas, and M.C. Anderson, 2012: Two source energy balance model-refinements and lysimeter tests in the Southern High Plains. Transactions of the ASABE, 55(2): 551-562.

Colaizzi, P.D., N. Agam, J.A. Told, S.R. Evett, T.A. Howell, S.A. O'Shaughnessy, P.H. Gowda, W.P. Kustas, and M.C. Anderson, 2016: Advances in the two-source energy model: Partitioning of evapotranspiration and transpiration for cotton. Transactions of the ASABE, 59(1): 181-197.

Cosh, M. H., T. E. Ochsner, L. McKee, J. Dong, J. B. Basara, S. R. Evett, C. E. Hatch, E. E. Small, S. C. Steele-Dunne, M. Zreda, and C. Sayde. 2016. The Soil Moisture Active Passive Marena, Oklahoma, In Situ Sensor Testbed (SMAP-MOISST): Testbed Design and Evaluation of In Situ Sensors. Vadose Zone J. 15. doi:10.2136/vzj2015.09.0122

Fischer, M.L., D.P. Billesbach, J.A. Berry, W.J. Riley, and Torn, M.S., 2007: Spatiotemporal variations in growing season exchanges of CO2, H2O, and sensible heat in agricultural fields of the Southern Great Plains. Earth Interactions, 11(17): 1-21.

Fisher, J.B., K.P. Tu, and D.D. Baldocchi (2008), Global estimates of the land-atmosphere water flux based on monthly AVHRR and ISLSCPII data, validated at 16 FLUXNET sites. Remote Sensing Environment, 112, 901-919.

Foken, T., 2006: 5o years of the Monin-Obukhov similarity theory. Boundary Layer Meteorology, 119 (3): 431-447.

Foken, T., 2008: The energy balance closure problem: an overview. Ecological Applicastion, 18 (6): 1351-1367.

Foken, T., M. Aubinet, J.J. Finnigan, M.Y. Leclerc, M. Mauder, and K.T. Paw U, 2011: Results of a panel discussion about the energy balance closure correction for trace gases. American Meteorogical Society. Doi: 10.1175/2011BAMS3130.I

Ford CR, Hubbard RM, Kloeppel BD, Vose JM, 2007: A comparison of sap flux-based evapotranspiration estimates with catchment-scale water balance. Agriculture and Forest Meteorology 145: 176-185.

Gash, J.H.C. et al. 1997: The variability of evaporation during the HAPEX Sahel intensive observation period. Journal of Hydrology, 189(1-4): 385-399.

Gowda, P., Paul, G., Marek, T., Basara, J., Steiner, J.L., Xiao, X., Zhou, Y. 2016. Daily time series evapotranspiration maps for Oklahoma and Texas panhandle. Pp. 28-33. In: R.W. Todd and A. Campbell (Eds). Proceedings-Great Plains Grazing Field Research Symposium, 14 June 2016, Oklahoma State University, Stillwater, OK.Available at: https://drive.google.com/file/d/0B5YS3Y9RTDyiQV9IUURWY2NNNW8/view?pref=2&pli=1.

Gowda, P.H., T.A. Howell, G. Paul, P.D. Colaizzi, T.H. Marek, B. Su, Copeland, K.S., 2013: Deriving hourly evapotranspiration rates with SEBS: A lysimetric evaluation. Vadose Zone Journal. Doi:10.2136/vzj2012.0110.

Hasler, N., and R. Avissar, 2007: What controls evapotranspiration in the Amazon Basin?, J. Hydrometeorol., 8(3), 380-395, doi:10.1175/JHM587.1.

Hess, G.D., Hicks, B.B. and Yamada, T., 1981: The impact of the Wangara Experiment. Boundary Layer Meteorology, 20(2): 135-174.

Hyson, P. and Hicks, B.B., 1975: Single-beam infrared hygrometer for evaporation measurement. Journal of Applied Meteorology, 14(3): 301-307.

Karl, T.R., J.M. Melillo, and T.C. Peterson, 2009: Global Climate Change Impacts in the United States. Cambridge University Press, 180 pp.

Knapp, A.K., P.A. Fay, J.M. Blair, S.L. Collins, M.D. Smith, J.D. Carlisle, C.W. Harper, B.T. Danner, M.S. Lett, and J.K. McCarron, 2002: Rainfall variability, carbon cycling, and plant species diversity in a mesic grassland. Science, 298(5601): 2202-2205.

Leclerc, M.Y. and Thurtell, G.W., 1990: Footprint prediction of scalar fluxes using a Markovian analysis. Boundary Layers Meteorology, 52: 247-258, 1990.

Ma, W., Y. Ma, Z. Hu, Z. Su, J. Wang, and H. Ishikawa, 2011: Estimating surface fluxes over middle and upper streams of the Heigh River Basin with ASTER imagery. Hydrology Earth System Science, 15: 1403-1413.

Marc, V., and M. Robinson, 2007: The long-term water balance (1972-2004) of upland forestry and grassland at Plynlimon, mid-Wales. Hydrological Earth System Science, 11(1): 44-60.

McCabe, M.F., Y.Y. Liu, R. Vinukollu, H. Su, J.P. Evans, and E.F. Wood, 2009: Comparison of latent heat flux estimates over Australia. Paper presented at: 18th World IMACS/MODSIM Congress, Cairns, Australia. 13-17 July 2009.

McPherson, R. A. and D.J. Stensrud, 2004: Influences of a winter wheat belt on the evolution of the boundary layer. Monthly Weather Review, 133: 2178-2199.

Mo, K.C. and D.P. Lettenmaier, 2015: Heat wave flash droughts in decline. Geophys. Res. Lett., 42: 2823-2829. Doi: 10.1002/2015GL064018.

Mo, K.C. and D.P. Lettenmaier, 2016: Precipitation deficit flash droughts over the United States. Journal of Hydrometeorology, 17: 1169-1184. Doi: 10.1175/JHM-D-15-0158.1.

Monteith, J.L., 1965: Evaporation and environment. The state and movement of water in living organisms, in Symposium of the Society of Experimental Biology, edited by G.E. Fogg, pp. 205-234, Cambridge Univ. Press, Cambridge, U.K.

National Center for Atmospheric Research Staff (NCAR) (Eds). Last modified 23 Dec 2015. "The Climate Data Guide: PRISM High-Resolution Spatial Climate Data for the United States: Max/min temp, dewpoint, precipitation." https://climatedataguide.ucar.edu/climate-data/prism-high-resolution-spatial-climate-data-united-states-maxmin-temp-dewpoint.

Norman, J.M., Kustas, W.P., and K.S. Humes, 1995: A two-source approach for estimating soil and vegetation energy fluxes from observations of directional radiometric surface temperature. Agriculture and Forest Meteorology, 77: 263-293.

Ohtoki, E. and Matsui, T., 1982: Infrared device for simultaneous measurement of fluctuations of atmospheric carbon-dioxide and water-vapor. Boundary Layer Meteorology, 24(1): 109-119.

Otkin, J.A., M.C. Anderson, C. Hain, I.E. Mladenova, J.B. Basara, and M. Svoboda, 2013a: Examining rapid onset drought development using the thermal infrared-based evaporative stress index. American Meteorological Society, 14: 1057-1074. Doi: 10.1175/JHM-D-12-0144.1.

Otkin, J.A., M.C. Anderson, C. Hain, and M. Svoboda, 2013b: Examining the relationship between drought development and rapid changes in the evaporative stress index. American Meteorological Society, 15: 938-956. Doi: 10.1175/JHM-D-13-0110.1.

Paul, G., P.H. Gowda, P.V. Varaprasad, T.A. Howell, and S.A. Staggenbord, 2011: Evaluating surface energy balance system using aircraft data. In: Bearing knowledgy for sustainability. Proceedings of the 2011 World Environmental and Water Resources Congress, Palm Springs, CA. 22-26 May 2011. American Meteolological Society of Civil Engineering, Reston, VA. p. 2777-2786.

Pielke, R.A., Avissar, R., Raupach, M., Dolman, A.J., Zeng, X., A.S. Denning, 1998: Interactions between the atmosphere and terrestrial ecosystems: influence on weather and climate. Global Change Biology, 4: 461-475.

Pruitt, W.O., Morgan, D.L. and Lourence, F.J., 1973: Momentum and mass transfers in surface boundary-layer. Quarterly Journal of the Royal Meteorological Society, 99(420): 370-386.

Rebmann, C., M. Göchede, T. Foken, M. Aubiner, M. Aurela, P. Berbigier, C. Bernhofer, N. Buchmann, A. Carrara, A. Cescatti, R. Ceulemans, R. Clement, J. Elbers, A. Granier, T. Grünwald, D. Guyon, K. Havránková, B. Heinesch, A. Knohl, T. Laurila, B. Longdoz, B. Marcolla, T. Markkanen, F. Miglietta, J. Moncreiff, L. Montagnani, E. Moors, M. Nardino, J. Ourcival, S. Rambal, U. Rannik, E. Rotenburg, P. Sedlak, G. Unterhuber, T. Vesala, D. Yakir, 2005. Quality analysis applied on eddy covariance measurements at complex forest sites using footprint modeling. Theoretical and Applied Climatology, 80 (2-4): 121-141. DOI: 10.1007/s00704-004-0095.

Reynolds, O., 1895: On the dynamical theory of incompressible viscous fluids and the determination of the criterion. Philosophical Transactions of the Royal Society of London, A, 186: 123-164.

Ryu, Y., Baldocchi, D.D., Ma, S., and T. Hehn, 2008: Interannual variability of evapotranspiration and energy exchange over an annual grassland in California. Journal of Geophysical Research, 113: 1-16. DOI: 10.1029/2007JD009263.

Ryu, Y., D.D. Baldocchi, H. Kobayashi, C. van Ingen, J. Li, T.A. Black, J. Beringer, E. van Gorsel, A. Knohl, B. E. Law, and Roupsard, O., 2011: Integration of

MODIS land and atmosphere products with a coupled-process model to estimate gross primary productivity and evapotranspiration from 1 km to global scales. Global Biogeochemistry Cycles, 25, GB4017.

Ryu, Y., D.D. Baldocchi, T.A. Black, M. Detto, B.E. Law, R. Leuning, A. Miyata, M. Reichstein, R. Vargas, C. Ammann, J. Beringer, L.B. Flanagan, L. Gu, L.B. Hutley, J. Kim, H. McCaughey, E.J. Moors, S. Rambal, and Vesala, T., 2012: On the temporal upscaling of evapotranspiration from instantaneous remote sensing measurements to 8-day mean daily-sums. Agricultureal and Forest Meteorology, 152:212-222. DOI: 10.1016/j.agrformet.2011.09.010.

Jiang, C. and Ryu, Y., 2016: Multi-scale evalutation of global gross primary productivity and evapotranspiration products derived from Breathing Earth System Simulator (BESS). Remote Sensing Environment, 186:1-20. http://dx.doi.org/10.1016/j.rse.2016.08.030

Scrase, F.J., 1930: Some characteristics of eddy motion in the atmosphere. Geophysical Memoirs, #52, Meteorological Office. London, 56 pp.

Sellers, P.J. and Hall, F.G., 1992: Fife in 1992 results, scientific gains, and future-research directions. Journal of Geophysical Research-Atmospheres, 97(D17): 19091-19109.

Sellers, P.J. et al. 1995: Boreal ecosystem atmosphere (BOREAS): an overview and early results from the 1994 field year. Bulletin of the American Meteorological Society., 76:1549-1577.

Sellers, P.J., 1997: Boreas in 1997: Scientific results; experimental overview and future directions. Journal of Geophysical Research., 102: 28731-28770.

Sellers, W.D., 1965: Physical Climatology. University of Chicago Press, Chicago, IL, 272 pp.

Shuttleworth, W.J., Zreda, M., Zeng, X., Zweck, C., and Ferre, P.A., 2010: The COsmic-ray Soil Moisture Observing System (COSMOS): a non-invasive, intermediate scale soil moisture measurement network. Proceedings of the British Hydrological Society's Third International Symposium: 'Role of hydrology in managing consequences of a changing global environment', Newcastle University, 19-23 July 2010. ISBN: 1 903741 17 3.

Su, H., M.F. McCabe, E.F. Wood, Z. Su, and J.H. Prueger, 2005: Modeling evapotranspiration during SMACEX: Comparing two approaches for local- and regional-scale prediction. Journal of Hydrometeorology, 6(6): 910-922.

Su, Z., 2002: The surface energy balance system (SEBS) for estimation of turbulent fluxes. Hydrological Earth System Science, 6:85-99.

Svoboda, M., D. LeComte, M. Hayes, R. Heim, K. Gleason, J. Angel, B. Rippey, R. Tinker, M. Palecki, D. Stooksbury, D. Miskus, and Stephens, S., 2002: The drought monitor. Bull. Amer. Meteor. Soc, 83, 1181-1190.

Swinbank, W.C., 1951: The measurement of vertical transfer of heat and water vapor by eddies in the lower atmosphere. Journal of Meteorology, 8(3): 135-145.

Swinbank, W.C. and Dyer, A.J., 1967: An experimental study in micrometeorology. Quarterly Journal of the Royal Meteorological Society, 93(398): 494-&.

Tang, Q.H., S. Peterson, R.H. Cuenca, Y. Hagimoto, and Lettenmaier, D.P., 2009: Satellite-based near-real-time estimate of irrigated crop water consumption. J. Geophys. Res., 114, D05114.

Timmermans, J., C. van der Tol, A. Verhoef, W. Verhoef, Z. Su, M. van Helvoirt, and L. Wang, 2011: Quantifying the uncertainty in estimates of surface-atmosphere fluxes through joint evaluation of the SEBS and SCOPE models. Hydrological Earth System Science Discussion, 8:2861-2893.

Trenberth, K.E., Smith, L., Qian, T.T., Dai, A.G. Fasullo, J., 2007: Estimates of the global water budget and its annual cycle using observational and model data. J. Hydrometeorol. 8(4), 758-769.

Twine T.E., J.H. Prueger, T.P. Teyers, M.L. Wesley, P.J. Starks, J.M. Norman, W.P. Kustas, P.R. Houser, Cook, D.R., 2000: Correcting eddy-covariance flux underestimates over a grassland. Agricultural and Forest Meteorology 103: 279-300.

Twine, T.E., C.J. Kucharik, and Foley, A.J., 2004: Effects of land cover change on the energy and water balance of the Mississippi River basin. Journal of Hydrometerology, 5: 640-655.

United States Drought Monitor online. c2000-2016. Lincoln (NE): National Drought Mitigation Center; [accessed 2016 Oct 27]. http://droughtmonitor.unl.edu/.

United States Geological Survey online, 2016. Land cover data viewer; [accessed 2016 Nov 9]. http://gis1.usgs.gov/csas/gap/viewer/land_cover/Map.aspx.

Wagle, Pradeep and Kakani, V.G., 2012: Growing season variability in evapotranspiration, ecosystem water use efficiency, and energy partitioning in switchgrass. Ecohydrology. 7, 64-72.

Wagle, P., X. Xiao, P. Gowda, J. Basara, N. Brunsell, J. Steiner, and K.C. Anup, 2016: Analysis and estimation of tallgrass prairie evapotranspiration in the central United States.

Wan, Zhanming, Ke Zhang, Xianwu Xue, Zhen Hong, Yang Hong, Jonathan Gourley, 2015: Water Balance Based Actual Evapotranspiration Reconstruction from

Ground and Satellite Observations Over the Conterminous United States. Water Resources Research, 51: 6485-6499. Doi:10.1002/2015WR017311.

Wilson, Kell, A. Goldstein, E. Falge, M. Aubinet, D. Baldocchi, P. Berbigier, C. Bernhofer, R. Ceulemans, H. Dolman, C. Field, A. Grelle, A. Ibrom, B.E. Law, A. Kowalski, T. Meyers, J. Moncrieff, R. Monson, W. Oechel, J. Tenhunen, R. Valentini, Verman, S., 2002: Energy balance closure at FLUXNET sites. Agricultural and Forest Meteorology, 113:223-243.

Vinukollu, R.K., E.F. Wood, C.R. Ferguson, and J.B. Fisher, 2011: Global estimates of evapotranspiration for climate studies using multi-sensor remote sensing data: Evaluation of three process-based approaches, Remote Sensing Environment, 115:801-823.

Zilitinkevich, S.S. and Chalikov, D.V., 1968: On momentum heat and moisture exchange in process of interaction between atmosphere and underlying surface. Izvestiya Akademii Nauk Sssr Fizika Atmosfery I Okeana, 4(7): 765-&.

Appendix A: Energy Balance Closure

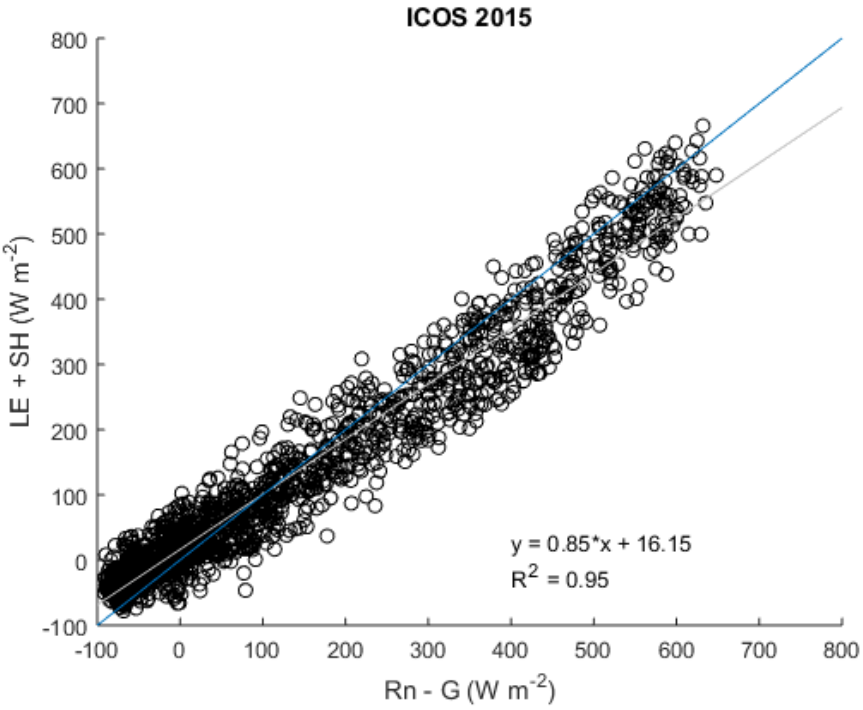

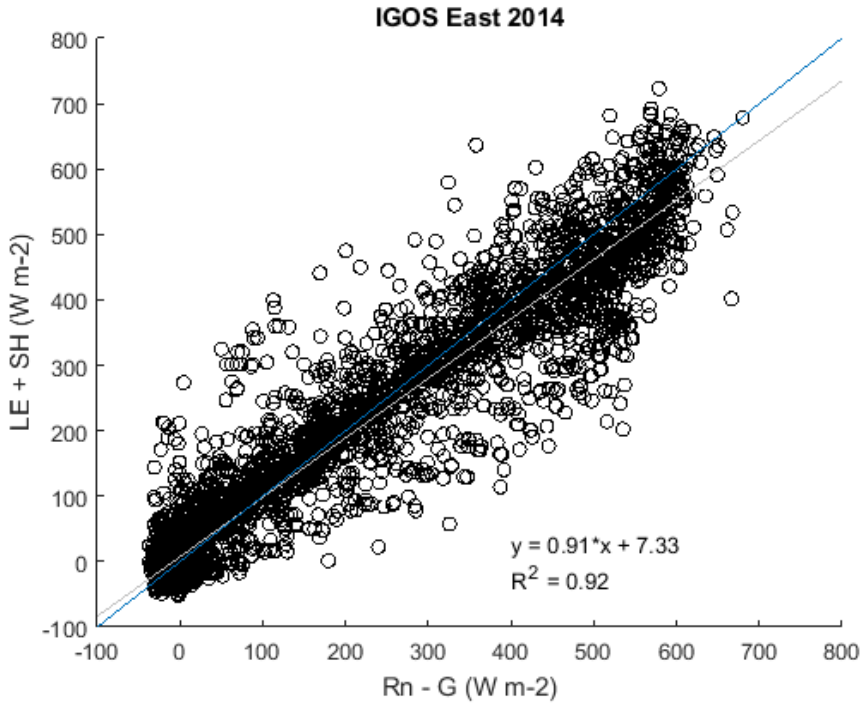

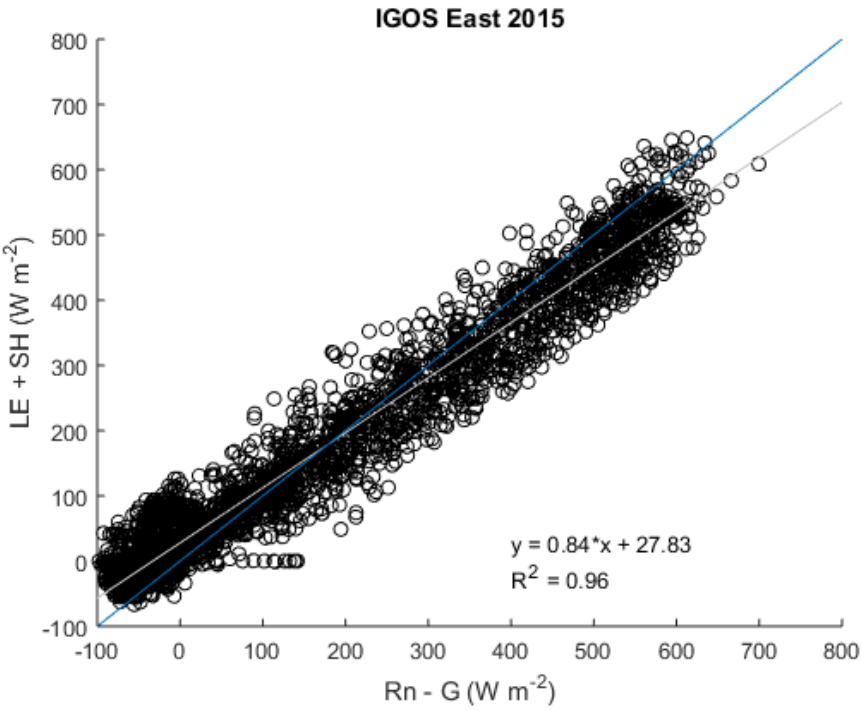
IGOS East 2015
LE + SH (W m-2)
Rn - G (W m-2)
y = 0.84*x + 27.83
R2 = 0.96

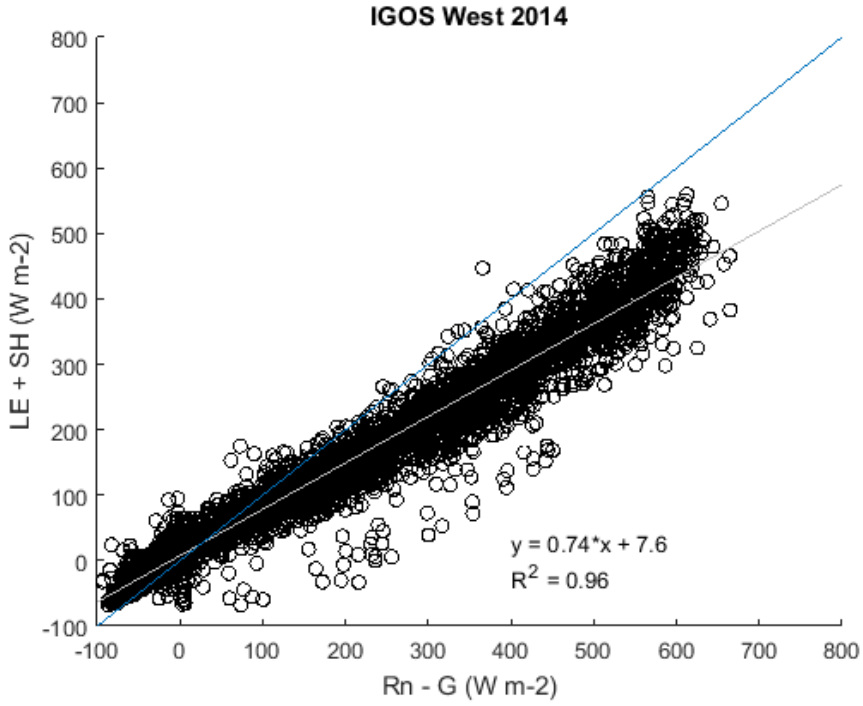
IGOS West 2014
LE + SH (W m-2)
Rn - G (W m-2)
y = 0.74*x + 7.6
R2 = 0.96

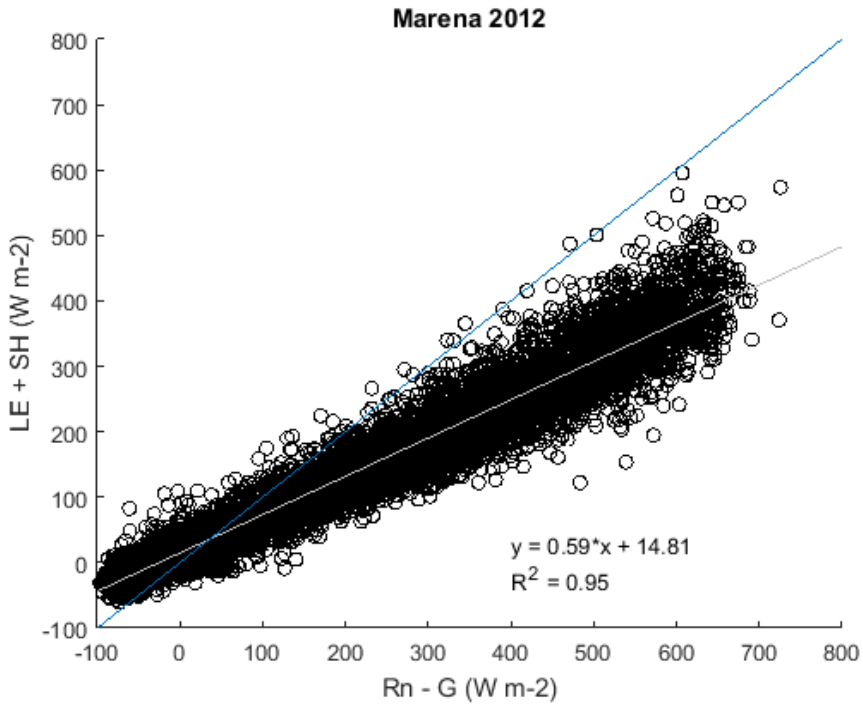
Marena 2012
LE + SH (W m-2)
Rn - G (W m-2)
y = 0.59*x + 14.81
R2 = 0.95
800
700
600
500
400
300
200
100
0
-100
-100
0
100
200
300
400
500
600
700
800

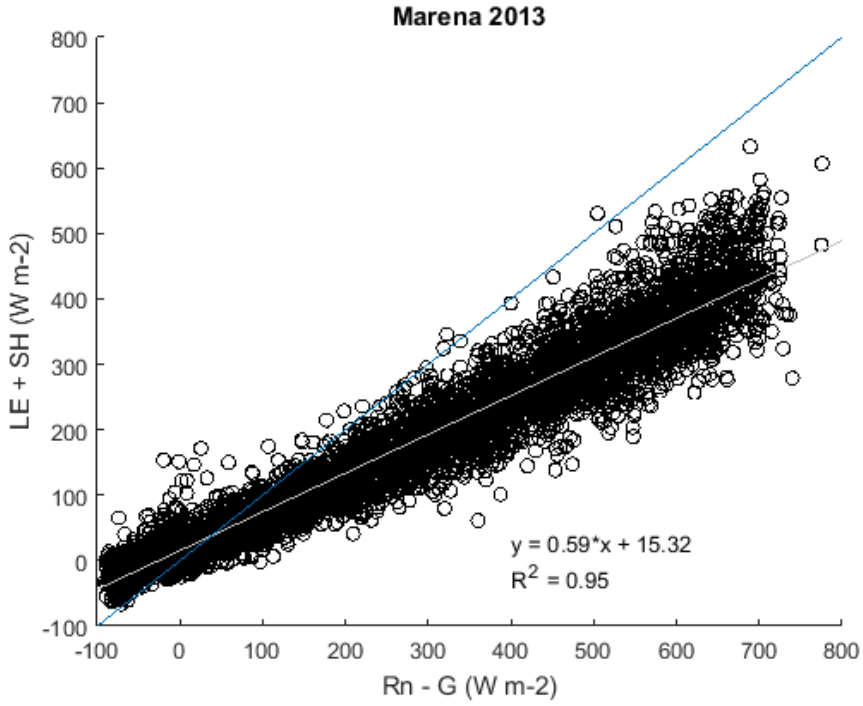
Marena 2013
LE + SH (W m-2)
Rn - G (W m-2)
y = 0.59*x + 15.32
R2 = 0.95
800
700
600
500
400
300
200
100
0
-100
-100
0
100
200
300
400
500
600
700
800

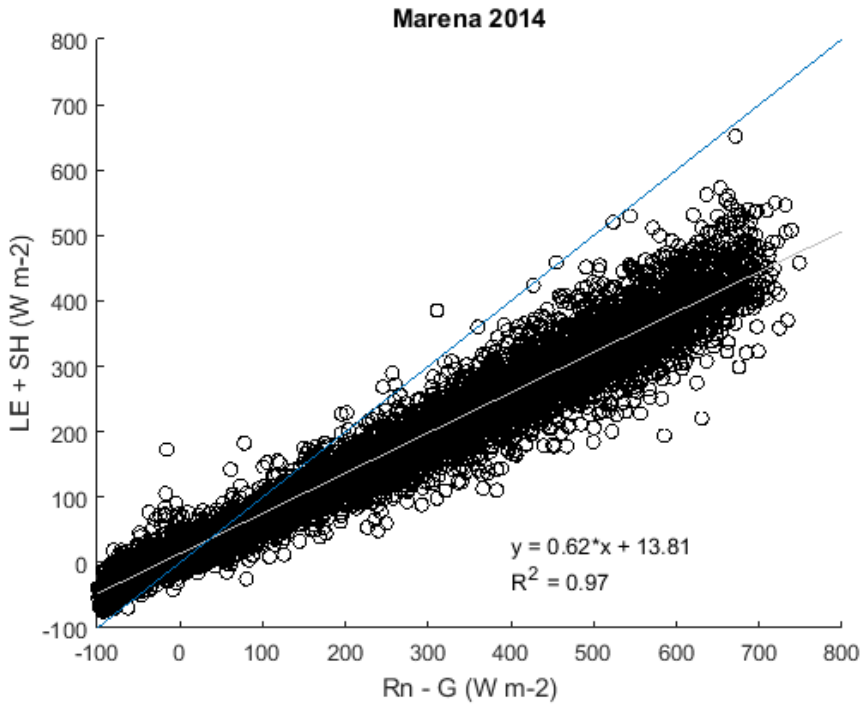
Marena 2014
LE + SH (W m-2)
Rn - G (W m-2)
y = 0.62*x + 13.81
R2 = 0.97
800
700
600
500
400
300
200
100
0
-100
-100
0
100
200
300
400
500
600
700
800

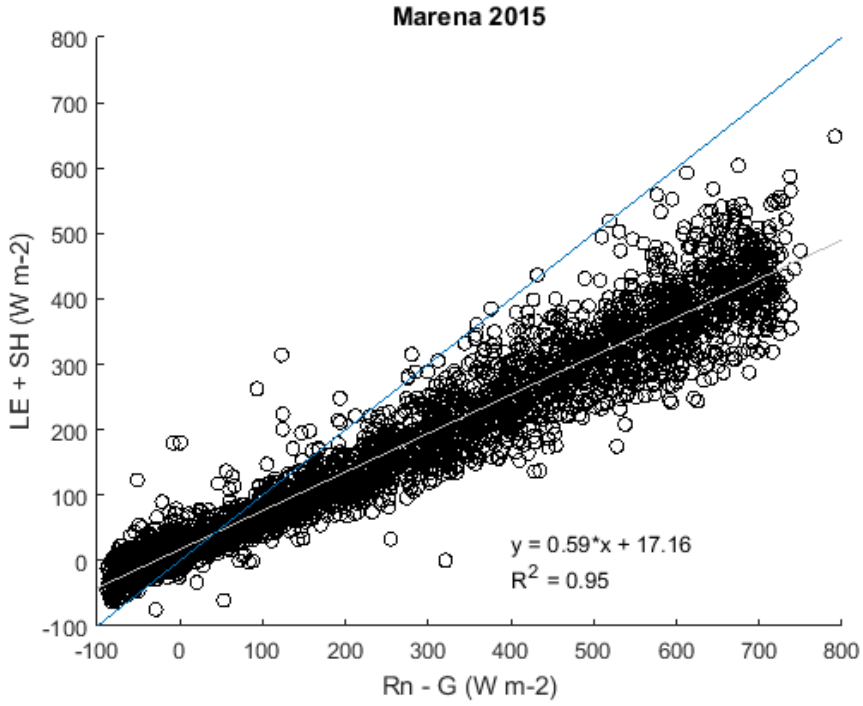
Marena 2015
LE + SH (W m-2)
Rn - G (W m-2)
y = 0.59*x + 17.16
R2 = 0.95
800
700
600
500
400
300
200
100
0
-100
-100
0
100
200
300
400
500
600
700
800

Appendix B: Site-by-Site Comparison

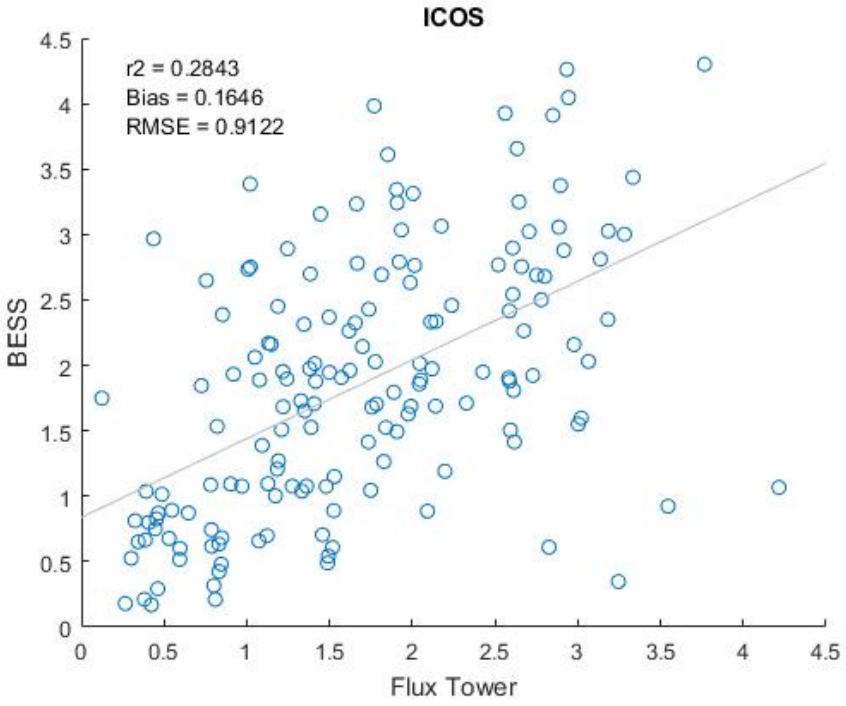

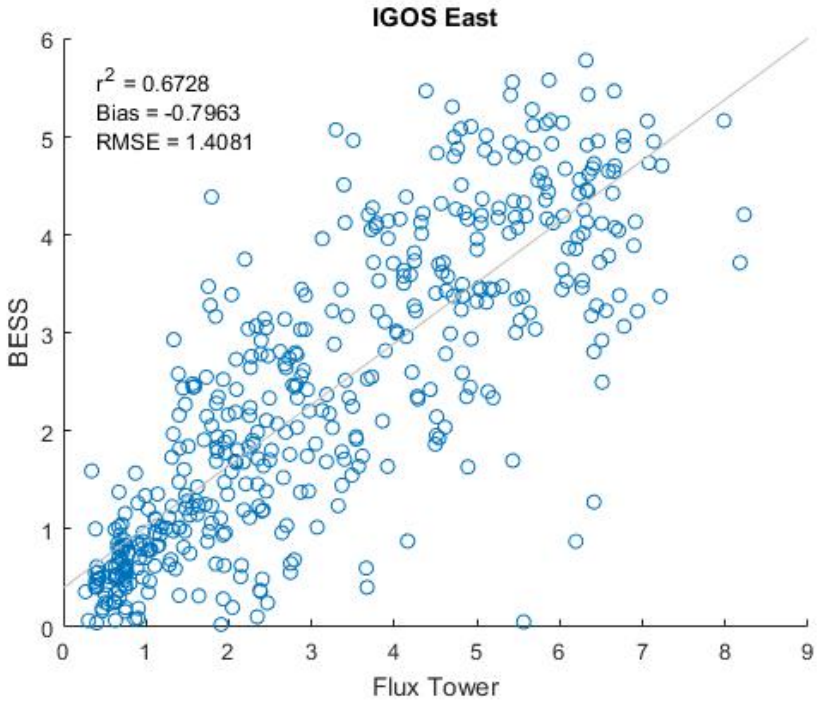

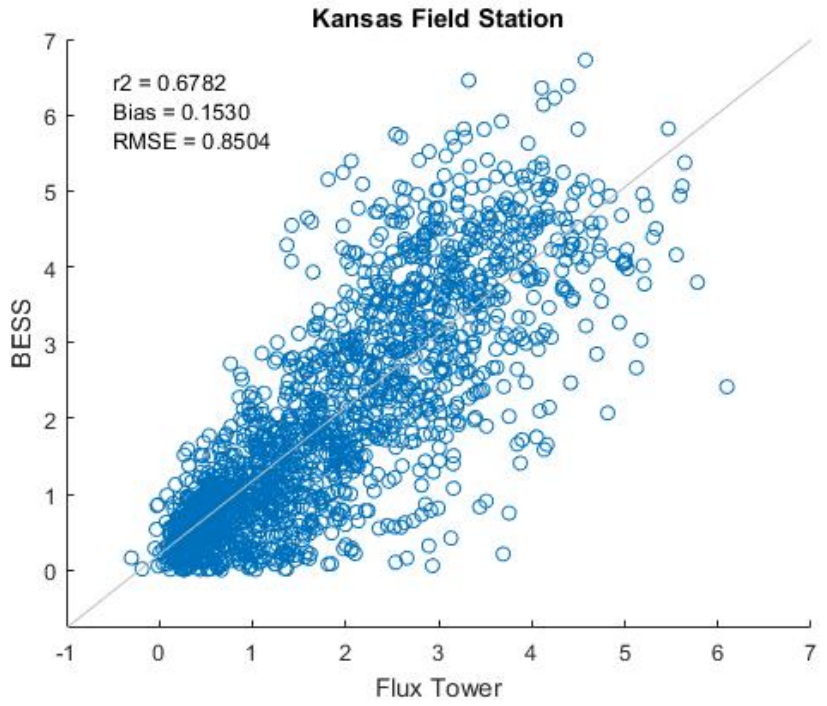
Kansas Field Station
r2 = 0.6782
Bias = 0.1530
RMSE = 0.8504
BESS
Flux Tower
7
6
5
4
3
2
1
0
-1
0
1
2
3
4
5
6
7

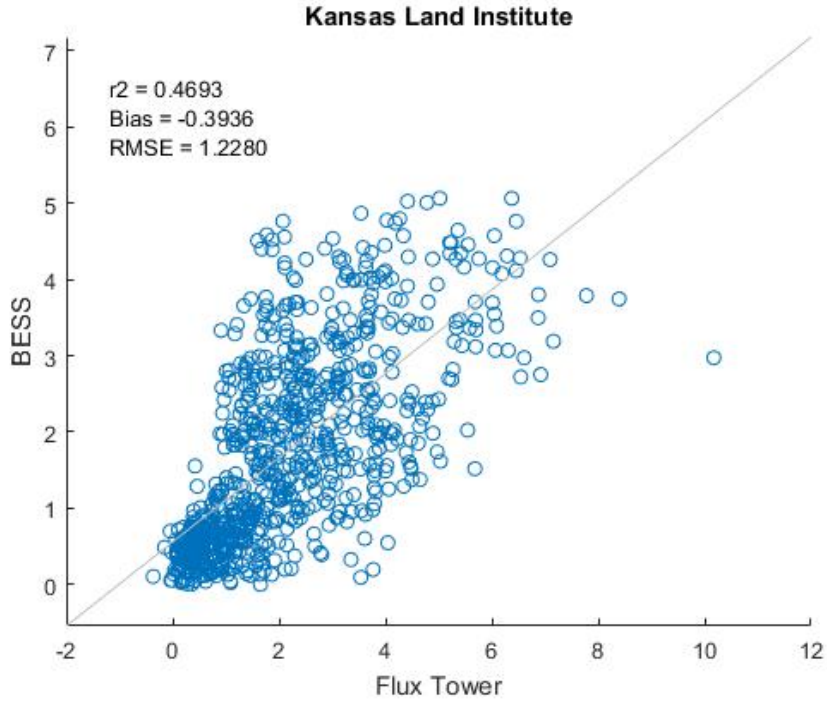
Kansas Land Institute
r2 = 0.4693
Bias = -0.3936
RMSE = 1.2280
BESS
Flux Tower
7
6
5
4
3
2
1
0
-2
0
2
4
6
8
10
12

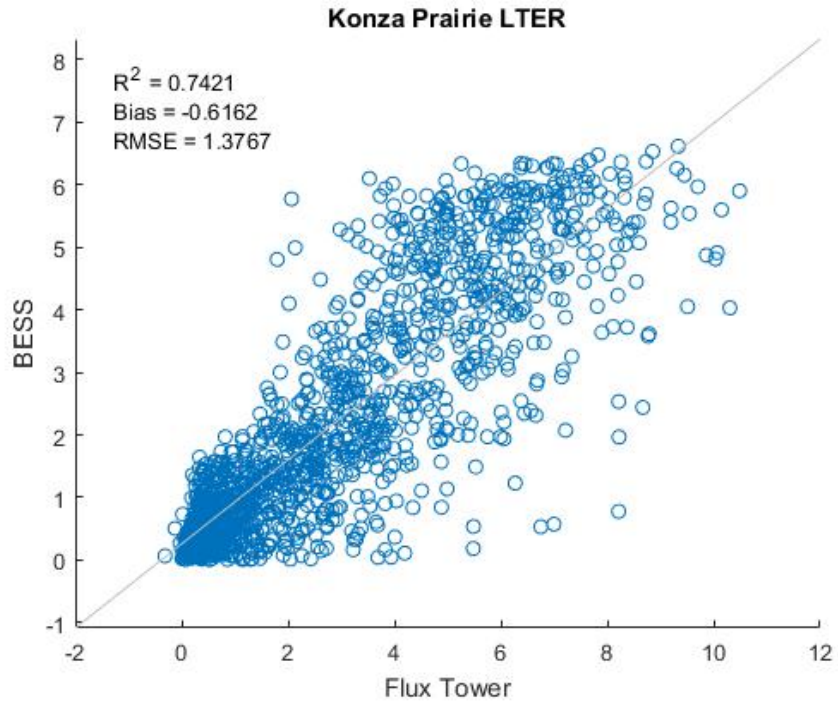
Konza Prairie LTER
R2 = 0.7421
Bias = -0.6162
RMSE = 1.3767
BESS
Flux Tower

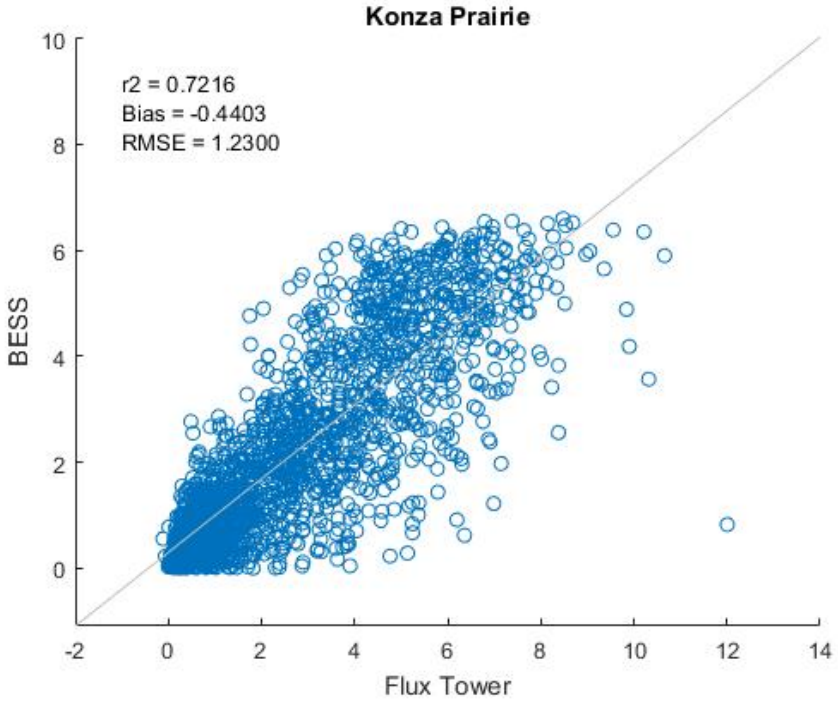
Konza Prairie
r2 = 0.7216
Bias = -0.4403
RMSE = 1.2300
BESS
Flux Tower

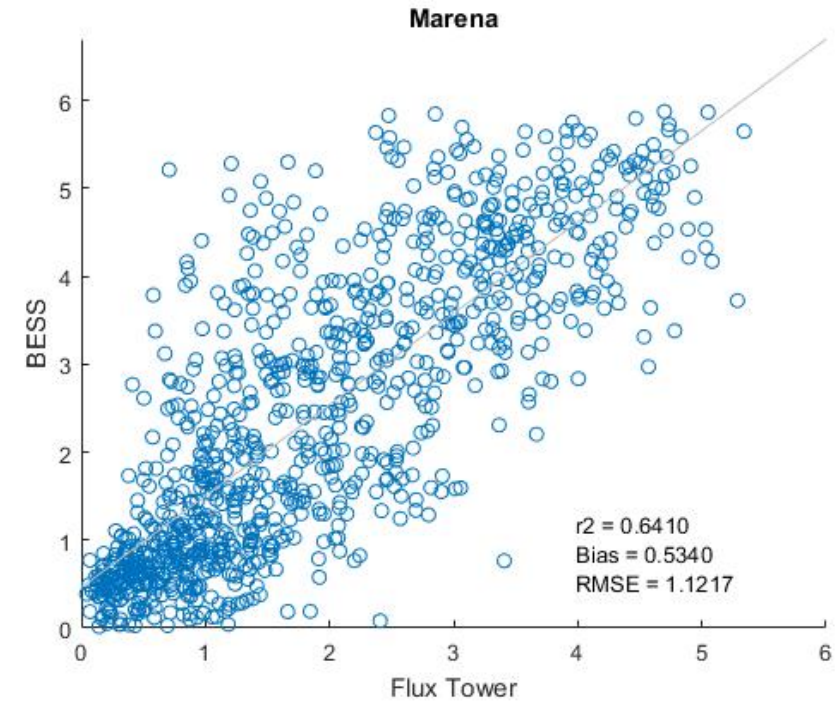
Marena
BESS
Flux Tower
r2 = 0.6410
Bias = 0.5340
RMSE = 1.1217
0
1
2
3
4
5
6

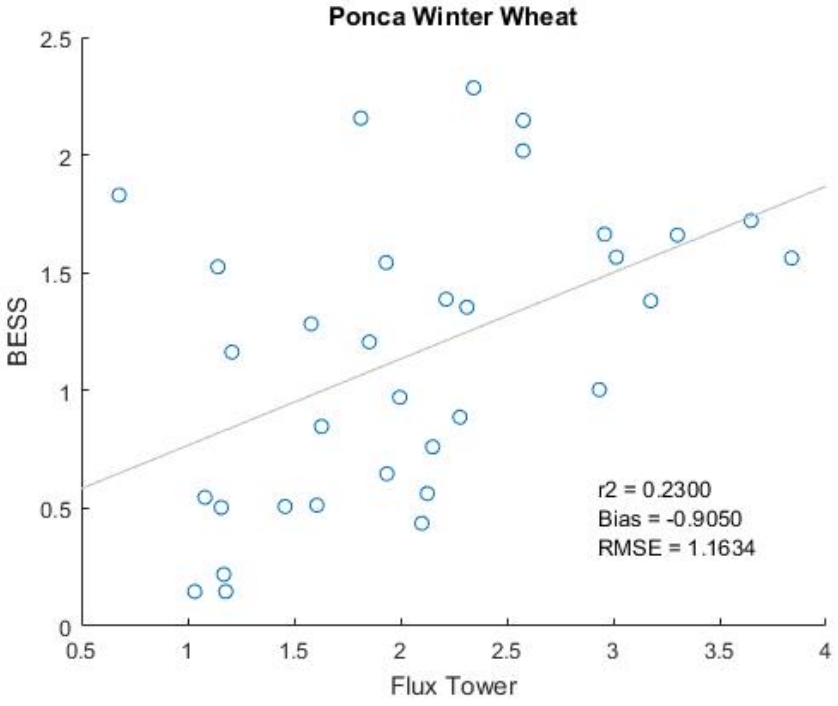
Ponca Winter Wheat
BESS
Flux Tower
r2 = 0.2300
Bias = -0.9050
RMSE = 1.1634
0
0.5
1
1.5
2
2.5
3
3.5
4

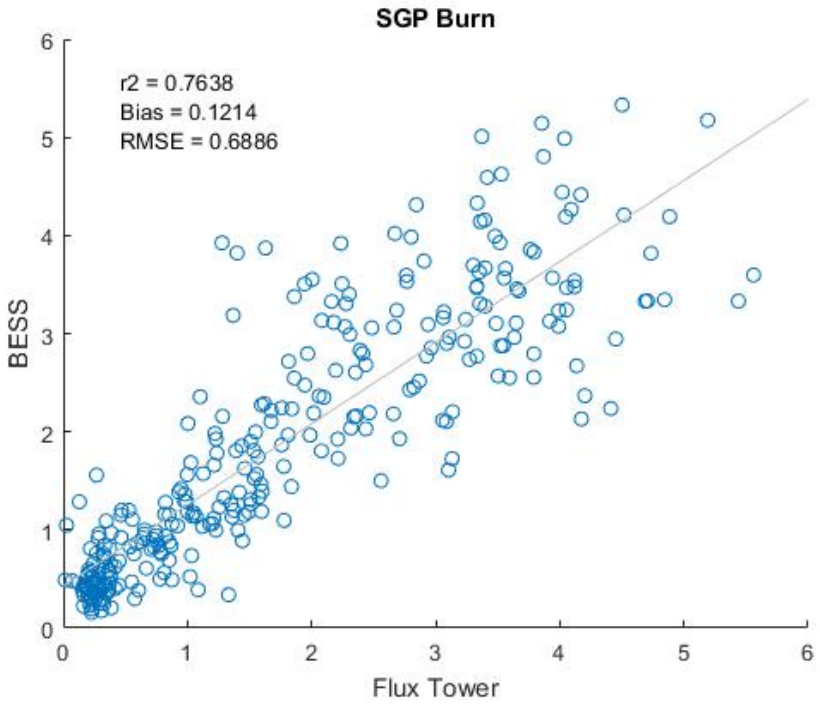
SGP Burn
r2 = 0.7638
Bias = 0.1214
RMSE = 0.6886
BESS
Flux Tower
0
1
2
3
4
5
6

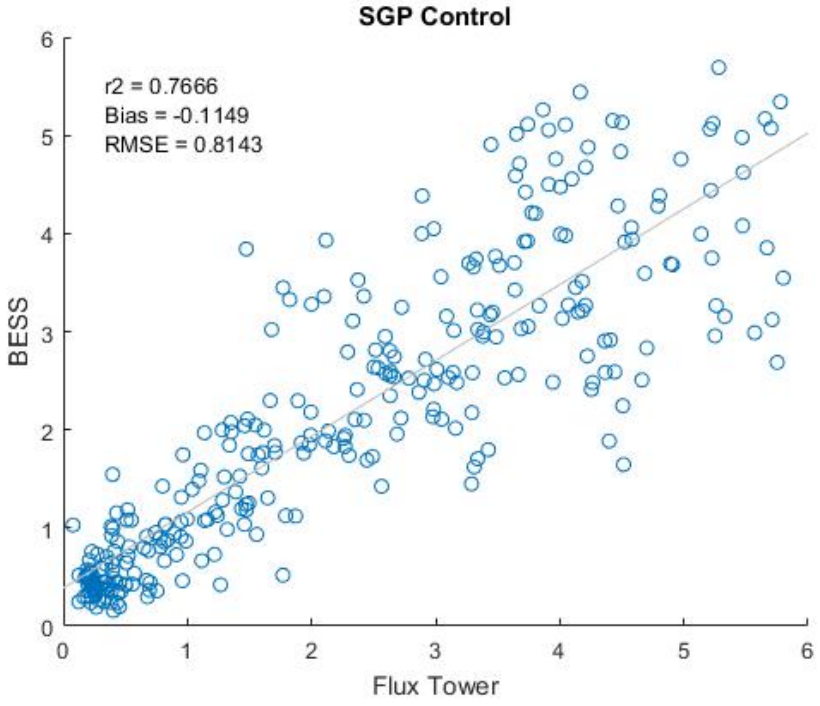
SGP Control
r2 = 0.7666
Bias = -0.1149
RMSE = 0.8143
BESS
Flux Tower
0
1
2
3
4
5
6

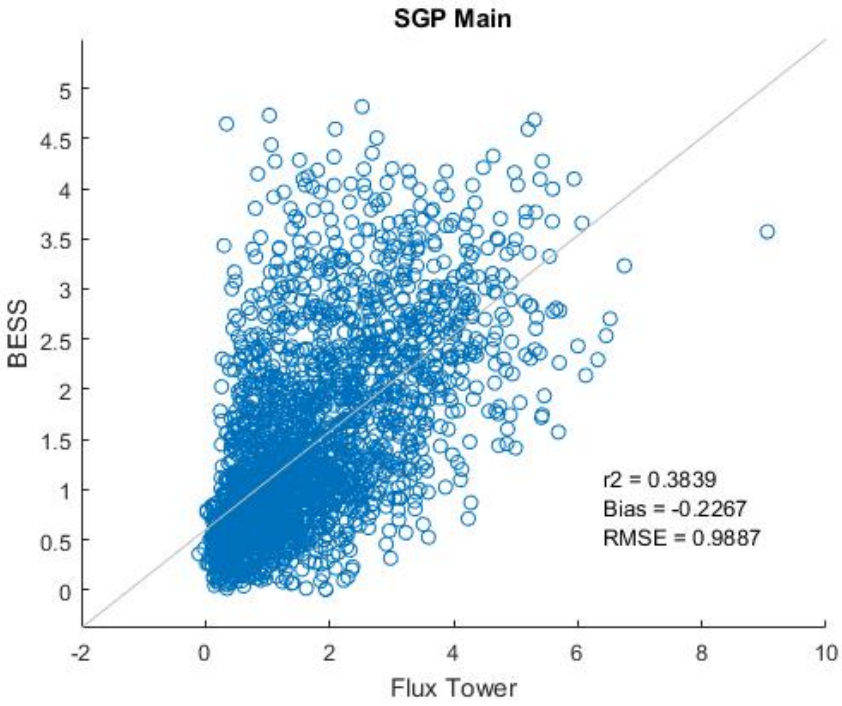
SGP Main
BESS
Flux Tower
r2 = 0.3839
Bias = -0.2267
RMSE = 0.9887

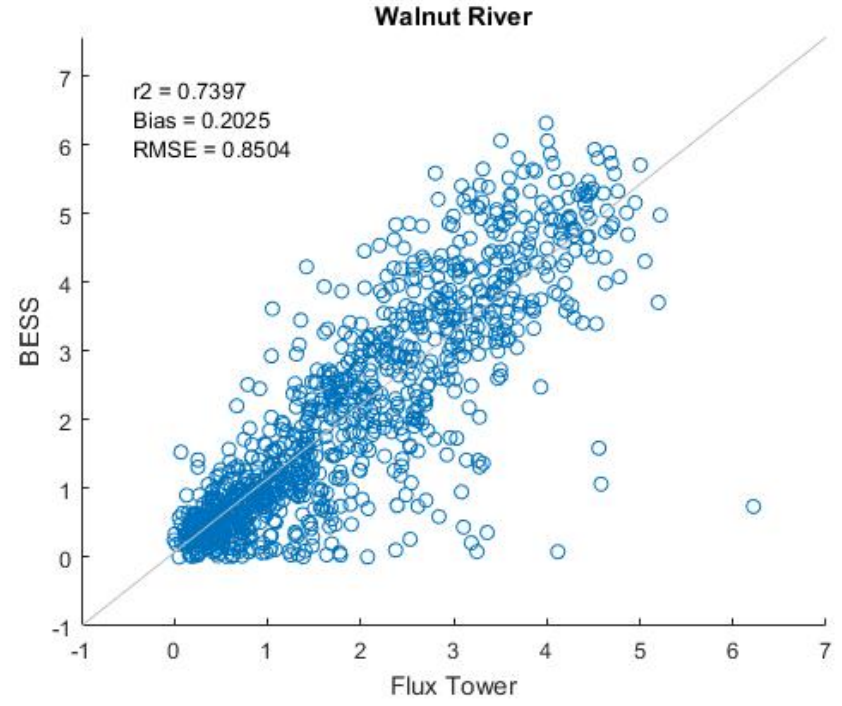
Walnut River
BESS
Flux Tower
r2 = 0.7397
Bias = 0.2025
RMSE = 0.8504

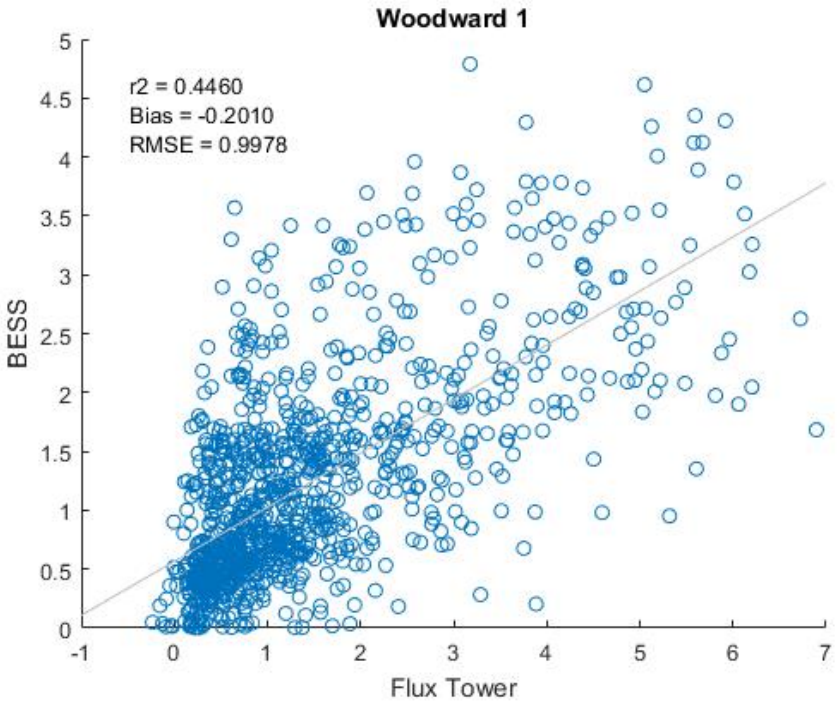
Woodward 1
r2 = 0.4460
Bias = -0.2010
RMSE = 0.9978
BESS
Flux Tower

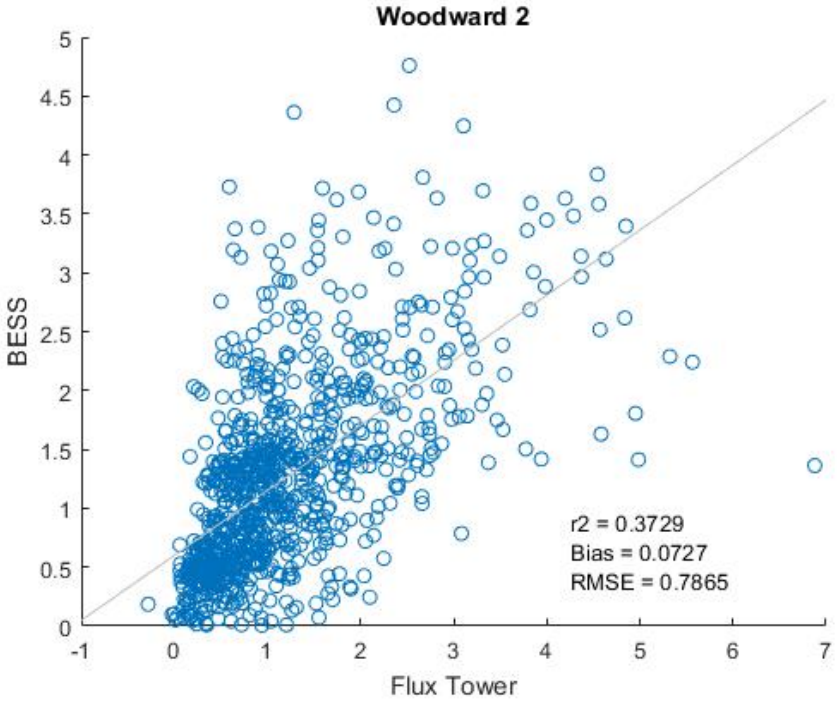
Woodward 2
r2 = 0.3729
Bias = 0.0727
RMSE = 0.7865
BESS
Flux Tower

Appendix C: Site-by-Site Time Series

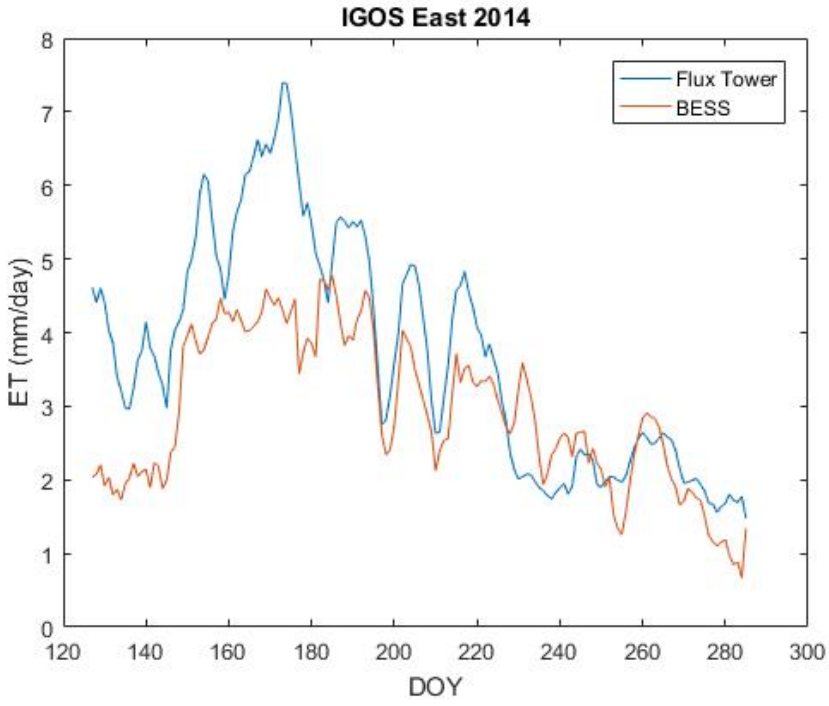

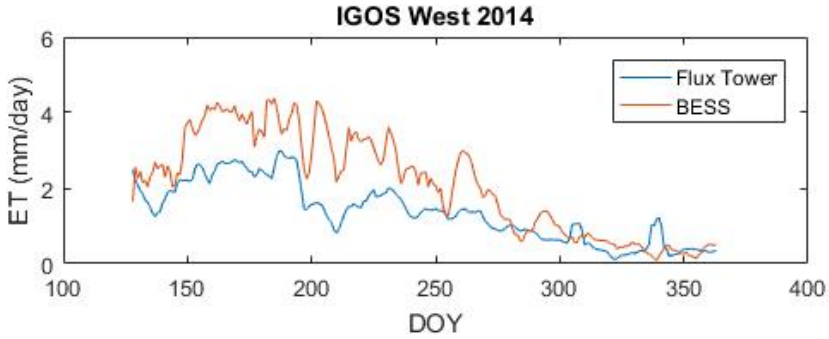

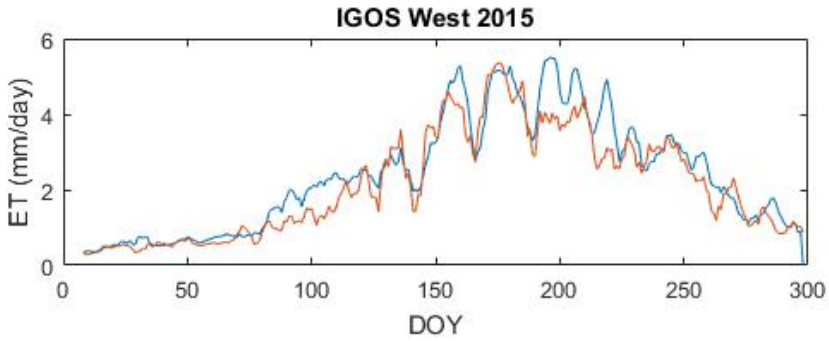

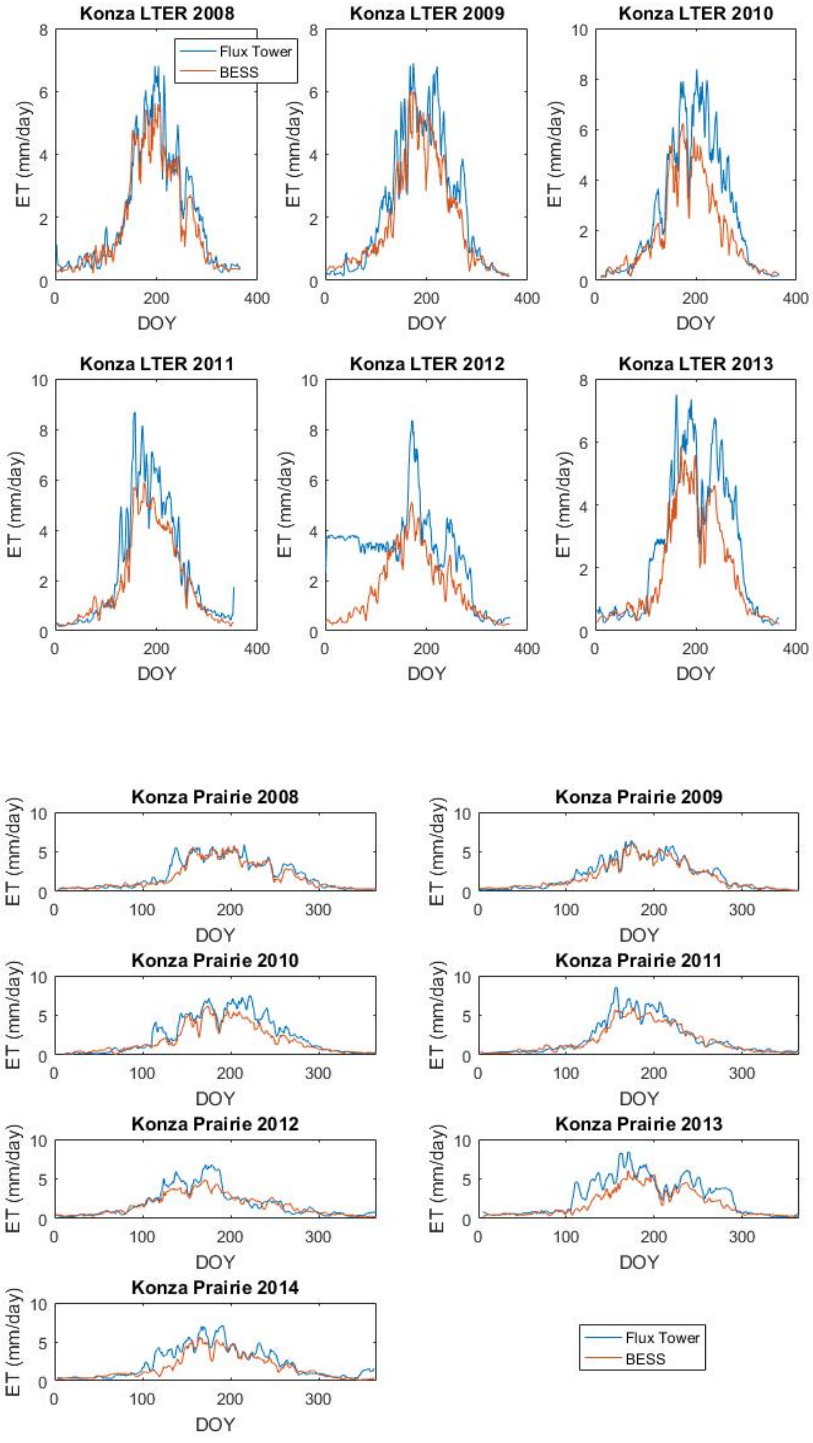
Konza LTER 2008
Konza LTER 2009
Konza LTER 2010
Konza LTER 2011
Konza LTER 2012
Konza LTER 2013
Flux Tower
BESS
ET (mm/day)
DOY
Konza Prairie 2008
Konza Prairie 2009
Konza Prairie 2010
Konza Prairie 2011
Konza Prairie 2012
Konza Prairie 2013
Konza Prairie 2014

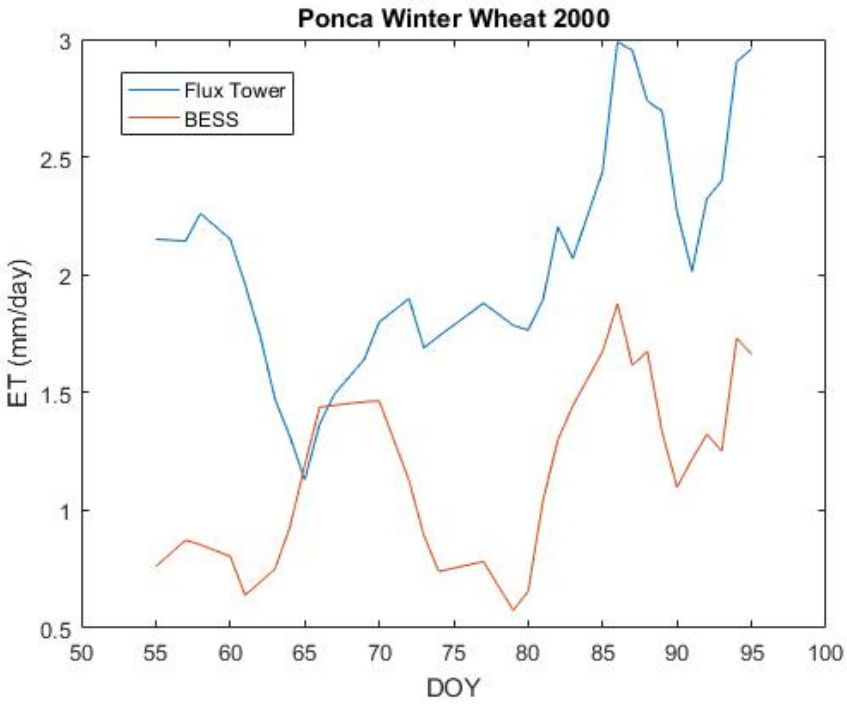
Ponca Winter Wheat 2000
Flux Tower
BESS
ET (mm/day)
DOY
3
2.5
2
1.5
1
0.5
50
55
60
65
70
75
80
85
90
95
100

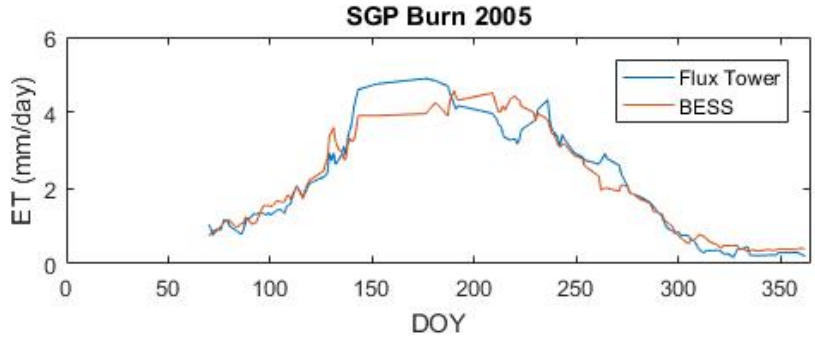
SGP Burn 2005
Flux Tower
BESS
ET (mm/day)
DOY
6
4
2
0
0
50
100
150
200
250
300
350

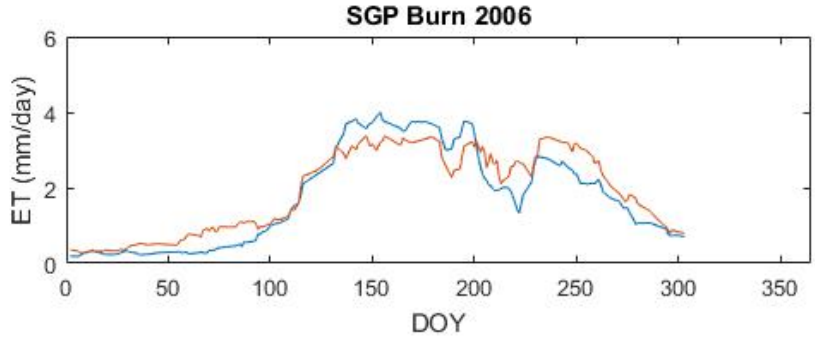
SGP Burn 2006
ET (mm/day)
DOY
6
4
2
0
0
50
100
150
200
250
300
350

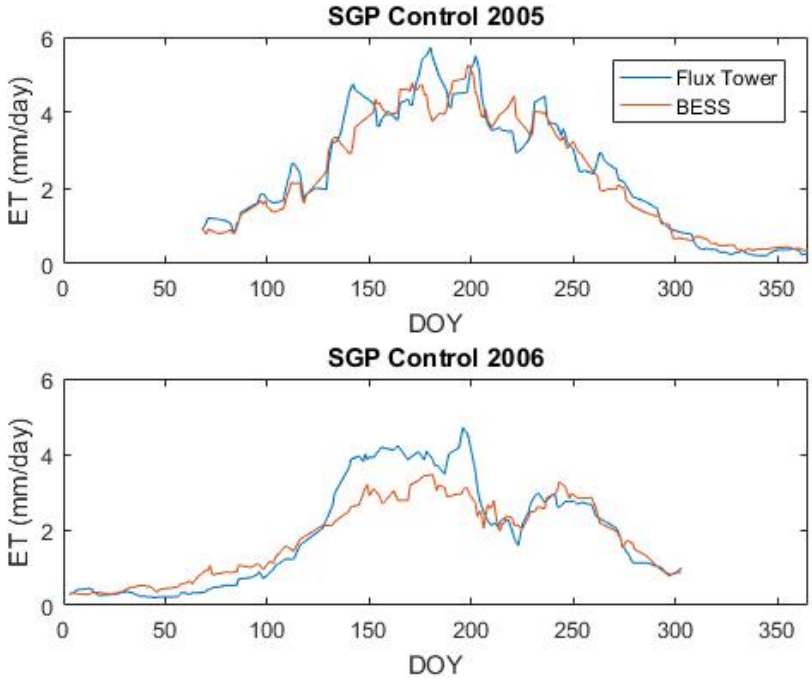
SGP Control 2005
Flux Tower
BESS
ET (mm/day)
DOY
SGP Control 2006
ET (mm/day)
DOY

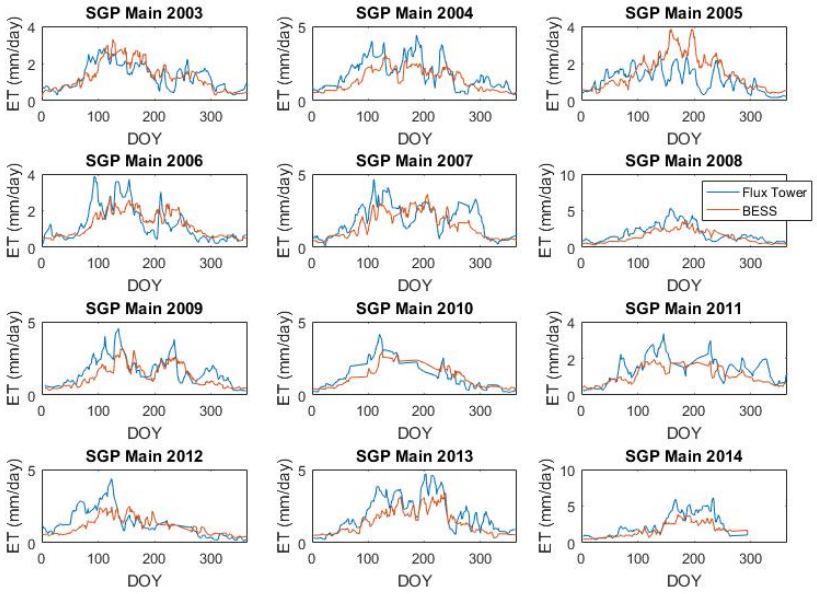
SGP Main 2003
SGP Main 2004
SGP Main 2005
SGP Main 2006
SGP Main 2007
SGP Main 2008
Flux Tower
BESS
SGP Main 2009
SGP Main 2010
SGP Main 2011
SGP Main 2012
SGP Main 2013
SGP Main 2014
ET (mm/day)
DOY

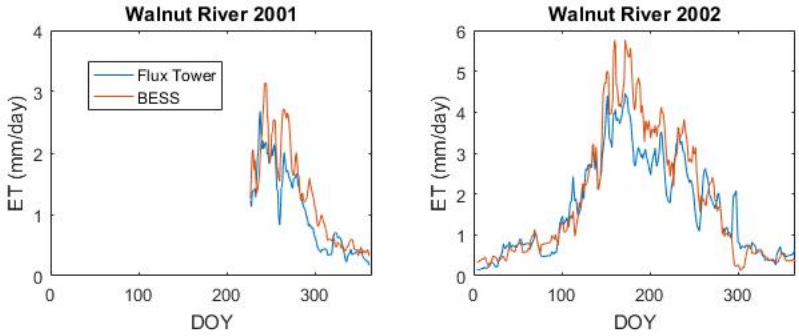
Walnut River 2001
Flux Tower
BESS
ET (mm/day)
DOY

Walnut River 2002
ET (mm/day)
DOY

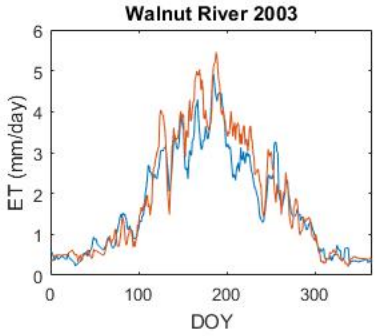
Walnut River 2003
ET (mm/day)
DOY

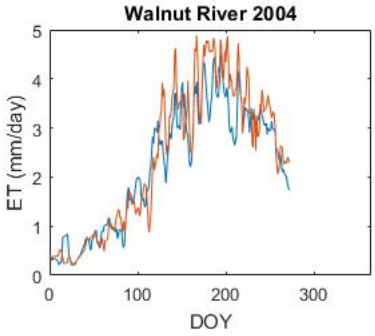
Walnut River 2004
ET (mm/day)
DOY

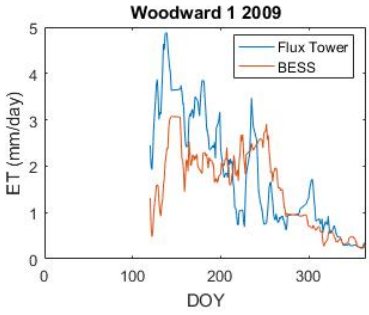
Woodward 1 2009
Flux Tower
BESS
ET (mm/day)
DOY

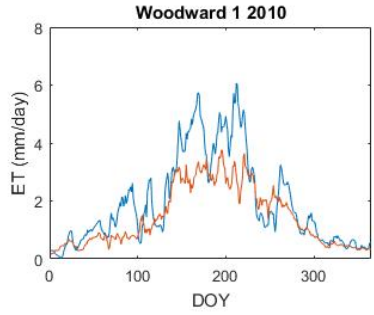
Woodward 1 2010
ET (mm/day)
DOY

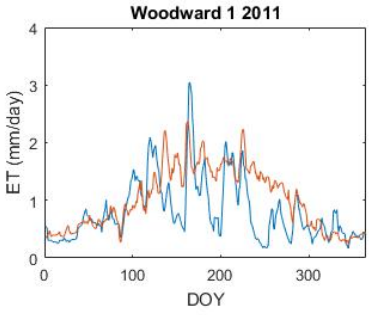
Woodward 1 2011
ET (mm/day)
DOY

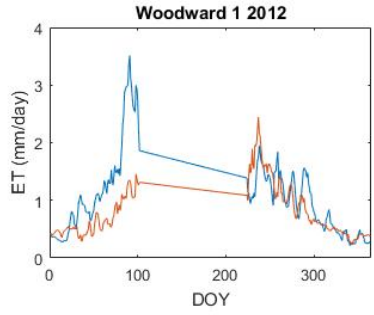
Woodward 1 2012
ET (mm/day)
DOY

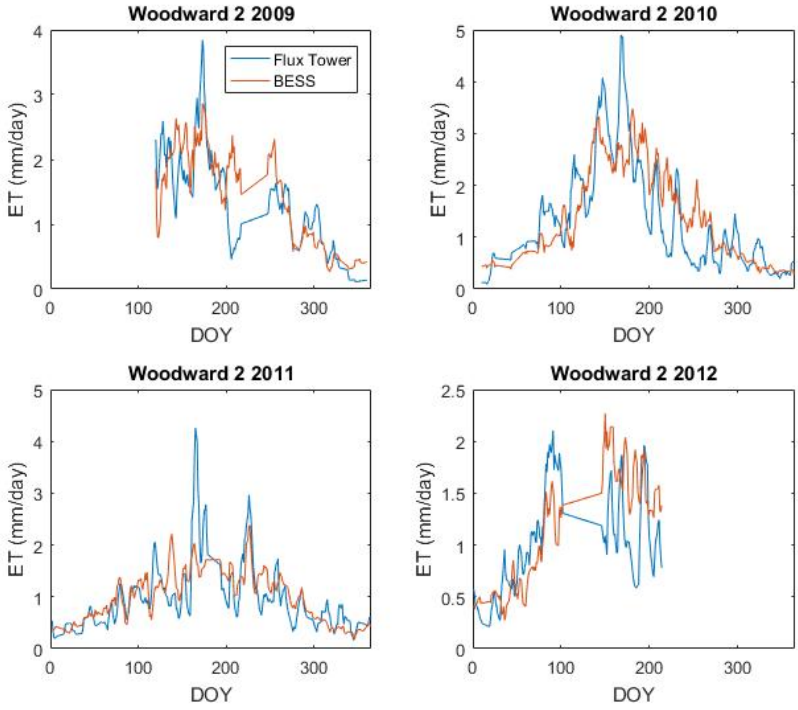
Woodward 2 2009
Flux Tower
BESS
ET (mm/day)
DOY
Woodward 2 2010
ET (mm/day)
DOY
Woodward 2 2011
ET (mm/day)
DOY
Woodward 2 2012
ET (mm/day)
DOY